Degradation Mechanisms of Solid Oxide Fuel Cell Cathodes

Dissertation

zur Erlangung des akademischen Grades
doctor rerum naturalium (Dr. rer. nat.)

vorgelegt dem Rat der
Fakultät für Mathematik und Naturwissenschaften
der Technischen Universität Ilmenau

von Dipl.-Ing.
Martin Finsterbusch
aus Ilmenau

Gutachter:

Prof. Dr. Juergen A. Schaefer, Institut für Physik, Technische Universität Ilmenau

Prof. Dr. Yves U. Idzerda, Physics Department, Montana State University

Prof. Dr. Syed Imad-Uddin Ahmed, Fakultät für Maschinenbau,
Fachhochschule Wolfenbüttel

Tag der Einreichung: 11. Oktober 2011
Tag der öffentlichen Aussprache: 24. November 2011

urn:nbn:de:gbv:ilm1-2011000392

Contents

CHAPTER 4

CHAPTER 5

CHAPTER 6

List of Figures

List of Tables

Chapter 1

1. Introduction and Motivation

The worldwide energy consumption is expected to grow at an annual rate of approx. 1.8% or a total of 49% from 2007 to 2035[2]. For the first time, the energy demand of the non-OECD (Organization for Economic Cooperation and Development) nations exceeded that of the OECD nations in 2007. This trend was enhanced by an uneven recovery from the recession in 2008 and 2009, leading to an actual reduction of total energy use of 2.2% in 2009[2]. Non-OECD nations, foremost in Asia showed a faster recovery from the recession than e.g. Europe or Japan, which reflects on the fact that the expected energy demand growth in those countries is 2.2% compared to 0.5% in OECD nations[2]. Today, fossil fuels (oil, coal and natural gas) provide approx. 83% of the total consumed energy with oil being the highest portion. In the light of this rapid growth in energy demand in non OECD countries and due to the slow increase in oil production we will face high future oil prices. Thus, a shift from oil to coal, natural gas, nuclear- and ultimately renewable energy sources is desired, especially in Europe and North America. Renewable energy sources like hydroelectricity, wind, solar and biomass/waste are a clear focus of energy technology development and implementation, resulting in the largest growth of approx. 2.2% annually[2] of all mentioned energy sources.
However, one drawback of renewable energies is the discrepancy in possible production places and areas of high demand, e.g. surface area available for solar panels in cities. Strong regional preferences for one renewable source or the other can be a second factor, mitigating a broad and fast implementation. A solution can be found in efficient ways of energy storage and transportation which have to be explored to facilitate a rapid growth of renewable energies. In particular, efficient rechargeable batteries, super-capacitors and hydrogen production via water electrolysis are intensely researched and are the most likely candidates for successful energy storage from renewable sources. Since the former two candidates directly yield electrical energy, the production of hydrogen is only viable if cheap and efficient back-conversion to the desired electrical energy can be achieved. Additionally, all three methods take the use and production of carbon (mainly in form of CO_2) out of the energy cycle, which is of great concern with regard to greenhouse effect and global warming.
Fuel cells are electrochemical devices that directly convert chemical energy into electrical energy via “cold” combustion, which is oxidation with very little or no significant heat development. The efficiency (whole system) can be up to 60% which is much higher than internal combustion engines or diesel generators. Since there are no moving parts in a fuel cell they are the perfect solution for silent, low maintenance and long term operation e.g. in residential homes, electric appliances, cars and industry. Another big advantage is enabling the use of liquid bio-fuel, e.g. methanol made from plant matter (used in direct methanol fuel cells) or methane derived from solid waste, wastewater and manure (used in solid oxide fuel cells – SOFCs). Solid oxide fuel cells use ceramic (oxide) components that are cheap to manufacture and can be scaled without losing efficiency, thus enabling modular construction to adapt to different power needs e.g. from a single home up to a multiplex apartment building. Additionally, SOFCs generate some heat that can be used for warm water supply and heating, increasing the (combined) efficiency even further. Advantageous is also the capability to use hydrocarbons from fossil sources, e.g. natural gas, propane, methane, gasified coal etc. in SOFCs due the autocatalytic properties of the

used materials, aiding in a fast commercialization today and during the transition phase from fossil fuels to renewable energy sources.
Unfortunately, long term stability of the used oxide materials with respect to contaminants, structural degradation and material decomposition is still mitigating a broad implementation of SOFCs (and most other fuel cells). Thus, a fundamental understanding of the degradation mechanisms is needed to find the best degradation mitigation strategies and apply them in order to advance the commercialization of fuel cells. In case of fuel contaminants, recent progress in identifying the crucial processes in degradation lead to easing the impact (detrimental effects) of sulfur in the fuel gas on the ceramic materials used on the fuel side of the SOFC. However, material decomposition is still a major issue for all of used ceramics and lacks the desired understanding of underlying mechanisms and basics impact on performance. Especially on the air side, material decomposition can lead to rather high performance degradation, and elimination of this problem would greatly improve the long term stability of SOFCs facilitating the progress of their commercialization.
In this work I want to illuminate the degradation processes found on the air side of SOFCs by identifying the underlying mechanisms and propose possible mitigation strategies. Hereby, I utilized mostly X-ray spectroscopy techniques to gain insight into the structural configuration of the used oxide ceramics. The differences of cells as manufactured and after running them for given periods of time under various simulated conditions expected in commercial SOFCs are extracted. X-ray absorption spectroscopy (XAS) has been shown to be a perfect tool for this task due to its element specificity, sensitivity to chemical states and tolerance of the often porous nature of the oxide material. After an introduction to synchrotron radiation and SOFCs, my research of the impact of Cr contamination on the oxygen uptake at the air side of SOFCs is outlined. Afterwards the investigation of the structural decomposition of $La_{0.6}Sr_{0.4}Co_{0.2}Fe_{0.8}O_{3-\delta}$ (LSCF), a commonly used cathode material in SOFCs, is presented. Finally the ongoing research of the degradation of thin LSCF cathodes via X-ray absorption mapping, a newly developed method at the Advanced Light Source (Lawrence Berkeley National Lab, Berkeley, CA) is explained in detail. All these topics show the various ways of degradation but also the numerous ways to approach this problem using a multitude of surface science techniques and combining them to identify the underlying mechanism and draw a more complete picture of degradation for these interconnected and related degradation problems.

Chapter 2

2. Theoretical Background

2.1. Synchrotron Radiation

The following part presents an overview of the history of synchrotron radiation generation and the main differences of the beamlines (undulator vs. bend magnet) are explained in detail. The research was conducted at the National Synchrotron Light Source (NSLS) at Brookhaven National Labs, Brookhaven, NY and the Advanced Light Source (ALS) at Lawrence Berkeley National Labs, Berkeley, CA. In particular, measurements were done at beamline U4B at NSLS and beamlines 6.3.1 and 4.0.2 at ALS.

2.1.1. Bend magnets and Undulators

Since the discovery of the electron, radiative energy loss encountered in the classical treatment of its circular motion posed a problem for early models of the structure of atoms. Until Bohr's Postulates of the loss free electron shells, the theory behind these dipol-losses evolved rapidly. In the 1930's and 40's scientists experimented with magnetic induction electron accelerators, so-called Synchrotrons or Betatrons, and were able to predict the energy loss of a given system due to the radiative losses of the electrons. The first Betatron was built in 1940 by Kerst at the University of Illinois and operated with electron energies of 2.3 MeV[3]. Betatrons were (and are) used as high intensity X-ray sources for nuclear research and medical applications. Four years later, General Electric (GE) commissioned a 100 MeV Betatron and Blewett began the search for the predicted synchrotron losses. Unfortunately, the produced wavelength peaked in the infrared/visible range but the tube in which the electrons circulated was opaque. Proof came from another project at GE one year later where the problem of mass increase at relativistic velocities was investigated. Since heavier particles experience less acceleration they get out of sync with the RF excitation, effectively slowing down. Since the opposite is true for lighter particles, a self – stabilizing effect of the electron bunch is observed, allowing for stable operation. To reach higher energies, the RF frequency had to be reduced in accordance with the mass gain of the electrons. This was tested at a newly built 70 MeV electron synchrotron which had a transparent electron tube and was not fully shielded[3]. This allowed for the first observation of synchrotron radiation as seen in Figure 1 and measurement of its characteristic energy and polarization characteristics.

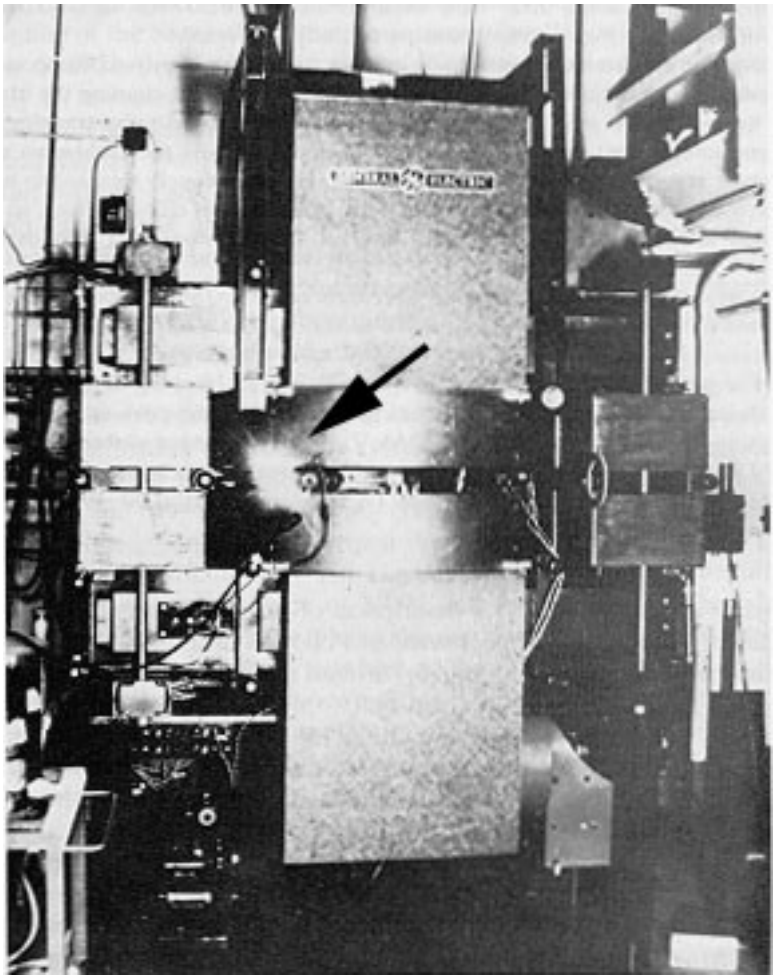

Figure 1: Picture of the 70 MeV electron synchrotron at GE, where synchrotron radiation was observed for the first time. (from Ref [3])

At first, synchrotron radiation was only used from a parasitic point of view, at facilities dedicated to high-energy or nuclear physics. The first of these so-called first generation synchrotrons was the National Bureau of Standards 180 MeV synchrotron that in 1961, after it "had outlived its usefulness for nuclear physics"[3], was modified to allow access to the vacuum system for extraction of synchrotron radiation. At first, studies in the UV region lead to new observations in the absorption spectra of noble gases and sparked the interest in this new measurement technique. The trend to higher and higher electron energies, resulting in lower and lower wavelengths culminated in 1964 when operation of the 6 GeV Deutsches Elektronen Synchrotron (DESY) in Hamburg, Germany started. Reaching the soft X-ray region with wavelengths of 0.1Å, photoemission measurements in aluminum and absorption measurements of metals and alkali-halides were possible[3]. In contrast to synchrotrons, electron storage rings were also in use, mainly as electron – positron colliders. Here, the electrons were run continuously for hours at a fixed energy, rather than injecting, accelerating and extracting the electrons at frequencies of up to 50 Hz at an electron synchrotron. This allowed for much longer and stable radiation extraction but due to the primary use as collider, beam intensities and electron energies were rather low. The increased popularity of storage rings and more and more interest in studies using synchrotron radiation finally lead to the second generation of synchrotrons, only dedicated to optimize and maximize synchrotron radiation generation and extraction.

In 1981, the Synchrotron Radiation Source at the Daresbury Laboratory, UK with 2 GeV and the National Synchrotron Light Source in Brookhaven, NY consisting of a 700 MeV (for UV) and a 2.5 GeV (for soft X-rays) storage ring finished construction. The Stanford Synchrotron Radiation Laboratory was added to the Stanford Linear Accelerator Center (SLAC) and the Hamburger Synchrotronstrahlungslabor (HASYLAB) was added to DESY in order to gradually make the change from high energy physics focus to synchrotron radiation. With these dedicated facilities, new X-ray techniques were developed using the specific characteristics of synchrotron radiation, e.g. extended X-ray absorption fine structure (EXASF), angle resolved photoelectron spectroscopy (ARPES) and high resolution protein crystallography.

In order to rate the quality of all these different types of synchrotrons with different electron energies scientists usually refer to the spectral brightness or brilliance, which in optical systems is invariant for a given system and cannot be improved by optical techniques. The brightness is the radiated energy per unit area (flux) per unit solid angle per unit spectral bandwidth [3] in units of $W \quad m^2 \times sr \times s^{-1}$. This makes careful planning of the radiation source most important since a broad electron beam resulting in a large radiation cone can be fixed by focusing the beam but results in a larger beam divergence. The careful arrangement of the dipole, quadrupole and sextupole magnets used in the electron storage ring is called lattice and goes back to the planning of NSLS by Chasman and Green, whose design is the basis for most of today's storage rings[3].

Today, instability in the beam is often mainly due to "hopping" from one lattice trajectory to another which ultimately results in an energy shift of peaks observed in the acquired spectra. The reason is that this shift in lattice trajectory corresponds to a change in incident angle on the monochrometer which voids the energy calibration. Energy referencing is thus necessary in order to obtain absolute values for absorption edges and can be achieved by simultaneously measuring the absorption edge of a known compound with the edge of the sample of interest. This method is used e.g. at beamline U4B at NSLS. Positioning the standard sample in front of the entrance aperture of the chamber avoids loosing beam intensity incident on the actual sample.

During this strive for increasing brightness, a concept was explored based on theoretical work by Ginzburg (Soviet Union) in 1944 using an array of altering magnetic fields to "wiggle" or "undulate" the electron beam horizontally in a sinusoidal pattern, as shown in Figure 2. This motion, as proved experimentally in 1953 by Motz and coworkers at Stanford University[3], also produces electromagnetic waves which are polarized (horizontally) and can be used for spectroscopy. Most of the so-called "wigglers" and "undulators" used today are planar, vertical arrays of permanent magnets with a characteristic repetition length (period) of λ_U, the undulator period. The main difference between undulators and wigglers is the strength of the magnetic field which is much higher for wigglers, resulting in large oscillation amplitudes of the electrons. These wide excursions have the advantage of a high photon flux due to larger acceleration and a rather broad spectrum but at the cost of spatial collimation (broad radiation cone) and thus low spectral brightness. Undulators on the other hand have much weaker magnetic fields with much lower excursions of the electrons which then fall within the radiation cone θ_{con} resulting in constructive and destructive interference of the emitted radiation. This leads to the main difference of undulator radiation with respect to bend magnets and wigglers – only the fundamental wavelength and some of its harmonics are produced and usually have very narrow spectral bandwidth and low spatial divergence, resulting in very high spectral brightness. Since higher energies (lower wavelengths) are usually harder to generate, these harmonics can be used to extend the energy range of a given undulator[4]. However, changes in both polarization and radiation cones have to be considered.

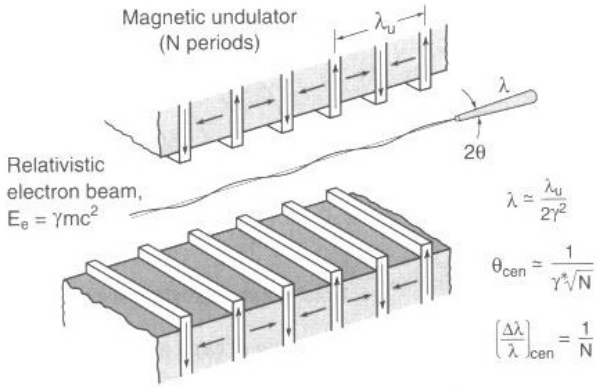

Figure 2: Working principle of an undulator. An array of magnetic dipols (length of one period λ_U) induces a sinusoidal motion of the electron beam, producing a characteristic wavelength λ of light with low divergence and thus high spectral brightness. (from Ref [4])

To change the energy of an undulator, the magnets have to be moved vertically (adjusting the gap between the two magnetic dipole arrays) increasing and decreasing the strength of the magnetic field and thereby the excursion of the electrons. This change in the gap is desirable since it does not involve changes in the electron beam lattice. However, there is still an adverse effect on the electron bunch requiring the use of corrective elements before and after each undulator to actively counteract the changes resulting from changing the gap. Even the generation of elliptically polarized light, naturally produced by bend magnets at the edges of the radiation cone, can be produced by specially designed undulators which further restrict the produced harmonics. Since both wigglers and undulators operate with straight electron beams, a new generation of synchrotrons, the third generation, was constructed to fully exploit the advantages of these so-called "insertion" devices (Figure 3). The new design went from circular rings to straight sections for insertion devices, connected by bend magnets to achieve the basic ring structure for the electron beam lattice. End-user stations can now either be a bend magnet or an undulator with their characteristic radiation properties according to the specific spectroscopic needs. For example, I encountered a problem of peak overlap due to harmonic light in the spectrum, which was eliminated by using elliptically polarized light at the undulator beamline 4.0.2. The faster scan capability of the bend magnet beamline 6.3.1 enabled the use of XAS mapping of the surface of a sample (see next Chapter). Both examples nicely show the possibility of complimentary use of both radiation generation techniques. The first third generation synchrotron facility was the European Synchrotron Radiation Facility (ESRF) in Grenoble, France in 1994, followed by the Advanced Photon Source at Argonne National Labs (near Chicago, Illinois) in 1996[3]. Besides, both wigglers and undulators have been "retrofitted" successfully into old storage rings and some second generation synchrotrons were built with the possibility of adding insertion devices, like NSLS[3]. Extensive use and research with undulators resulted in the successful development of a free electron laser (FEL) using the long spatial coherence of the emitted synchrotron radiation. When using the electron beam in the synchrotron as lasing medium, very fast pulses in the fs range with tunable energy and ultra-high spectral brightness are possible and opened the way to possible 4th generation facilities[3]. Efforts

are currently made at HASYLAB (DESY) and SLAC to implement such a FEL into an existing synchrotron facility or linear accelerator respectively.

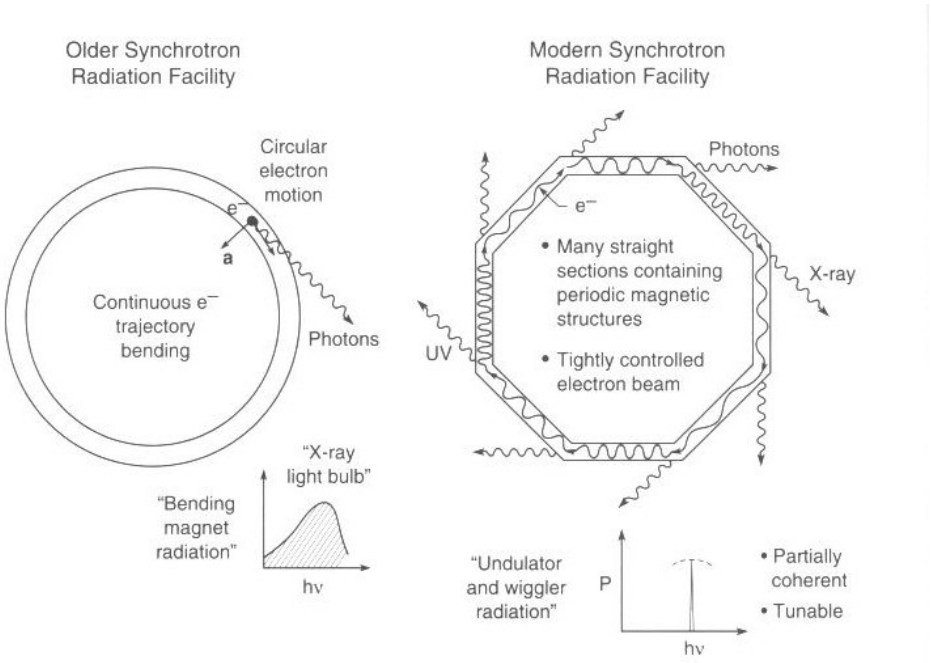

Figure 3: (left side) "Early synchrotron radiation facilities basically consisted of circular rings for bending magnet radiation, although some have been retrofitted with periodic magnetic structures (undulators or wigglers). They generally have an electron beam of relatively large cross section and angular divergence (right side). Modern storage rings are dedicated to broad scientific use and optimized for high spectral brightness through the inclusion of many long straight sections for undulators and wigglers, as well as very tightly confined (spatial and angular extent) electron beams. Bending magnet radiation is also generated in tuning from one straight section to the next (not shown)." (from Ref [4])

2.2. X-ray Absorption Spectroscopy (XAS)

X-ray absorption spectroscopy (XAS) is the technique, involving synchrotron radiation, mostly used for conducting the research presented in this thesis. The selection rules governing the electron transition are derived in this chapter and the basics of a new measurement method, the fast scan capability of beamline 6.3.1 are explained.

2.2.1. XAS and Fermi's Golden Rule

The discovery of X-rays by Wilhelm C. Röntgen in 1895[5] and their usefulness for imaging biological systems sparked the development of several new techniques for material analysis as well. After Max von Laue discovered the scattering of X-rays in 1913, microscopy and spectroscopy of materials via X-rays became a main pillar of condensed matter analysis. When X-rays pass through a material, three interactions are possible: scattering, absorption and fluorescence. For most techniques the generation of X-rays determines the analysis method since it fixes the characteristics of the generated radiation. Conventional X-ray generation via X-ray tubes (possibly using a monochromator) is used e.g. for stand-alone X-ray powder diffraction (XRD), X-ray photoelectron spectroscopy (XPS) and X-ray fluorescent spectroscopy (XRF). The energy of the X-rays is hereby limited to a specific energy, determined by the material used in the X-ray tube (e.g. Al or Mg) and a monochromator is often needed to decrease the peak width of the main emission peak and suppress the Bremsstrahlung background. The excited electrons are then analyzed by their kinetic energy remaining after the excitation to vacuum level. As explained in the previous chapter, X-rays generated by synchrotrons have the advantage of tunable energy due to the same brightness over a large energy range and good energy selectivity by gratings. This enables techniques that use resonant transitions, that is, from one state in the atom/solid to another, rather than exciting electrons all the way to the vacuum level. The main resonant techniques are X-ray absorption spectroscopy (XAS) and X-ray resonant scattering (XRS) and the quantum mechanics (selection rules) governing both will be explained here in detail, since XAS was the main technique used to obtain the results presented in this thesis. Transition metals are a very useful example since they are materials of interest in the studies presented here and the relevant simplifications and conventions allow a better understanding of the research presented later. Following the very detailed explanation of Stöhr and Siegmann[6] X-ray absorption is most easily viewed in the one electron picture, neglecting the effect on all the other electrons caused by the interaction of X-rays with the photo-electron. However, this can lead to confusion since the state measured is the excited state, not the ground state. Therefore, when depicting the transition, spin-orbit and other interactions, lifting the degeneracy of certain states have to be considered. A good example of this dilemma is the visualization of the absorption of an X-ray photon leading to a transition from 2p to 3d in a transition metal in Figure 4a (for example spectrum, see e.g. Figure 8 - Ni L_{23} in NiO). The one electron picture shows the spin-orbit split 2p states with the $2p_{3/2}$ and $2p_{1/2}$ levels, originating from $j=l\pm s$, as initial states and also the spin-orbit split d states $3d_{3/2}$ and $3d_{5/2}$ as final states. However, as Stöhr and Siegmann[6] point out, this is can be misleading since the 2p core shell in the ground state is completely filled and thus no spin orbit splitting is observed since the net angular momentum is zero.

Using the complementary hole rather than the electron transition is a more correct way to depict the transition, as shown in Figure 4b.

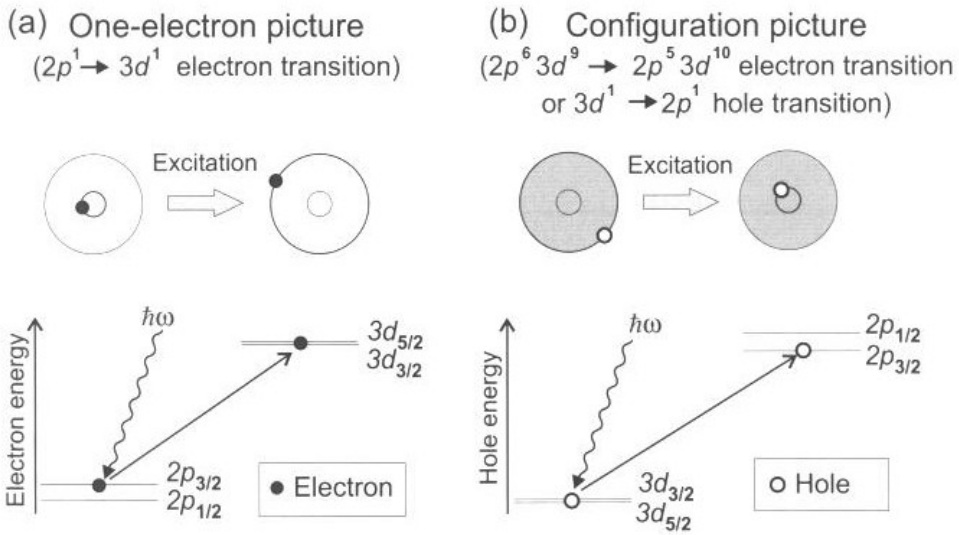

Figure 4: Resonant L edge absorption in two pictures a) one electron picture and b) hole picture for d^9 configuration. Both p and d states are spin-orbit split in the final state but the splitting of the p states is much larger (~15eV) than the splitting of the d states (~50meV) since the p shell is much more compact, dominating the XAS spectrum. (from Ref[6])

The simplest transition case is a $2p^6\ 3d^9$ configuration with only 1 hole in the d shell (e.g. Cu^{2+}). The absorption from above, promoting an electron from $2p_{3/2}$ to 3d, can now be described as a hole being promoted from the initial 3d level now correctly split by the spin orbit interaction into $3d_{3/2}$ and $3d_{5/2}$ into the final $2p_{3/2}$ also correctly split by the spin orbit interaction (note that the energy is inverted, since the hole has the opposite spin of the electron). This shows the importance of the fact that absorption spectroscopy always measures the excited, rather than the ground state of the atom. However, both pictures are not equivalent when there is more than 1 hole or electron in the d shell present and interactions between them have to be considered, e.g. multiplet structures.

When trying to determine which final states can be reached by exciting the atom in the ground (initial) state with a photon, we usually use the "dipole selection rules". Knowledge of the initial and final state, the amount of energy needed to excite an electron from one state to the other state and how the polarization of the light affects the absorption or scattering is crucial since energy and polarization of the synchrotron radiation used in our experiments needs to be selected. Thus in-depth knowledge of the rules governing absorption and scattering is very important and will be explained in the following pages. The formalism of how the system evolves from the initial state i to the final state f was first derived by Kramers, Heisenberg and Dirac and a very good derivation (that we will follow to obtain "Fermi's Golden Rule") can be found in Ref [7]. The incoming electromagnetic wave (photon) interacts with the electron via the electric field and can be described using the vector-potential:

$$\boldsymbol{E} = \frac{\partial \boldsymbol{A}\ \boldsymbol{r},t}{\partial t}$$

$$\boldsymbol{A}\ \boldsymbol{r},t\ = \boldsymbol{A_0} e^{i\ \boldsymbol{k}\cdot\boldsymbol{r}-\omega t}$$

Since both fields are time dependent, we have to treat the interaction via time-dependent perturbation theory. Starting with the Schrödinger equation:

$$i\hbar \frac{\partial \Psi(\boldsymbol{r},t)}{\partial t} = H\Psi(\boldsymbol{r},t)$$

we can separate the Hamiltonian into a time independent term H^0 and the time dependent perturbation $\mathrm{H}'(t)$:

$$H\ \mathrm{t}\ = \mathrm{H}^0 + \mathrm{H}'(t)$$

We have to solve it to first order for $\mathrm{H}'(t)$ and since the time independent H^0 gives us only a phase factor of exp $-iE_i^0 t/\hbar$ we can eliminate H^0 by including this phase term. The amplitude of the transition d_f can then be written as (for more details see Ref. [7], Chapter 18):

$$d_f\ \mathrm{t}\ = \delta_{fi} - \frac{i}{\hbar} \int_0^t f^0\ \mathrm{H}'(t')\ i^0\ \ e^{i\omega_{fi}t'}\, dt'$$

Since we want to investigate the interaction of a photon with an electron, the perturbation part of the Hamiltonian has to contain an electron part and a photon part and is found to be the dot product of the vector potential $\boldsymbol{A}\ \boldsymbol{r},t$ of the incoming photon (em-wave) and the momentum operator $\boldsymbol{P}$ of the electron [6, 7] :

$$\mathrm{H}'\ t\ = \frac{e}{2mc}\ \ \boldsymbol{A}\cdot\boldsymbol{P} + \boldsymbol{P}\cdot\boldsymbol{A}$$

$$= \frac{e}{2mc}\ \boldsymbol{A}\cdot\boldsymbol{P} \qquad because\ \boldsymbol{\nabla}\cdot\boldsymbol{A} = 0$$

$$= \frac{e}{2mc}\ e^{i\ \boldsymbol{k}\cdot\boldsymbol{r}-\omega t}\ \boldsymbol{A_0}\cdot\boldsymbol{P}$$

$$\mathrm{H}'\ t\ = \mathrm{H}' e^{-i\omega t}$$

with

$$\mathrm{H}' = \frac{e}{2mc}\ e^{i\boldsymbol{k}\cdot\boldsymbol{r}}\boldsymbol{A_0}\cdot\boldsymbol{P}$$

The transition Amplitude now becomes (considering $i \neq f$):

$$d_f\ \mathrm{t}\ = -\frac{i}{\hbar}\int_0^t f^0\ \mathrm{H}' e^{-i\omega t}\ i^0\ \ e^{i\omega_{fi}t'}\,dt'$$

$$d_f\ \mathrm{t}\ = -\frac{i}{\hbar}\int_0^t f^0\ \mathrm{H}'\ i^0\ \ e^{i\ \omega_{fi}-\omega\ t'}\,dt'$$

$$d_f\ \mathrm{t}\ = -\frac{i}{\hbar}\ f^0\ \mathrm{H}'\ i^0\ \ \frac{e^{i\ \omega_{fi}-\omega\ t}-1}{i\ \ \omega_{fi}-\omega}$$

With the probability of the transition $i \rightarrow f$

$$P_{i\rightarrow f} = \ d_f\ ^2 = \frac{1}{\hbar^2}\ \ f^0\ \mathrm{H}'\ i^0\ \ ^2\ \ \frac{sin\ \ \ \omega_{fi}-\omega\ \frac{t}{2}}{\omega_{fi}-\omega\ \ \frac{t}{2}}\ \ ^2\ t^2$$

The latter term $sin^2x\ \ x^2$ peaks at x=0 and has the width π so that the system wants to go to final states f where

$$\omega_{fi}-\omega\ \ \frac{t}{2}\ \leq \pi$$

or

$$E_f^0 - E_i^0 = \hbar\omega\ \ 1 \pm \frac{2\pi}{\omega t}$$

This demonstrates that the electron only prefers the higher energy final state after being exposed to the perturbation of the photon for a couple of periods, e.g. $\omega t \gg 2\pi$. To obtain the final state we have to wait some time with the perturbation acting on our system. If we consider the case of a system exposed to the perturbation all the time[7]:

$$d_f\ \mathrm{t}\ = \lim_{T\rightarrow\infty} -\frac{i}{\hbar}\int_{-T/2}^{T/2} f^0\ \mathrm{H}'\ i^0\ \ e^{i\ \omega_{fi}-\omega\ t'}\,dt'$$

$$= -\frac{2\pi i}{\hbar}\ f^0\ \mathrm{H}'\ i^0\ \delta\ \ \omega_{fi}-\omega$$

we find the transition probability:

$$P_{i\rightarrow f} = \frac{4\pi^2}{\hbar^2}\ \ f^0\ \mathrm{H}'\ i^0\ \ ^2\delta\ \ \omega_{fi}-\omega\ \ \delta\ \ \omega_{fi}-\omega$$

With

$$\delta\ \omega_{fi} - \omega\ \delta\ \omega_{fi} - \omega\ = \delta\ \omega_{fi} - \omega\ \lim_{T\to\infty} \frac{T}{2\pi}$$

We get the average transition rate[7]:

$$R_{i\to f} = \frac{P_{i\to f}}{T} = \frac{2\pi}{\hbar}\ \ f^0\ \mathrm{H}'\ i^0\ \ ^2\delta\ E_f^0 - E_i^0 - \hbar\omega$$

which was originally derived by Dirac and called by Fermi "Golden Rule No. 2"[6] and is now commonly referred to as *Fermi's Golden Rule*. If we want to include scattering (elastic (resonant) and inelastic), we have to solve the matrix element up to second order for $\mathrm{H}'(t)$ and the transition rate $T_{i\to f}$ (which is normalized to the density of the final states $\rho\ \mathcal{E}_f$ and in units of 1/time) becomes[6]:

$$T_{i\to f} = \frac{2\pi}{\hbar}\ \ f\ \mathrm{H}'\ i\ + \sum_n \frac{f\ \mathrm{H}'\ n\ \ n\ \mathrm{H}'\ i}{\mathcal{E}_i - \mathcal{E}_n}\ \ ^2\delta\ \mathcal{E}_i - \mathcal{E}_f\ \rho\ \mathcal{E}_f$$

with the system going through intermediate (virtual) states n and the sum being over all possible intermediate energy states $\mathcal{E}_n$. In this equation the initial i and final states f are the product of both atomic and photonic states and the energies $\mathcal{E}_i$ and $\mathcal{E}_f$ are the combined energies of electron and photon, making it consistent with the earlier equation (also regarding energy conservation) for absorption by:

$$\delta\ \mathcal{E}_i - \mathcal{E}_n\ = \delta\ E_i^0 + \hbar\omega - E_f^0$$

for resonant (elastic) scattering by:

$$\delta\ \mathcal{E}_i - \mathcal{E}_n\ = \delta\ \ E_i^0 + \hbar\omega - \ E_f^0 + \hbar\omega\ \ = \delta\ E_i^0 - E_f^0$$

for inelastic scattering by:

$$\delta\ \mathcal{E}_i - \mathcal{E}_n\ = \delta\ \ E_i^0 + \hbar\omega_1 - \ E_f^0 + \hbar\omega_2\ \ = \delta\ \ E_i^0 - E_f^0 + \hbar\ \omega_1 - \omega_2$$

The second order term is now commonly called *Kramers-Heisenberg Relation* and was referred to by Fermi as "Golden Rule No. 1". The intermediate or virtual states the system goes through do not need to obey energy conservation since the intermediate states do not show up in the δ function. The possibility of inelastic scattering – where the photon gains or loses energy, is used to explain e.g. Raman scattering. To obtain the total cross section of the photon – electron interaction σ_{tot} we have to divide the transition rate by the total incoming flux of photons Φ_0:

$$\sigma_{tot} = \frac{T_{i\to f}}{\Phi_0}$$

The unit of σ_{tot}:

$$\sigma_{tot} = \frac{T_{i\to f}}{\Phi_0} = \frac{1}{\frac{1}{time}} = time \cdot area$$

is usually given in (Mega) barn whereas 1 Mb = 10^{-22} m^2.

2.2.2. The Dipole Selection and Sum Rules

If we want to find the transitions of an electron, which are allowed when an incident photon excites it; we know form Fermi's golden rule that the term $\langle f | H' | i \rangle$ has to be non-zero. In order to arrive at the "dipole selection rules" we have to further evaluate this term to find the conditions under which it is non-zero. The time-independent Hamiltonian is still a function of the photon wave vector **k**:

$$H' = \frac{e}{2mc} e^{i\boldsymbol{k}\cdot\boldsymbol{r}} \boldsymbol{A_0} \cdot \boldsymbol{P}$$

It is usually sufficient to eliminate the k dependence by expanding the exponential only to first order and write the electron momentum operator **P** in terms of the length operator **r**:

$$e^{i\boldsymbol{k}\cdot\boldsymbol{r}} \boldsymbol{A_0} \cdot \boldsymbol{P} = \left(1 + ikr + \cdots\right) \boldsymbol{A_0} \cdot \boldsymbol{P} \cong \boldsymbol{A_0} \cdot \boldsymbol{P} = im_e \omega_{if} \boldsymbol{A_o} \cdot \boldsymbol{r}$$

This approximation is called "dipole approximation", where m_e is the electron rest mass and ω_{if} is the photon frequency associated with the transition $i \to f$. The vector potential amplitude can now be interpreted as the polarization vector of the photon **ϵ**. This approximation is only valid if the size of the absorbing shell is much smaller than the wavelength of the incident photon

$$\boldsymbol{r} \ll \frac{\lambda}{2\pi}$$

which is the case for photon energies of soft X-rays (<2000eV, $\lambda > 0.6\,nm$) in combination with the here commonly measured $p \to d$ transitions (L-edge) where the 2p core shell radius is approx. 0.01nm (factor of 60 smaller). We can now write the absorption cross section for a transition from a discrete initial state a to a discrete final state b as[6]:

$$\sigma^{abs} = 4\pi^2 \frac{e^2}{4\pi\epsilon_0 \hbar c} \hbar\omega \; |\langle a | \boldsymbol{\epsilon} \cdot \mathbf{r} | b \rangle|^2 \delta\left(E_b - E_a - \hbar\omega_{ab}\right) \rho\left(E_b\right)$$

and we get the X-ray absorption resonance intensity I_{res} from calculating the energy integral over the cross section and if the initial and final states are volume normalized to unity we get[6] :

$$I_{res} = A \; |\langle a | \boldsymbol{\epsilon} \cdot \mathbf{r} | b \rangle|^2$$

With the proportionality factor A:

$$A = 4\pi^2 \alpha_f \hbar\omega$$

Containing the fine structure constant α_f:

$$\alpha_f = \frac{e^2}{4\pi\epsilon_0 \hbar c} = \frac{1}{137.04}$$

The unit of I_{res} is [length^2 x energy], commonly given in [Mb x eV]. In order to obtain the dipole selection rules we have to evaluate the effect of the $\boldsymbol{\epsilon} \cdot \mathbf{r}$ on the initial and final state of the electron. As described earlier, for XAS at a modern (undulator) beamline it is possible to use 100% circular polarized light in addition to fully linear-polarized light. Thus, we want to derive the selection rules for linear and circular polarized light. The polarization vector for both cases can be written in terms of the angular momentum $l_p = q\hbar$ carried by the photon, where q is 0 for linear light and ±1 for circular polarized light and its polarization direction $\boldsymbol{\alpha}$ (in cartesian coordinates $\boldsymbol{r} = x\boldsymbol{e_x} + y\boldsymbol{e_x} + z\boldsymbol{e_x}$):

$$\boldsymbol{\epsilon_\alpha^q}$$

For linear light, this yields for the extreme cases with polarization along the coordinate axes[6]:

$$\boldsymbol{\epsilon_x^0} = \boldsymbol{\epsilon_x} = \mathbf{e}_x$$
$$\boldsymbol{\epsilon_y^0} = \boldsymbol{\epsilon_y} = \mathbf{e}_y$$
$$\boldsymbol{\epsilon_z^0} = \boldsymbol{\epsilon_z} = \mathbf{e}_z$$

Whereas for circular polarized light the angular momentum is parallel to the propagation vector **k** and if we determine it to be in the z – direction we can write for the polarization[6]:

$$\boldsymbol{\epsilon_z^\pm} = \mp\frac{1}{\sqrt{2}}\ \boldsymbol{\epsilon_x} \pm i\boldsymbol{\epsilon_y}$$

the other propagation directions can be directly obtained from permutation of the coordinate indices x, y and z. We can now define the polarization-dependent dipole operator P_α^q:

$$P_\alpha^q = \boldsymbol{\epsilon_\alpha^q} \cdot \boldsymbol{r}$$

which in turn can be expressed in terms of the spherical harmonics $Y_{l,m}\ \theta, \phi$ also used to describe electron orbitals, thus connecting the dipole operator to the electrons initial and final state. For $\alpha = z$ we obtain[6] for circular light:

$$P_z^\pm = \boldsymbol{\epsilon_z^\pm} \cdot \boldsymbol{r} = \mp\frac{1}{\sqrt{2}}\ \mathrm{x} \pm i\mathrm{y}\ = r\ \sqrt{\frac{4\pi}{3}} Y_{1,\pm1}$$

and for linear light:

$$P_z^0 = \boldsymbol{\epsilon_z^0} \cdot \boldsymbol{r} = \mathrm{z} = r \sqrt{\frac{4\pi}{3}} Y_{1,0}$$

which we can simplify using Racah's spherical tensors, defined as[6]:

$$C_m^{(l)} = \sqrt{\frac{4\pi}{2l+1}} Y_{l,m}\ \theta, \phi$$

and rewrite the dipole operator to (for details see appendix A3 and A4 of ref [6]):

$$P_z^0 = rC_0^{(1)} = rcos\theta = z$$

$$P_z^{\pm} = rC_{\pm 1}^{(1)} = \mp r\frac{1}{\sqrt{2}}\ sin\theta\ e^{\pm i\phi} = \mp\frac{1}{\sqrt{2}}\ x \pm iy$$

We are now able to rewrite the X-ray absorption intensity I_{res} in terms of the dipole operator:

$$\mathrm{I}_{res} = \mathrm{A}\ \ a\ \boldsymbol{\epsilon} \cdot \mathbf{r}\ b\ \ ^2 = \mathrm{A}\ \ a\ P_\alpha^q\ b\ \ ^2$$

allowing us to finally evaluate the (polarization dependent) dipole matrix element $a\ P_\alpha^q\ b$ where $\alpha = x, y\ and\ z$ for the polarization direction of the photon (**k** direction for circular polarized light) and q=0, ±1 for linear and circular light, respectively. The dipole matrix element depends on a and b, the initial and final state, which in the one electron picture is the core and valence electron wave function, respectively, and can be written as[6]:

$$R_{n,l}\ r\ Y_{l,m_l}\ \theta, \phi\ \chi_{s,m_s} = R_{n,l}\ r\ ; l, m_l, s, m_s$$

Where $R_{n,l}\ r$ is the radial component of the wave function of the shell n with angular momentum l, $Y_{l,m_l}\ \theta, \phi$ is the spherical harmonic describing the angular part and χ_{s,m_s} the spin part. If, in the one electron picture, we pick the initial state wave function a with the core shell number n and angular momentum c:

$$a = R_{n,c}\ r\ ; c, m_c, s, m_s$$

and the final state wave function b with the valence shell number n' and angular momentum l:

$$b = R_{n',l}\ r\ ; l, m_l, s, m'_s$$

we can calculate the dipole (transition) matrix element:

$$a\ P_\alpha^q\ b\ =\ R_{n',l}\ r\ ;l,m_l,s,m'_s\ P_\alpha^q\ R_{n,c}\ r\ ;c,m_c,s,m_s$$

It can be shown that for our simplified case $\alpha = z$ this transition has the general form of [6]:

$$a\ P_z^{0,\pm1}\ b\ = \underbrace{\delta\ m'_s,m_s}_{spin}\ \underbrace{R_{n',l}\ r\ \ r\ R_{n,c}\ r}_{radial}\ \underbrace{l,m_l\ C_{0,\pm1}^{(1)}\ c,m_c}_{angular}\ _{m_l,m_c}$$

where spin, radial and angular parts are separated. Conclusions can already be drawn from the general form. In order for the dipole matrix element to be non-zero, the spin state of the electron *cannot* change since otherwise the delta function would make it zero (this will later be one of the selection rules). The radial part of the dipole matrix element, given by:

$$R_{n',l}\ r\ \ r\ R_{n,c}\ r\ \ =\ \int_0^\infty R_{n',l}^*\ r\ \ R_{n,c}\ r\ r^3 dr$$

has its main contribution in the near core region for the transition $2p \rightarrow 3d$, as seen in Figure 5. This sets X-ray absorption spectroscopy apart from optical spectroscopy. In contrast to optical transitions with energies of ~1 eV, that only allow interband transitions in the valence band which are often delocalized and thus not element-specific, the much higher energies of X-rays enable core electron excitations which are localized at a specific atom, thus giving XAS its element specificity and sensitivity to the local environment (valence shell properties). The main part of the dipole selection rules, however, lies in the angular part of the dipole matrix element. They were tabulated by Condon and Shortley and by Slater and the non-zero ones are:

$$l+1,m\ C_0^{(1)}\ l,m\ =\ \frac{l+1\ ^2-m^2}{2l+3\ \ 2l+1}$$

$$l-1,m\ C_0^{(1)}\ l,m\ =\ \frac{l^2-m^2}{2l-1\ \ 2l+1}$$

for linear light and:

$$l+1,m+1\ C_{+1}^{(1)}\ l,m\ =\ \frac{l+m+2\ \ l+m+1}{2\ 2l+3\ \ 2l+1}$$

$$l-1,m+1\ C_{+1}^{(1)}\ l,m\ =-\ \frac{l-m\ \ l-m-1}{2\ 2l-1\ \ 2l+1}$$

$$l+1,m-1\ C_{-1}^{(1)}\ l,m\ =\ \frac{l-m+2\ \ l-m+1}{2\ 2l+3\ \ 2l+1}$$

$$\langle l-1, m-1 \mid C_{-1}^{(1)} \mid l, m \rangle = -\sqrt{\frac{l+m}{2}\,\frac{l+m-1}{2l-1}\,\frac{}{2l+1}}$$

for circular polarized light. Since all other dipole matrix elements are zero, we can "read off" the dipole selection rules for transition between initial state n, l, m_l, s, m_s and final state n', l', m'_l, s', m'_s, they are[6]:

$$\Delta l = l' - l = \pm 1$$
$$\Delta m_l = m_l' - m_l = q = 0 \; or \; \pm 1$$

and from the spin part:

$$\Delta s = s' - s = 0$$
$$\Delta m_s = m'_s - m_s = 0$$

where q refers to the angular momentum of the incoming photon $l_p = q\hbar$. This picture is only valid for a single atom, but when dealing with atoms in solids, where ligand field, atomic bonding, exchange and spin orbit effects have to be considered, the wave function can be written as linear combination of the atomic basic function used here[6], e.g. in Figure 4 where we included the spin-orbit interaction which does not affect the selection rules. In general, when dealing with X-ray absorption in solids, we have to consider the sample orientation, the X-ray polarization and an external magnetic field, if applied. Done correctly, we can extract important information of our sample, e.g. the number of holes in the valence band or the magnetic moment per atom[6]. In order to obtain meaningful data, we have to acquire the orientation averaged resonance intensity I_{res} (which is, as we saw earlier, the energy integral over the absorption cross section). This can be done in several ways; first we can use a polycrystalline nonmagnetic sample where the grains are randomly oriented with respect to the incoming X-ray polarization. Second, for a nonmagnetic single crystal sample with higher than monoclinic symmetry (axes orthogonal) we can average three measurements along the principle axes x,y and z or one direction with all three, linear positive circular and negative circular polarization. In case of perfect cubic symmetry the spectral intensity is isotropic and thus requires only one measurement. Finally, for magnetic single crystals, linear light can be used and averaged over 3 axes or the sample can be saturated parallel and antiparallel to the direction of the circular polarized light (positive or negative) and then averaged over both. When done correctly the (angle averaged) resonance intensity obeys the very important so called "sum rule"[6]:

"The *angle-averaged intensity* of the combined L_3 and L_2 resonances is directly proportional to the total number of d states above the Fermi level, i.e., the number of holes in the d band."

When the magnetic field is included in this picture, the absorption and thus the sum rule can be made spin dependent, effectively yielding information about the difference in spin up and spin down holes which is the magnetic moment per atom in the sample[6]. The number of holes obtained in this way corresponds to the number of holes in the *ground state* of the atom, even though we measure the excited state, this is not obvious from this derivation, but can be proven in a more general configuration[6].

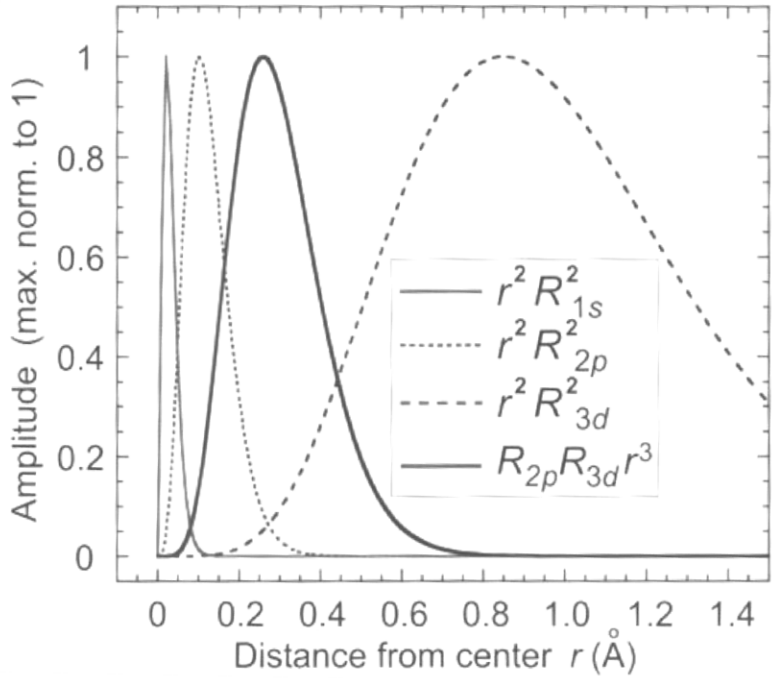

Figure 5: Radial functions for the 1s, 2p and 3d orbitals of the Mn^{2+} ion (probability of finding the electron at distance r from the nucleus) and the radial part of the dipole matrix element $R_{2p}R_{3d}r^3$ for the transition $2p \rightarrow 3d$. All functions are normalized to 1. (From ref [6])

2.2.3. Beamline 6.3.1 and the New Fast-Scan / Mapping Capability

Most of the research conducted for this thesis involved XAS, performed mainly at beamline 6.3.1 at ALS. Beamline 6.3.1 is a bend-magnet beamline in the 6th sector of the synchrotron using the 3rd bend magnet of this bend section and is the first beamline on this bend magnet. It is labeled 6.3.1, whereas beamline 4.0.2 is in the 4th section, using the undulator in the straight part (denoted by the 0) and is the second beamline at ALS, sharing the beam with another station. It was fully operational in March 2000 and is designed as a user friendly beamline for EUV and soft X-ray reflectometry, scattering and aborption experiments[8]. It has a differential pumping system to allow the parts upstream of the end-station to stay at 10^{-10} Torr, whereas the end-station can reach up to 10^{-7} Torr. This, together with a very fast pump down time, enables switching of samples in approx. 30 min, increasing the effective time that can be used to measure samples. A schematic overview of the beamline is shown in Figure 6 (from Ref [8]):

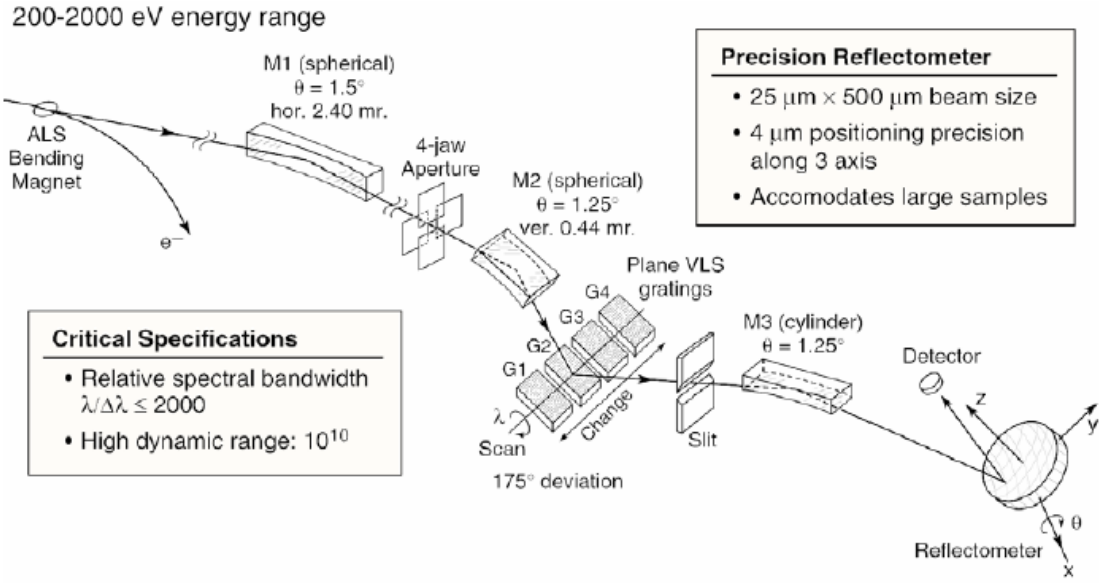

Figure 6: Schematic overview of beamline 6.3.1 at ALS with the most basic characteristics.

The most interesting feature of this beamline is the lack of an entrance slit to the monochromator (the 4-jaw aperture only defines the incoming beam size) which is a plane variable line spacing (VLS) grating of the Hattrick-Underwood type[8]. This type of grating does not require a movable exit slit to maintain its energy resolution due to its focusing capabilities but the exit slit has to be high precision due to the small beam divergence after the grating and can be actuated and position sensed with 0.1 μm accuracy[8]. This allows the monochromator to reach the resolution limit, determined by the ALS vertical beam size (vertical source size). The monochromator consists of 4 VLS gratings made of fused silica, coated with Au (for better adherence a Cr interlayer was deposited as well) which can be placed in the beam and have central grove densities of 240, 600, 1200 and 2400 lines/mm. As shown in Figure 7, each grating has a different

optimal energy range with respect to brightness (photon flux) and resolution. In general, resolution decreases with decreasing number of lines/mm for a given energy range.

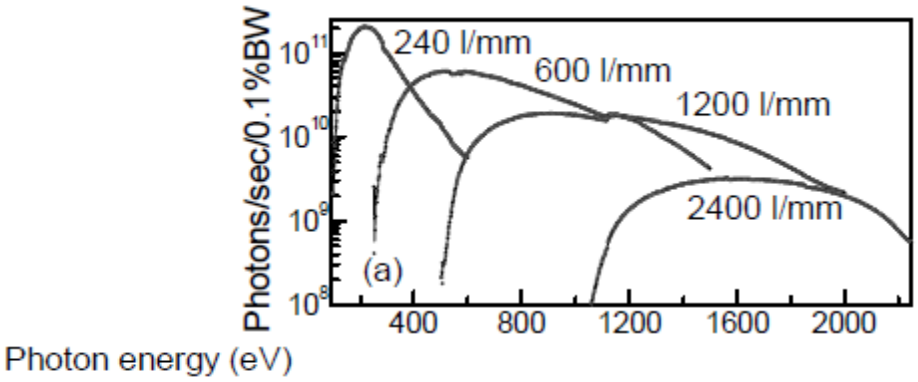

Figure 7: Photon flux vs. photon energy plot for all 4 VLS gratings used at beamline 6.3.1[8].

The energy range of this beamline is approx. 200-2000 eV with a spectral resolution of $\lambda\ \Delta\lambda \cong 2000$ when using the 600 or 1200 lines/mm gratings[8]. To obtain a XAS spectrum as seen in Figure 8, the energy of the incident beam is scanned across the absorption edge of interest by changing the angle of the line grating with respect to the X-ray beam. The energy, selected by the stationary exit slit is determined from the position of the grating. The position is changed using a motor, read out and referenced to obtain the energy plotted on the x-scale (Figure 8). Energy shifts in the spectrum due to shifts in the electron beam lattice are thus possible and care has to be taken when comparing peak positions (see Chapter 2.1.1.). In normal scan mode, for each energy step, the grating is moved, read out and the intensity measured for the preset time. This is repeated for each energy step (also preset) and can take from 0.5 to 2 sec, if additional motors have to be moved, e.g. entrance and exit slits, polarization and applied magnetic field. Depending on the beamline and measuring time per step, a L_{23} spectrum of a typical transition metal like Ni takes between 13 and 18 minutes, as shown in Figure 8 regular scan (black). Normally, this time cannot be decreased without losing resolution since the moving times for the grating, slits, polarization and magnetic field are fixed. Thus, the only way to increase the speed is by reducing the integration time, decreasing intensity and resolution. The absence of moving entrance and exit slits at beamline 6.3.1 enables the acquisition of a XA spectrum with only moving one motor – the grating angle. This makes this beamline ideal for a new concept of XAS data acquisition implemented by Elke Arenholz, Senior Staff Scientist at ALS. Rather than moving the grating to the new energy, stopping, acquiring data and then move the grating again, it is scanned continuously from preset start to stop energies. The XA signal is acquired by integrating over a preset period of time and assigning the thus acquired data point to the average energy the grating was at. A sample spectrum can be seen in Figure 8, flying scan (red line). The scan has to be optimized with respect to scan speed and integration time, effectively giving a time per data point that is pure integration time. Note that the integration times in Figure 8 for regular and flying scan are only a factor of 2.5 different, whereas the total scan time is reduced by a factor of ~9. This difference shows that most of the reduction comes from elimination of waiting time between steps. In theory, this is also possible for beamlines where the exit slits or (at an undulator) the undulator gap has to be moved simultaneously,

but is much more difficult since all those motors have to move in perfect synchronization. (Efforts are made by Elke Arenholz to implement the fastscan at beamline 4.0.2 as well.) This faster scan mode without sacrificing resolution, enabled the studies presented in the experimental part of this thesis (Chapter 5). The idea is to obtain a map of samples with cm dimensions where each data point consists of a complete XAS scan. Having full XA spectra facilitates the extraction of chemical information over the entire sample surface. The resolution of the so obtained chemical map is only determined by the X-ray beam dimensions. At beamline 6.3.1 the minimum beam size on the sample is approximately 25 x 500 µm but usually has to be increased depending on the sample and integration time to have sufficient signal to noise ratio. Additionally, this beamline has a fully automated x,y and z positioning system which enables the data acquisition to be fully automatized. For the example shown in Figure 8, the mapping of a 1 x 1 cm sample with 200 data points "pixels" in normal mode would take approximately 44 hours, not including the sample movement. Fast scanning reduces the acquisition time to 5 hours, making this type of study feasible, since the normal beamtime available to users is on the order of 3-5 days.

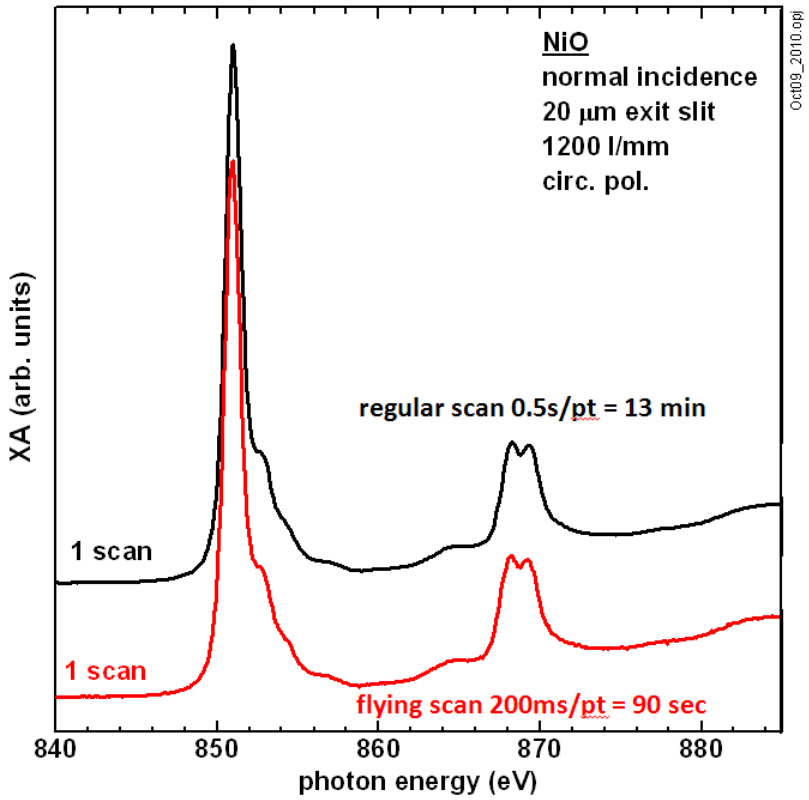

Figure 8: Comparison of normal (black) and fast (red) energy scan of the Ni L_{23} edges in a NiO sample (courtesy of Elke Arenholz, ALS). The fast scan is ~9 times faster at equal resolution.

Now multiple samples and edges can be scanned during one trip, greatly increasing the versatility of the beamline and types of studies possible. Especially another type of spectroscopy – X-ray magnetic circular dichroism (XMCD) where the sample is magnetized and measured with circular polarized light, is sped up dramatically. Instead of switching the magnetic field between parallel and antiparallel for each data point, a complete spectrum is taken at each (constant) magnetic field, decreasing the measurement

time even further. This new way of taking XAS and XMCD data is most beneficial for a user facility like ALS where available beamtime is of utmost concern for both administration/staff and users.
Unfortunately, this method of acquiring XAS spectra cannot be easily used at other beamlines, making 6.3.1 currently the only beamline with this capability (to my knowledge). As mentioned above, the difficulty in using other beamlines in this mode is to move multiple beamline components (motors) synchronous, each at its own required speed. For the undulator beamline 4.0.2 this would mean to move the premirror height, premirror angle, grating angle, EPU (elliptical polarizing undulator) gap and EPU phase which is naturally very difficult to do reliably without changing e.g. the energy resolution, polarization, energy per integration step or even the actual energy of the X-ray photons (since this is computed from the position of the grating alone using reference measurements). This makes beamline 6.3.1 a unique and valuable component of the Advanced Light Source by increasing the measurement mode possibilities and enabling a new and exciting way to perform spatially resolved X-ray spectroscopy in the hundreds of μm range.

2.3. Fuel Cells

In the following part the fundamentals concerning fuel cell systems, both their application and operation are presented. After an introduction to the different types of fuel cells and examples of their use, the basic work principles of Solid Oxide Fuel Cells (SOFCs) are explained. The emphasis lays on the difference between oxygen conducting and hydrogen (proton) conducting SOFCs and the material challenges faced.

2.3.1. Overview Fuel Cell Types

Fuel cells are solid state devices that convert chemical energy into electric energy via chemical reactions. Like all electrochemical devices, its main components are current collector, cathode, anode and electrolyte. Since there are no moving parts, their main advantage is silent, efficient, and maintenance free operation which makes them ideal for applications in urban areas and consumer electronics. Efficiencies of 60% electric and 80% with combined use of heat and electricity are already achieved[1]. To distinguish between the different types of fuel cells, it is convenient to use a classification according to the type of electrolyte since it determines most of the other properties of the cell, e.g. operating temperature, basic design and material of the electrodes and therefore the most useful and typical applications. In Table 1 the most common types of fuel cells are shown using the electrolyte as distinction. Alkaline Fuel Cells (AFCs) were the first ones to be commercially used by NASA during its space missions and they are in use on board of space shuttles[1]. Molten Carbonate Fuel Cells (MCFC) and Phosphoric Acid Fuel Cells (PAFC) use liquid electrolytes that are immobilized in a porous alumina matrix and are the only ones currently used on a larger commercial scale, i.e. most units sold prior to 2001 were PAFCs[1].

	AFC	DMFC	MCFC	PAFC	PEMFC	SOFC
Electrolyte	Potassium hydroxide	Polymer membrane	Immobilised Liquid Molten Carbonate	Immobilised Liquid Phosphoric Acid	Ion Exchange Membrane	Ceramic
Operating Temperature	60-90ºC	60-130ºC	650ºC	200ºC	80ºC	1,000ºC
Efficiency	45-60%	40%	45-60%	35-40%	40-60%	50-65%
Typical Electrical Power	Up to 20 kW	< 10 kW	> 1 MW	> 50 kW	Up to 250 kW	> 200 kW
Possible Applications	Submarines, spacecraft	Portable applications	Power stations	Power stations	Vehicles, small stationary	Power stations

Table 1: Classification of fuel cells by electrolyte type [1].

Polymer Exchange Membrane Fuel Cells (PEMFCs), also called Proton Exchange Membrane Fuel Cells, operate at low temperatures and they are able to utilize liquid fuels, e.g. methanol in Direct Methanol PEMFCs (DMFCs), making them perfect for smaller

applications like Laptops or vehicles especially since they can adapt quite well to varying power needs during operation[1]. Solid Oxide Fuel Cells (SOFCs) have strong application potential in stationary power production in a decentralized power grid or to increase the efficiency of existing power plants. Another advantage is the non-toxicity of the used cell materials. Since the operating temperatures are quite high, non noble metal catalysts can be used instead of the usual platinum in low temperature fuel cells reducing production costs dramatically and guarantee scalability.
However, a disadvantage is the still high degradation rate due to fuel impurities, material poisoning originating from other cell components and material decomposition due to thermal and chemical stress, which are discussed in the next section (section 2.3) in detail. As stated in the motivation chapter, the advantage of SOFCs is their autocatalytic property enabling the use of natural "fossil" fuels like natural gas and gasified coal, but also natural "renewable" energy sources like methane or other fuels generated using biomass, algae or bacteria. These possible applications in mind, the challenges faced are usually of material degradation nature and investigation of the fundamental mechanisms in these systems is not only advantageous for the commercialization of SOFCs but also for many other applications in the energy production and storage sector using the same or similar materials. Ceramic materials used in SOFCs are also used in Solid Oxide Electrolyser Cells (SOECs), Batteries and Super-capacitors under similar electrochemical environments, such as high ionic currents trough interfaces, overpotentials, gaseous and aqueous reactions at surfaces and many more, leading to the same problems regarding material and interface stability faced in SOFCs. Thus, the basic research on these materials is not only applicable to SOFCs in particular, but also to the whole class of application using these materials under similar or sometimes even quite different operating conditions. Understanding the underlying mechanisms of the adverse effects on the materials of interest is crucial for the development of successful mitigation strategies that enable the broad employment of fuel cell technology which can be an important pillar for the worldwide switch to and implementation of renewable energy sources.

2.3.2. Solid Oxide Fuel Cells (SOFCs)

As stated in the previous section, SOFCs use ceramic components and operate at higher temperatures than other fuel cell types. Even though the trend is to reduce the operating temperature in order to minimize thermal stress of the components during thermal cycling and between components with different coefficients of thermal expansion, the high operating temperature allows the use of inexpensive non-precious metal catalysts without sacrificing the autocatalytic activity of the system. The main reason for this high operating temperature is the ionic conductivity of the electrolyte, which puts a lower limit on the temperature since it originates in thermally stimulated hopping of the ion species that is conducted. Even though all SOFCs have the same principal components, it is again the electrolyte that can be used for distinguishing two main categories of SOFCs: oxygen conducting SOFCs and proton conducting SOFCs. Figure 9 shows a schematic of both types, with the actual fuel cell parts being anode, electrolyte and cathode. The current collector which is used in planar fuel cell designs to connect single cells in a stack, provide gas flow and connect the external wires and seals, is not shown in this simplistic model. This current collector is usually made of stainless steel or metals of similar elemental composition since it combines thermal stability, good conductivity, easy machinability, low cost and corrosion resistance but can be the source of contaminants that can be detrimental for the performance of the fuel cell itself. Successful attempts to

circumvent the use of this metallic interconnect were made by Siemens, by using a tubular rather than a planar design and are very successful[9]. However, the higher costs of all ceramic cells and lower current collection efficiency of ceramic interconnects are still problems in the tubular design and promote the development of the cheaper planar fuel cells.

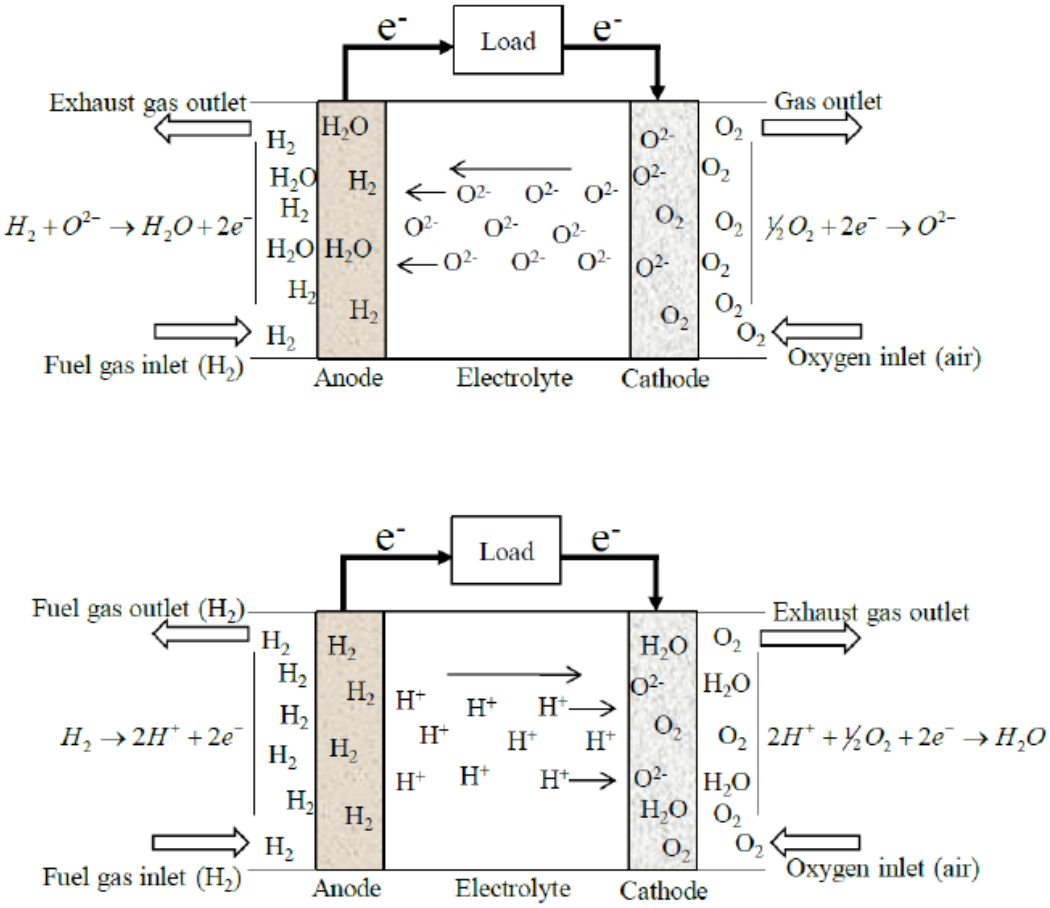

Figure 9: (top) schematic of an oxygen conducting SOFC with the summary chemical reactions, (bottom) schematic of a hydrogen conducting SOFC with the summary chemical reactions. (from[10])

Since the electrolyte does not conduct electrons, the electrons generated and used by the chemical reactions at anode and cathode, respectively, have to travel through an external load where they can be used for electrical work. Thus, both types convert a chemical potential into an electrical potential but as seen in Figure 9, different chemical reactions are involved. For the oxygen conducting SOFCs (top) the electrolyte (e.g. $Gd_xCe_{1-x}O_2$, GDC) conducts oxygen ions, produced at the cathode (air) side, to the anode side where they combine with hydrogen (fuel side). The disadvantage associated with this type is the dilution of the fuel with the produced water vapor, making recycling, cleaning and reintroduction of the fuel necessary. The lack of this disadvantage is also the main advantage of the hydrogen conducting fuel cell (bottom) where hydrogen dissociates at the anode (fuel) side, is transported across the electrolyte and associates with oxygen at the air side to form water vapor. Thus, there is no dilution of the fuel, making it the

superior type with regard to fuel preparation and recycling. However, when comparing the overall production cost and material stability, oxygen conducting SOFCs are far superior since the materials used are much cheaper in production, manufacturing of the cell and last longer in the harsh electrochemical environments existing in SOFCs and first commercial products based on oxygen conducting SOFCs are already available (e.g. Siemens tubular fuel cells or the Bloom "box"). One huge barrier for commercialization is the still rather large degradation of SOFCs that even in state of the art SOFCs today can be up to 1% per 1000 hours of operation, which is unacceptable for a target lifetime of about 40,000 hours[11, 12].

2.4. Degradation Mechanisms of Solid Oxide Fuel Cell Cathodes

In the following part a more specific motivation for the research conducted during the last three years is given, reasoning why the specific topics were chosen and why they are important to the scientific community. As stated in the previous section, various types of degradation are mitigating fast and broad implementation of SOFCs. Therefore, the fundamentals of two major types of cathode degradation, Cr poisoning and cation segregation, and their underlying mechanisms are presented in the following section, representing their current level of understanding in the literature.

2.4.1. Cr and Other Gaseous Poisoning

As outlined earlier, the production cost of a fuel cell unit is of major concern and great efforts are being made to keep them as low as possible. On one hand, precious metals are great catalysts and are chemically stable in a variety of oxidizing or reducing environments, even when simultaneously exposed to high temperatures. However, due to their limited availability material prices are rather high. On the other hand, transition metals are abundant and thus cheap, but have (slightly) lower catalytic activities and are typically severely affected by oxidizing environments and high temperatures. Especially as current collectors (with gas flow channels) and sealing materials transition metals are cheap in production and machining and extensive knowledge, infrastructure and production capabilities are readily available. This difference between precious and transition metals leads to a conflict between low production cost and long term stability (low degradation) where great effort is made toward finding the sweet-spot where both are ideal for mass-production and wide implementation of fuel cells into everyday life. Siemens successfully developed a SOFC using only ceramic materials[9], even as current collector, but machining is complex and thus production costs are relatively high. A much cheaper way is the production of planar SOFCs using stainless steel as current collector and interconnect between cells since gas flow channels can easily be machined into it and the coefficient of thermal expansion can be matched to the ceramic anode/electrolyte/cathode membrane by adding the appropriate amount of Cr; such special stainless steels are now commercially available, e.g. Thyssen Krupp's Crofer 22 [13]. However, this advantage comes with a drawback: the protective chromia layer, forming at high temperatures in oxidizing environments, protects the underlying steel from oxidation but is slowly evaporated. The lost Cr can easily be replenished from

within the steel but the gaseous Chromia species introduced into the cell can now react with the other cell components or deposit in critical regions leading to performance degradation. This phenomenon has been investigated by many authors[14-18] for almost two decades now and is a well known problem in SOFCs using stainless steel components.
All authors agree on the Cr evaporation mechanism from the interconnect where solid Cr^{3+} in the form of Cr_2O_3 is converted into gaseous Cr^{6+} species, mainly by following these two reaction paths[14]:

$$\frac{1}{2}\mathrm{Cr_2O_3}\ s\ + \frac{3}{4}\mathrm{O_2}(g) + \mathrm{H_2O}(g) \rightarrow \mathrm{CrO_2\ OH\ _2}(g)$$

$$\frac{1}{2}\mathrm{Cr_2O_3}\ s\ + \frac{3}{4}\mathrm{O_2}(g) \rightarrow \mathrm{CrO_3}(g)$$

The first reaction occurs predominately in moist air, forming the Cr^{6+} oxyhydroxide whereas the second reaction occurs predominately in dry air thus forming CrO_3. Since most air fed to the fuel cell contains some moisture, both reactions occur with the water content dictating the partial pressure of each component as shown in Figure 10. In the following part we will use the oxyhydroxide equation, neglecting all others, but note that all reactions can also take place when CrO_3 is present.
Once the hexavalent Cr is formed, it is transported by the gas stream through the cell and diffuses into the pores of the cathode. This in itself is not detrimental to the cell performance. However, when gaseous Cr is converted back to solid Cr_2O_3 and deposited on the cathode, in the pores and on the electrolyte, it now acts as a barrier for the oxygen reduction reaction and oxygen transport[14] (just as it did on the interconnect, where it protects the steel from corrosion). As mentioned earlier, vaporization of Cr at the interconnect is well understood and accepted, but the underlying mechanism for the re-deposition remains a controversy in the literature.
Two main concepts are emerged to explain the various experimental results obtained for different Cr deposition experiments. On the one hand some authors[15, 16] propose an electrochemically driven re-deposition of the gaseous Cr species at the three phase boundary (TPB, the points where all 3 phases of the cathode side of a fuel cell meet – air, electrode and electrolyte) which competes with the oxygen reduction reaction. The re-deposition reaction is in the following form:

$$2\mathrm{CrO_2\ OH\ _2}\ g\ + 6\mathrm{e^-} \rightarrow \mathrm{Cr_2O_3}\ s\ + 2\mathrm{H_2O}\ g\ + 3\mathrm{O^{2-}}$$

and since it depends on the amount of electrons available, the deposition rate increases with increasing polarization of the cathode (drawn current of the cell) which was experimentally observed.

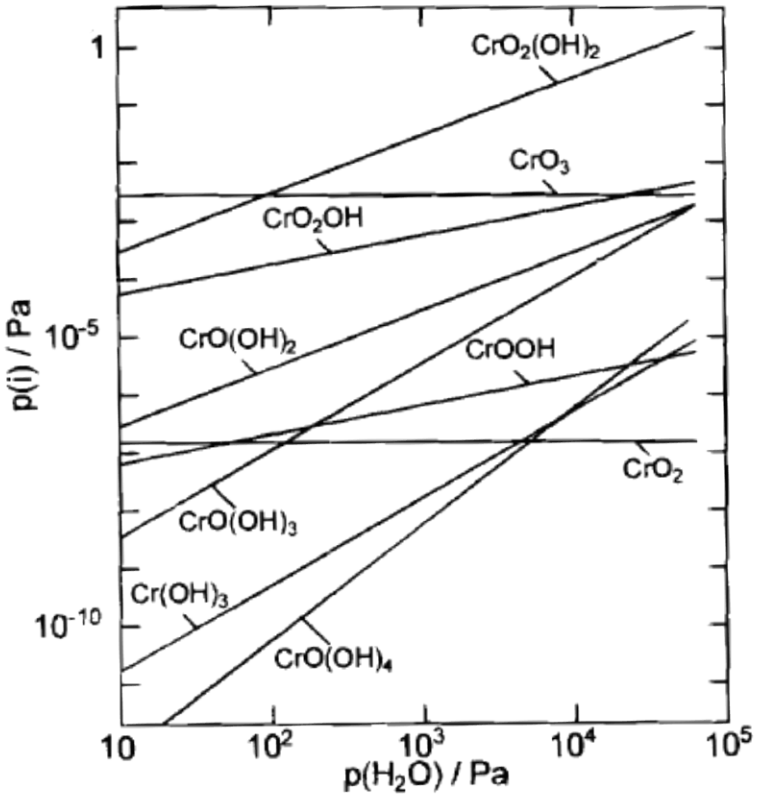

Figure 10: Partial pressures of various gaseous Cr species over solid Cr_2O_3 at 1223 K versus the partial pressure (content) of water in humid air (from Ref[14]) .

On the other hand some authors[17, 18] found evidence that the re-deposition is a nucleation governed reaction, independent of electrochemical sites (TPB) but facilitated by nucleation agents existing in the materials used at the cathode side. The re-deposition thus occurs all over the material, containing the nucleation agent, which was also experimentally observed. The reaction in case of a $La_{0.6}Sr_{0.4}Co_{0.2}Fe_{0.8}O_{3-\delta}$ (LSCF) cathode would be[17]:

$$\mathrm{CrO_2\ OH\ _2\ } g\ + \mathrm{SrO\ } s\ \rightarrow \mathrm{Sr-Cr-O}_x\ nuclei\ + \nu \mathrm{H_2O\ } g$$

$$\mathrm{Sr-Cr-O}_x\ nuclei\ + \mathrm{CrO_2\ OH\ _2\ } g\ \rightarrow \mathrm{Cr_2O_3\ } s\ + \nu \mathrm{H_2O\ } g$$

$$\mathrm{Sr-Cr-O}_x\ nuclei\ + \mathrm{CrO_2\ OH\ _2\ } g\ + \mathrm{SrO\ } s\ \rightarrow \mathrm{SrCrO_4\ } s\ + \nu \mathrm{H_2O\ } g$$

where y and ν are stoichiometric constants. After forming the initial nucleus with SrO, segregated at the surface (first reaction), the subsequent reactions can either produce Cr_2O_3or $SrCrO_4$, both being observed in experiments[17]. The discrepancy between the two theories and the inability to definitively rule out one or the other via experiments shows the difficulty in extracting the underlying mechanisms of degradation in the complex system of solid oxide fuel cells, where a variety of conditions and materials can have major effects on the observations made in experiments. In a review on this matter, J. W. Fergus[19] points this out nicely: "Poisoning of SOFC cathodes occurs by gas-phase transport of chromium from the interconnect material, but the amount and location of the

Cr_2O_3 deposit depends on the properties of the electrode and electrolyte materials. Chemical deposition (i.e. with no electrochemical polarization reaction) of Cr_2O_3 can occur and is affected by the substrate material, which may be due to thermodynamic and/or catalytic properties of the electrode material. However, the deposition process is also affected by the presence of cathodic polarization, so electrochemical reactions, either directly or indirectly, affect the deposition."[19].

The impact of Cr_2O_3 the on cell performance however, is negative in either case, making Cr poisoning the main reason that stainless steel interconnects are inferior to fully ceramic ones. To obtain a better understanding of the impact of Cr_2O_3 deposition on the performance of individual cell components (cathode and electrolyte), in Chapter 3 of this thesis the impact of Cr_2O_3 on the oxygen exchange at the surface of the cathode material LSCF and the electrolyte material $Y_xZr_{1-x}O_2$ (YSZ) is discussed[20]. The research presented there investigates the critical thickness that Cr_2O_3 deposits can have before they are detrimental to the performance of the material and thus give guidelines for mitigation strategies. To reduce the Cr poisoning in SOFCs, multiple strategies are explored and show promising results. One strategy relies on elimination of nucleation agents in the cathode material, e.g. the Sr or Mn, and by tailoring the composition of the electrolyte and cathode, Cr tolerant cells were made possible[17]. Possible drawbacks might be of inferior chemical stability with respect to thermal and redox cycling of the cell or higher material decomposition rates at elevated temperatures, as well as higher costs. Another strategy is to prevent the formation of the gaseous Cr species in the first place via application of protective coating to the stainless steel. Here, the coating acts as a diffusion barrier for the Cr and can consist of e.g. a $CoMn_2O_4$ spinel or nano-layered materials engineered for high oxygen and chromium diffusion blockage[21]. The drawback of this method is the sometimes low adherence of the coating to the substrate, especially under thermal stress and the possibly of high degradation of the coating itself, leading to cell or stack failure. Overcoming these drawbacks is essential for successful implementation of cheap stainless steel interconnects into commercially available solid oxide fuel cells and shows the importance of investigating the fundamental mechanisms of cathode degradation due to Cr poisoning.

2.4.2. Cation Segregation in Perovskites

Another known degradation mechanism in SOFCs is the decomposition of and secondary phase formation in the perovskite cathode. While the first fuel cells consisted of platinum electrodes that were in direct contact with the electrolyte (consequently forming the three phase boundaries at the point of contact, mentioned in the previous chapter) and facilitated the oxygen reduction[22], modern cells have ceramic anodes and cathodes. Whereas the anode often consists of Ni particles embedded in a matrix of the electrolyte ceramic [23], the cathode often consist of a perovskite of the type ABO_3. Most widely used are perovskites with La in the A site and Mn or Fe in the B site which additionally can be doped with Sr (A-site) and Co (B-site). Historically the electrolyte YSZ was used in combination with $La_{1-x}Sr_xMnO_3$ (LSM or LSMO) which is considered almost pure electronically conductive[24], resulting in very small active regions for oxygen reduction[25] (essentially being just the TPBs). Fuel cell performance was increased by switching from Mn to Fe and co-doping the B-site with Co resulting in $La_{1-x}Sr_xCo_yFe_{1-y}O_3$ (LSCF or LSCFO). The observed increase in cell performance was attributed to the mixed conductivity of LSCF, meaning it is both an electric and ionic conductor[26, 27]. Many other mixed conducting compounds were discovered and are now commonly referred to as MIECs (mixed ionic electronic conductors). At operating temperature, this mixed conductivity extends the TPBs from quasi-two dimensional (Figure 11b) up to several µm beyond the actual point of contact[22, 27, 28] thus greatly enhancing the surface available for the crucial oxygen reduction reaction (Figure 11a). In Figure 11, the extension of the active region for oxygen reduction is shown for materials with low ionic conductivity (left hand side) and high ionic conductivity (right hand side) and demonstrates quite nicely the extent beyond the TPBs for both cases.

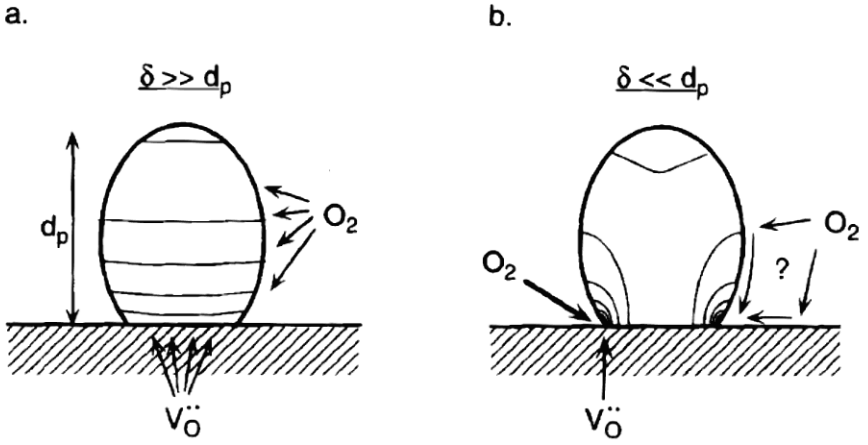

Figure 11: Extent of the active region δ participating in the oxygen reduction reaction for cathode materials with a) high ionic conductivity (reaction zone δ much larger than average particle size d_p) and b) low ionic conductivity (reaction zone δ much smaller than average particle size d_p) demonstrating that in the latter case it is mostly confined to the TPBs. (the lines represent the expected oxygen vacancy $V_O^{\cdot\cdot}$ profile, from Ref [25])

However, this new class of material was showing the same or worse structural, surface and interface degradation compared to LSM. At the interface of LSM with the YSZ electrolyte, formation of strontium or lanthanum zirconates had to be reduced/avoided by choosing the appropriate doping levels[29, 30]. With the use of LSCF however, this problem was greatly enhanced and to maintain acceptable degradation levels, the electrolyte had to be switched to Gd doped Ceria ($Gd_xCe_{1-x}O_2$, GDC or CGO) which in general shows no interaction with perovskites at standard operating temperatures[29]. Application of GDC interlayers also showed effective in prevention of unwanted secondary phases[31] and shows the importance of identifying the degradation mechanism for development of successful mitigation strategies. However, the surface of the perovskite itself is not only susceptible to the Cr poisoning mentioned in the previous chapter, but also to segregation of the dopant Sr and formation of secondary phases like SrO which lead to significant degradation of the cell performance[32]. This structural degradation of the cathode material itself leads to a compromised electrical and ionic conductivity, especially at the surface of the perovskite[33], which is essential for oxygen reduction. Since the basic mechanism of this type of degradation is mostly unknown, the influence of the electrochemical environment present during cell operation is of tremendous interest as basis for developing degradation mitigation strategies and will be the focus of the scientific part of this thesis. To get a better understanding of the different aspects of structural degradation and the impact of the electrochemical environment on the cathode material during operation, the basics of cathode ionic and electronic conductivity will be explained here.

First, the origin of the electrical conductivity is of interest, as it ties directly to the oxygen ion conductivity and most oxides have very low electrical conductivities or are insulating. In case of the doped perovskites, LSM or LSCF, the electrical conductivity comes from doping with divalent Sr, thus substituting a trivalent La (thus acting as an acceptor dopant). Due to charge neutrality, the dopant has to be charge compensated, either by a change in valency of another cation e.g. Fe or Co in case of LSCF, or by anion vacancy formation. Which mechanism is preferred depends on the environmental conditions and was investigated thoroughly by Tai et al. [34]. The authors found that the temperature dependent electrical conductivity was following the relationship:

$$\sigma = \frac{A}{k_B T} exp \quad -\frac{E_a}{k_B T}$$

below a critical temperature which is also the equation for the small adiabatic polaron hopping mechanism[35]. A is a material constant and contains the charge carrier density, k_B is the Boltzmann factor, T the absolute temperature and E_a is the activation energy for the hopping process. After determining the critical temperature T_{max} where the exponential term dominates and the conductivity starts to decrease, the authors found that it decreased faster than expected from the equation above and the explanation they found is of interest both for the ionic conductivity observed in these materials and for the experiments discussed later and a brief summary shall be given here.
First, the acceptor dopant Sr has to be charge compensated, thus generating holes and making LSCF a p-type conductor. As mentioned earlier, which compensation mechanism, Fe or Co oxidation or O vacancy increase, is dominant depends on the temperature and it was found that for high temperatures, most of the Sr is compensated by oxygen vacancies. Furthermore the Co ions can disproportionate at high temperature[34], forming a Co^{4+} Co^{2+} pair from 2 Co^{3+}. The charge compensation to reach electro-neutrality can now be written (in Kröger-Vink notation[36]):

$$\mathrm{Co}_{Co}^{*} = Sr_{La}^{'} - 2\,V_{O}^{**} + d$$

where Co_{Co}^{*} is the concentration of Co^{4+} (for clarity * was used to indicate a positive charge instead of a small solid dot usually used, a negative charge is denoted by '), $Sr_{La}^{'}$ the concentration of the Sr acceptor dopant, V_{O}^{**} the concentration of oxygen vacancies and d the concentration of Co_{Co}^{*} from the disproportionation reaction. If we assume that all of the Sr is charge compensated by oxygen vacancies, additional oxygen vacancies will be charge compensated by reducing 2 Co^{4+} to 2 Co^{3+} and thus lowering the amount of charge carriers and thus the conductivity of the sample. In Figure 12 the oxygen content, electrical conductivity and Seebeck coefficient are shown. Above 600˚C we see the expected decrease in conductivity with decrease in oxygen content (increase in oxygen vacancies) and increase in Seebeck coefficient.

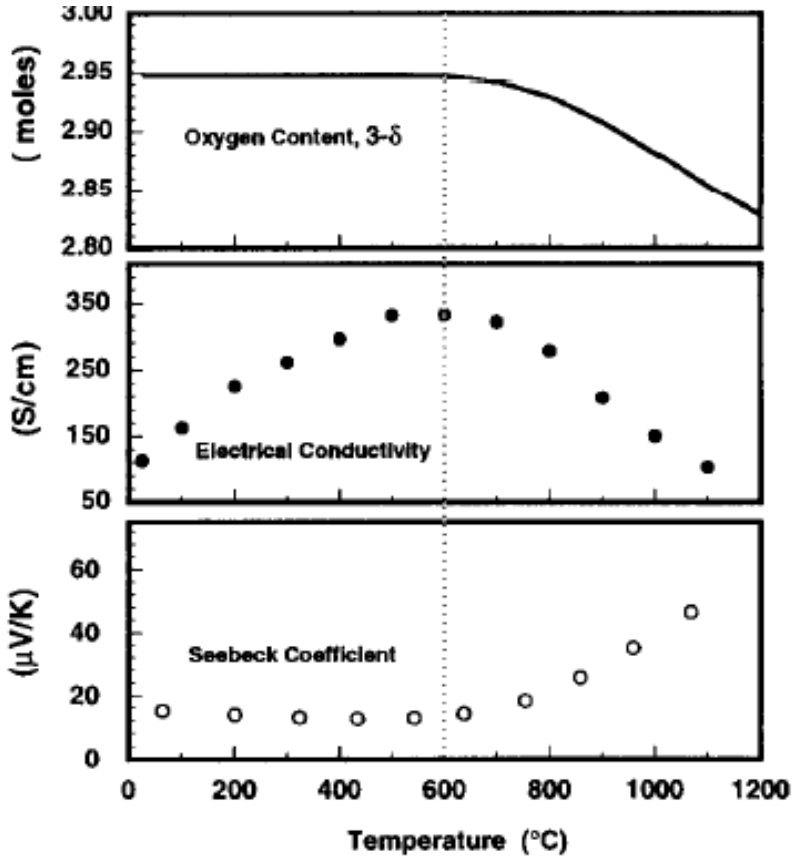

Figure 12: Oxygen content, electrical conductivity and Seebeck coefficient for $La_{0.6}Sr_{0.4}Co_{0.2}Fe_{0.8}O_{3-\delta}$ as function of temperature in air.

Using this concept explored by Tai et al. we can now draw conclusions about the amount of oxygen vacancies by measuring the concentration and oxidation states of the A and B cations. In Figure 13 the concentration of the different valence states of the B site cations are shown.

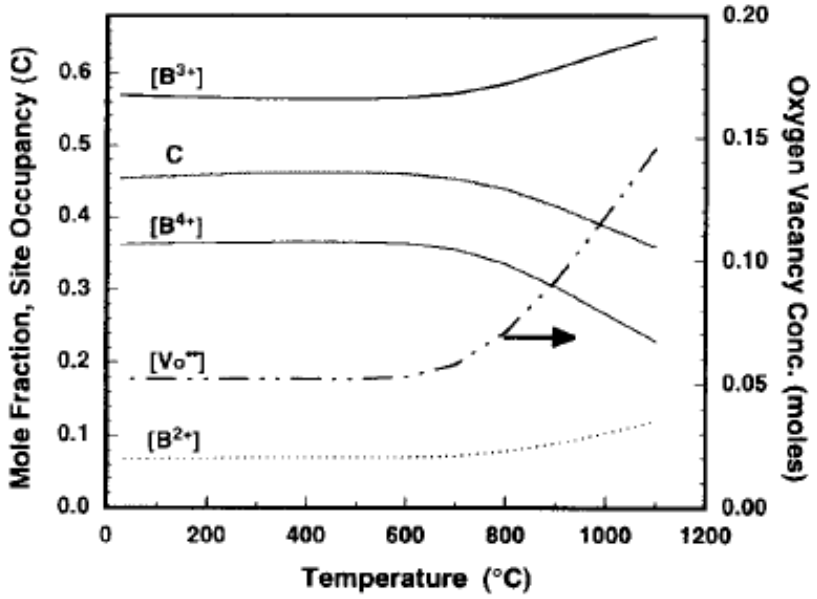

Figure 13: Mole fractions [B] of various B site ions, site occupancy C of the B site and oxygen vacancy concentration V_O^{**} for $La_{0.6}Sr_{0.4}Co_{0.2}Fe_{0.8}O_{3-\delta}$.

This demonstrates that the mole fractions of the 2+, 3+ and 4+ valent B-site ions track with the oxygen vacancy concentration as temperature is increased. We can now use this concept in order to draw conclusions about the amount of oxygen vacancies from measuring the valence state of the B-site ions. Normally, only a few techniques are able to measure the oxygen vacancy concentration, e.g. thermo gravimetric techniques as used by Tai et al.[34], and do not yield element specific information. Other techniques can be used to gain spatial information, like XPS or SEM, but they cannot measure oxygen vacancies. Whereas XPS can be used to determine oxidation states, it is much better in measuring local shifts in the work function, which can also be used to great effect in studying SOFC materials[37]. XAS can easily distinguish different oxidation states, but up to now was impractical to use for mapping due to the long scan time. By combining new XAS scanning techniques and applying the concepts presented in this chapter, a new way to map the oxygen vacancy distribution and thus the electro catalytic active regions on a sample will be explored in chapter 5 of this thesis.

Chapter 3

3. Chromium at the Surface and Interface of Electrolyte and Cathode

In this chapter, the impact of Chromium oxide layers on the oxygen uptake of electrolyte YSZ and cathode LSCF is discussed. To demonstrate the new scientific insight that was gained, the original peer reviewed experimental setup, results and discussions sections are printed (from[20]).

3.1. Effect of Cr_2O_3 on the ^{18}O tracer Incorporation in SOFC Materials

3.1.1. Introduction

As mentioned in the theoretical part of this thesis, Cr plays a major role in the degradation of SOFCs with stainless steel interconnects. One way to reduce degradation is to lower the operating temperature which in turn reduces Cr evaporation and thermal stress due to mismatching coefficients of thermal expansion (CTE) of different cell components. The problem hereby is to maintain performance and durability and investigations in this regard have been conducted for more than a decade now[38, 39]. Successfully reducing the operating temperature would not just enable the use of inexpensive metallic rather than ceramic interconnects [40], but also mitigate various other degradation effects [12]. "Examples from previous works include anode poisoning from fuel contaminants [23], interface degradation between the electrolyte and cathode layers [30, 41], and self-poisoning of the cathode by sealing and interconnect materials [17, 42]. Although degradation mechanisms for cell performance have been proposed for the anode (e.g. sulfur [23]) and for electrolyte/cathode interfaces [30, 41], a clear picture of the cathode degradation mechanisms due to poisoning from interconnect and sealing materials is still absent. Deposition of contaminants and reactions between SOFC materials forming non ion-conductive oxides (like $Sr_xZr_{1-x}O_2$ or Cr_2O_3) have been thought to be responsible for cathode degradation since the first cell stack tests with stainless steel interconnects were performed [14]."[20] Eliminating Cr from stainless steel interconnects is difficult, since18 – 22 wt% of Cr is necessary to match the CTE with the other cell components and the formation of a protective Cr_2O_3 layer makes the steel resistant to corrosion by the fuel cell environment in the first place. Since this Cr_2O_3 protective layer is the origin of the poisoning [15], mitigation strategies are being explored, mainly by application of other protective interconnect coatings [21]. $(Co,Mn)_3O_4$ spinels for example, can act as diffusion barrier for Cr from the bulk steel. However, a quantitative measurement of the effects of a Cr_2O_3 layer on the oxygen reduction and subsequent diffusion into the electrode or electrolyte of a cell is still absent.

In this part of my thesis, the effect of a Cr_2O_3 layer on the electrolyte material $Y_{0.15}Zr_{0.85}O_2$ (YSZ), and on the cathode material $La_{0.6}Sr_{0.4}Co_{0.2}Fe_{0.8}O_3$ (LSCF) is

investigated. Both materials are oxides but completely different in their electrochemical properties. ^{18}O tracer diffusion experiments were performed to investigate the impact of a Cr_2O_3 layer on the oxygen reduction at the surface and diffusion in the bulk of the material. The ^{18}O tracer diffusion profiles were extracted by TOF-SIMS at PNNL in collaboration with Zihua Zhu. Theoretical models by Lane and Kilner [43] predicted that the detrimental effect of Cr on the oxygen reduction stems from the lack of electronic species (electrons or holes) available on the surface. However, another mechanism could impede the oxygen reduction - secondary phase formation at the surface and thus a reduction in available oxygen vacancies, as commonly found e.g. in YSZ/LSCF [29] systems. To decide which mechanism is dominant, the solid-state reaction of both materials with Cr_2O_3 at operating temperature (800°C) and at sintering temperature (1400°C) was investigated using X-ray diffraction (XRD). In contrast to other degradations discussed in this thesis, this degradation is from the outside, demonstrating the multiple ways one has to consider in order to understand and de-convolute SOFC degradation. It also demonstrates the use of the standard technique in diffusion profiling – cross sectional SIMS and the necessity of combining it with other surface science techniques to obtain a complete picture of this degradation mechanism.

3.1.2. Experimental

Sample Preparation – All samples were prepared using commercially available powders, $La_{0.6}Sr_{0.4}Co_{0.2}Fe_{0.8}O_3$ (5.4 m^2/g) from Fuel Cell Materials (FCM) and $Y_{0.15}Zr_{0.85}O_2$ (TZ-8YS) from TOSOH. The powders were uniaxially pressed into pellets and sintered at 1400°C for 2 hours. Sample densities were measured by the Archimedes method using ethanol as submerging liquid and found to be ~98% theoretical density for YSZ, and ~95.4% theoretical density for LSCF with the remaining 4.6% consisting approximately of 1.6% open pores and 3% closed pores (an additional weight measurement of the wet sample with the assumption of only a very thin film of ethanol on the surface but all open pores filled with ethanol yielded the approximate value for open and closed porosity). XRD measurements showed no secondary phases. Subsequently, the samples were polished on both sides with SiC sandpaper (up to 1200 grit). All samples were annealed for 8 hours at 800°C in air, to achieve sample and surface equilibria after polishing. This annealing step ensures that appropriate boundary conditions are achieved for fitting Crank's solution to the diffusion equation [44] and extracting reliable oxygen diffusion and surface exchange coefficients.

Cr film deposition - The chromium deposition was performed by means of thermal evaporation on only one side of a subset of samples in a high vacuum chamber using a tungsten basket as evaporation crucible filled with 99.996% pure Cr flakes (Alpha Aesar). The base pressure in the chamber was $1\cdot$ and reached $\sim 5\cdot$ during the Cr depositions. A Cr film growth rate of approximately 1 nm/min was kept for all samples. To obtain uniform thicknesses, the Cr was grown simultaneously on LSCF and YSZ polished substrates as well as on a 0.5x0.5 cm piece of Si (100) with the native surface oxide intact. Sample sets with different Cr film thicknesses of 2.4, 5.4, 10.5, 12.6, 15.4 and 18.9 nm (as determined by Rutherford backscattering spectroscopy (RBS) on the Si specimen) were prepared.

To oxidize the Cr film prior to the ^{18}O experiment, every sample was annealed in air for 3 hours at 800°C. The RBS measurements showed that the films were completely oxidized and expanded to 3.6, 8.2, 16.3, 21.4, 29.8 and 38.1 nm which is in good agreement with the theoretically expected expansion value of 178%. The chemical state of the chromium oxide was determined using X-ray absorption spectroscopy (XAS in total electron yield mode) at beam line U4B of the National Synchrotron Light Source of Brookhaven National Laboratories. In Figure 14, the upper spectra represent two different thicknesses of the as-deposited Cr-films on Si after exposure to air. These two spectra represent the native oxide of the Metallic Cr films due to exposure to air since the escape depth of the electrons is very small (~nm), nevertheless most of the film is metallic. The lower spectra are from a Cr-film on Si after the oxidizing anneal and a 99% pure Cr_2O_3 reference powder (Alpha Aesar), demonstrating that the oxidized film is present as Cr_2O_3. The completeness of the Cr_2O_3 film on the LSCF and YSZ samples (polished) was ensured by EDX mapping of Cr and Fe in a 50x50 μm area in a field-emission scanning electron microscope image for the thinnest Cr_2O_3 film (3.6 nm) on a LSCF substrate. It showed a uniform Cr coverage demonstrating that the thin films are complete. The high resolution FE-SEM picture of an annealed sample showed a compact and crystalline film with grain sizes around and slightly larger than the film thickness (20 – 100 nm for the 29.8 nm Cr_2O_3 film).

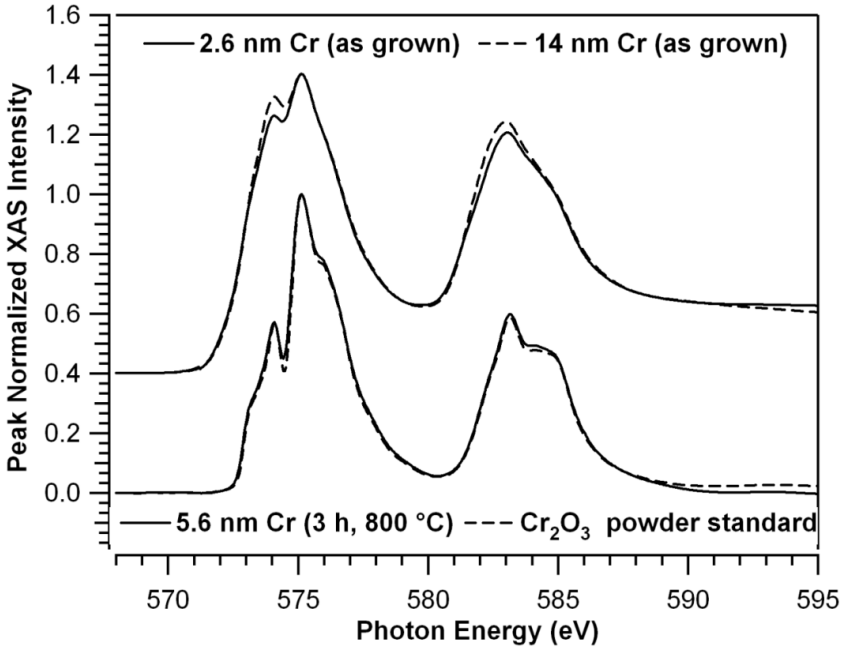

Figure 14: XAS spectra of the chromium $L_{2,3}$-edges of two as deposited Cr films after exposure to air (upper spectra, offset for clarity) and a film oxidized for 3 hours at 800°C (solid line of lower spectra). Also shown is a Cr_2O_3 powder reference (dashed line of lower spectra).

^{18}O tracer diffusion – A standard tracer diffusion setup was built, as in [45], in order to carry out the ^{18}O tracer diffusion experiments. A tube furnace with a quartz tube sealed at one end containing the samples was heated up to 800°C in air at ambient pressure. After annealing the samples for 3 hours the quartz tube was evacuated down to ~ $5x10^{-5}$ Torr

and a 1:1 isotopic mixture of ^{18}O and ^{16}O (from Icon Isotopes) was backfilled into the system to reestablish the initial standard O_2 partial pressure. The atmosphere was monitored using a quadrupole mass spectrometer (QMS) to detect possible ^{18}O depletion due to the isotopic exchange with the sample. Neither ^{18}O depletion nor a change of pressure in the quartz tube was observed. The exchange gas isotopic ratio was constant at 50% ^{18}O for all samples and all three species $^{16}O_2$, $^{18}O^{16}O$ and $^{18}O_2$ were equally abundant (within the detection limit of our QMS). After 30 minutes the oven was retracted from the quartz tube and the samples were quenched to ~100°C in approximately 2 minutes to minimize additional oxygen exchange.

Depth profiling by SIMS – The cross-sectional SIMS measurements were performed at Pacific Northwest National Laboratory (PNNL) using an IONTOF V ToF-SIMS spectrometer. A standard SIMS sample preparation was used [45] to measure the ^{18}O depth profile. All samples were cut in half using a diamond saw and the exposed cross-sections polished with SiC sandpaper (up to 1200 grit). To remove surface contaminations from the polishing, the cross-section was pre-sputtered with 1.0 keV Cs^+ ions until a steady state ToF-SIMS spectrum was achieved. Next, 25 keV Bi^+ ions were focused into a ~4 μm diameter spot and rastered over a 15×15 μm^2 area during data acquisition. Measurements were taken at 25 μm steps along the sample's cross-section. A low primary ion (Bi^+) current was used to avoid signal saturation ($^{16}O^- \leq 0.1$ counts per shot) with the noise level of the ^{18}O signal <0.01% of its peak intensity.

Solid state reaction with Cr_2O_3 – Additional experiments were conducted to ascertain that no substantial solid state interaction between Cr_2O_3 and YSZ or LSCF occurred. One-to-one volume ratio mixtures of Cr_2O_3 powder (Alpha Aesar, 99.9% pure) and powders of both materials of interest were prepared to determine the XRD patterns of any possible secondary phase formation. Each mixture was ground until a uniform color was achieved. For each mixture, 4 different pellets were uniaxially pressed. One pellet was sintered for 7 hours at 800°C, another for 14 hours at 800°C, and a third for 2 hours at 1400°C. Each pellet was then polished using diamond sandpaper (3M - 45 μm grains) and investigated by XRD.

3.1.3. Results

A typical ^{18}O depth profile obtained by cross section SIMS (symbols) and the corresponding fit according to equation 1 (solid lines) can be seen in Figure 15. The normalized concentration $C'\ x$ after a 30 min exposure at 800°C is plotted as a function of the depth, *x,* with the surface at x=0. Both, the bare side and Cr_2O_3 film side of one sample are displayed (here the Cr_2O_3 film is too thin to be represented on this scale). Since only one side of each pellet is coated with Cr_2O_3, the remaining bare side is used as the uncoated baseline reference. Comparing the diffusion coefficient, D_T, and the surface exchange coefficient, *k,* values of the bare side of each film thickness provides an easy check for repeatability and to ensure the differences in the effective surface exchange values are only due to the Cr_2O_3 layer. An important check on the appropriateness of the fitting procedure as well as the simplification for thin films (see *Discussion*) is that the extracted values for the diffusion coefficient, D_T, should be the same for both sides of the pellet, bare and Cr_2O_3 covered, because D_T represents a bulk property of YSZ and LSCF. In general, YSZ has a higher diffusion coefficient, D_T, but much smaller surface exchange coefficient, *k,* than LSCF. For both materials, constant D_T values and similar *k* values (of the bare sides) were extracted which are very close to those reported in the literature ($D_T =$ · · and $k =$ · · for LSCF [27] and $D_T =$ · · and $k =$ · · for YSZ [45]) .

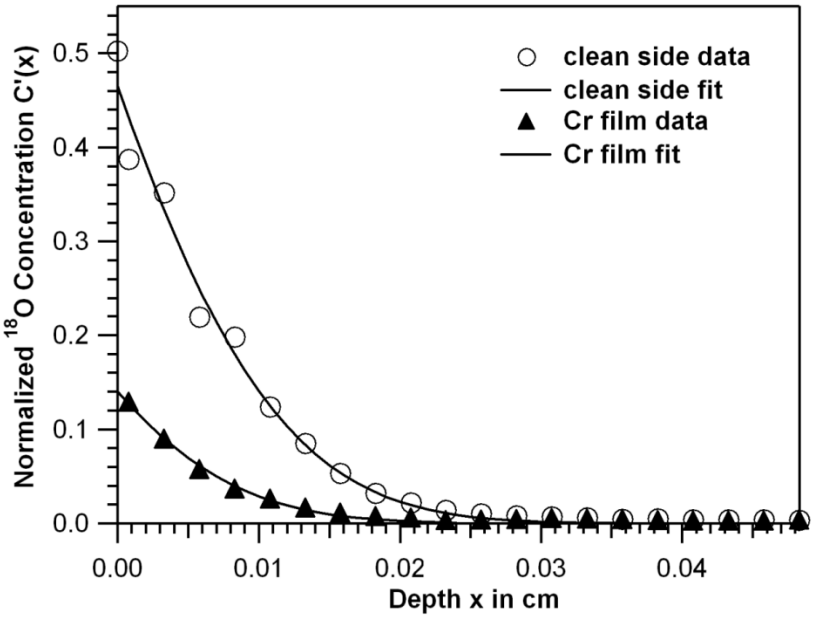

Figure 15: ^{18}O concentration depth profile and the corresponding fit for both sides of a LSCF pellet, one side uncovered (open circles) and one side covered by a 4.4 nm thick Cr_2O_3 overlayer (filled triangles).

3.1.4. Discussion

Diffusion parameters - For isotopic exchange anneals, the diffusion of the tracer through a solid gas interface into a semi-infinite medium is described by Crank's solution of the diffusion equation [46],

$$C'(x) = \frac{C(x,t) - C_{bg}}{C_{gas} - C_{bg}} = \operatorname{erfc}\left(\frac{x}{2\sqrt{D_T t}}\right) - \exp\left(\frac{k x}{D_T} + \frac{k^2 t}{D_T}\right)\operatorname{erfc}\left(\frac{x}{2\sqrt{D_T t}} + k\sqrt{\frac{t}{D_T}}\right)$$

where $C'(x)$ is the normalized tracer concentration, $C(x,t)$ the measured tracer concentration at depth x after annealing time t, C_{gas} the tracer concentration in the gas and C_{bg} the tracer's background concentration. This equation applies directly to the bare side of our samples since there is only the gas-LSCF or gas-YSZ interface. For the bare sides the surface exchange coefficient, k (in $cm \cdot$) and the diffusion coefficient, D_T (in $cm^2 \cdot$) represent intrinsic properties of the LSCF and YSZ which can be directly derived from (1) by fitting the measured ^{18}O tracer diffusion profile using a non-linear least square fit. The boundary conditions associated with this solution can be found elsewhere [44] and must be carefully maintained (e.g. constant ^{18}O concentration in the gas).

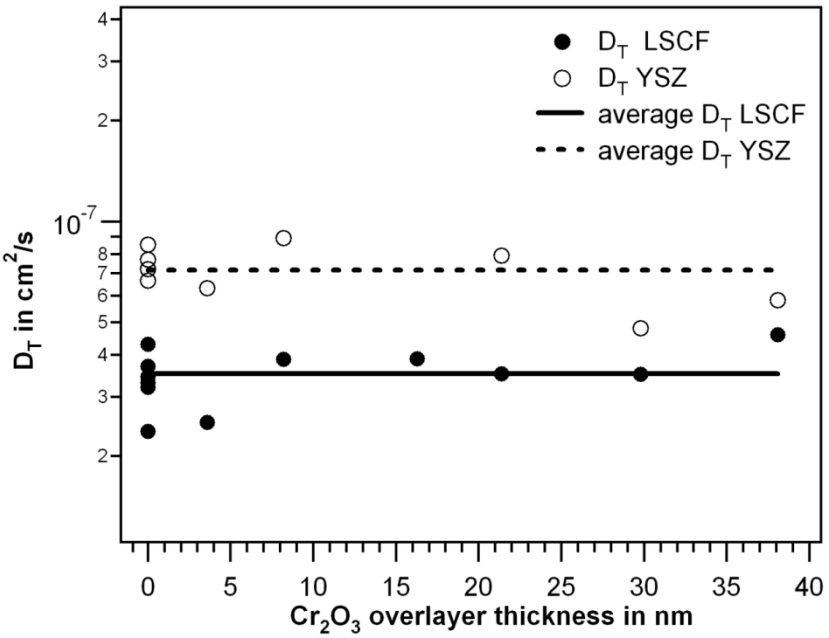

Figure 16: D_T values for LSCF (filled circles) and YSZ (open circles) as function of Cr_2O_3 overlayer thickness.

When a Cr_2O_3 film is present on the surface of the substrate, the model is more complicated since we have two interfaces. First the gas-solid interface at the surface of the sample (gas-Cr_2O_3), second the interface between the film and the substrate (Cr_2O_3-LSCF or Cr_2O_3-YSZ).

For the Cr_2O_3 covered sides the oxygen molecule must first diffuse through the Cr_2O_3 before entering the substrate. If we use equation (1) for fitting the profile – the extracted parameter k represents an effective surface exchange coefficient which depends on the following parameters: $k_{Cr_2O_3}$ the surface exchange coefficient for Cr_2O_3, $D_{O\_Cr_2O_3}$ the diffusion coefficient of oxygen in Cr_2O_3 and $k_{Cr_2O_3/substrate}$ the transfer of oxygen through the Cr_2O_3 / substrate interface. With the additional complication of surface roughness and Cr_2O_3 thickness variations, possible diffusion of Cr into or secondary phase formation with the substrate, attempting to derive a complete equation for the surface exchange coefficient utilizing these parameters might be generally useful but not feasible for our study since some of these parameters are very sample specific and difficult to measure. Furthermore, the goal of this study is to get a first impression of the impact of Cr_2O_3 on the oxygen uptake. Instead, since the thickness of the Cr_2O_3 overlayer is very small compared to the total diffusion length (e.g. 30 nm film thickness compared to ~300 µm total diffusion length in YSZ) an effective surface exchange coefficient is used k_{eff}. Using this approach, one might consider 3 possible regimes where 3 different rate determining steps govern the behavior of k_{eff} as we increase the Cr_2O_3 overlayer thickness. First a regime where k_{eff} is mainly determined by the change in electronic structure at the surface due to the increase in Cr_2O_3 overlayer thickness, second (once a stable electronic structure of the surface is established) a regime where k_{eff} is now mainly controlled by the flux of oxygen through the Cr_2O_3/substrate interface and for very thick films a third regime where k_{eff} is controlled by the diffusion of oxygen through the Cr_2O_3 (this regime would violate our assumption that the film thickness is small compared to the diffusion length and therefore is inaccessible with our experiment). In Figure 16 the extracted D_T values are plotted versus Cr_2O_3 layer thickness for each side of the samples for LSCF and YSZ. The bare sides of the Cr coated samples are represented by the multiple data points at x=0. The values for the Cr_2O_3 covered sides are plotted with increasing Cr_2O_3-film thickness. As expected, the diffusion coefficient, D_T, is identical for both the clean and Cr_2O_3 covered side, as highlighted by the average D_T value (solid line for LSCF, dashed line for YSZ). This is strong evidence that our k_{eff} assumption holds.

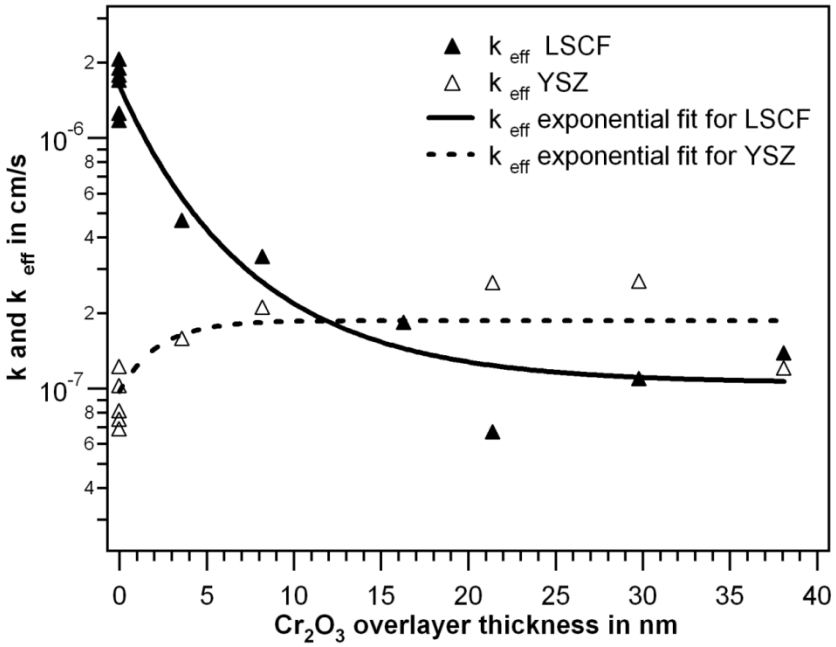

Figure 17: k and k_{eff} values for LSCF (filled triangles) and YSZ (open triangles) as function of Cr_2O_3 overlayer thickness.

The effective surface exchange coefficients for Cr_2O_3 covered LSCF and YSZ are plotted in Figure 17, also as a function of increasing Cr_2O_3-film thickness. (again, the direct surface exchange coefficients for clean LSCF and YSZ are plotted as zero Cr_2O_3 coverage.) The most striking feature for Cr_2O_3 coated LSCF is the rapid decrease of the effective surface exchange coefficient, k_{eff}, by over one order of magnitude. Exponential fits with respect to thickness (since the true mechanisms are unknown, as first approximation a single process with a governing energy barrier is used) indicate that k_{eff} for Cr_2O_3 coated LSCF (solid line) approaches an asymptotic value that is lower than the asymptotic value of the YSZ fit (dashed line). This also highlights the most striking feature of the YSZ data - an increasing k_{eff} for increasing Cr_2O_3-film thickness, which eventually exceeds the LSCF values.

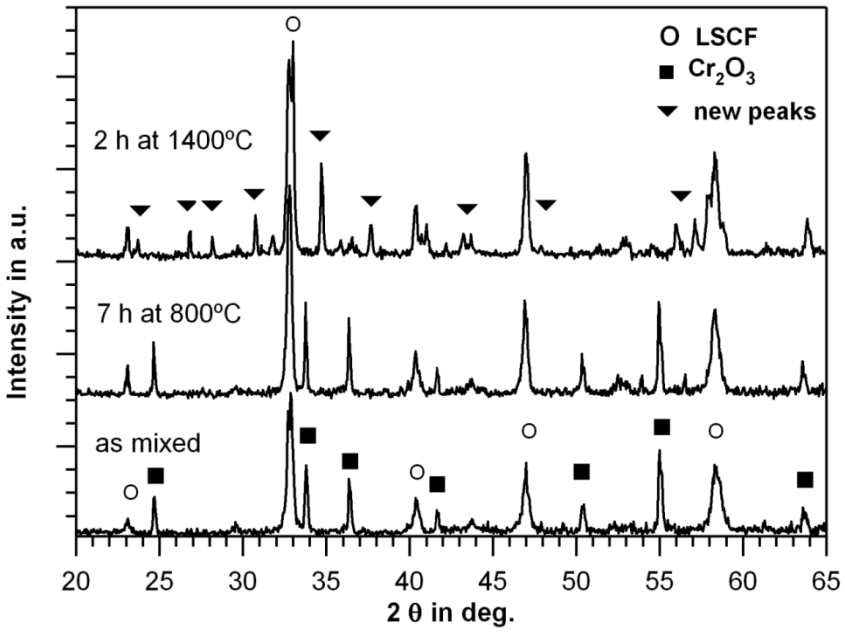

Figure 18: XRD spectra of the LSCF - Cr_2O_3 1:1 mixture before (lower spectrum), after 7 hours annealing at 800° in air (middle spectrum), and after 2 hours annealing at 1400°C in air (upper spectrum).

Cause of inhibited oxygen uptake - To understand the cause of inhibited oxygen uptake, it is first of all necessary to distinguish between rate limitation due to the concentration of electronic species available at the surface, as suggested by Lane and Kilner [43] for the GDC system and by various other authors for the mixed conducting perovskites like doped $SrTiO_3$ and LSF/LSC [47-49], and secondary phase formation at the interface of film and substrate as commonly found in the YSZ/LSCF system [29]. To check for the formation of secondary phases, a mixture of Cr_2O_3/LSCF and Cr_2O_3/YSZ was prepared (see Experimental) and sintered at 800°C for 7 hours in air, an annealing time twice the actual annealing time of the tracer diffusion studies to account for the modest detection limit of XRD. To check for possible long-term secondary phase formation, samples were also sintered at 1400°C for 2 hours. In Figure 18 the XRD spectra are shown for the 1:1 mixture of LSCF and Cr_2O_3 as prepared (lower spectrum), the mixture after 7 hours at 800°C (middle), and after 2 hours at 1400°C (upper spectrum). The LSCF peaks (circles) and Cr_2O_3 peaks (squares) identified in the "as mixed" spectrum are also observed in the "7 hrs at 800°C" annealed spectrum. No additional peaks were observed for annealing at 800°C, indicating that no secondary phase formed after 7 hours. However, for the "2 hrs at 1400°C" anneal spectrum the chromia related peaks are completely absent and new peaks can be observed (triangles), indicating that a secondary phase formation occurred. In contrast, the XRD spectrum for a mixture of YSZ and Cr_2O_3 (not shown) showed no additional peaks even after sintering for 2 hours at 1400°C. Thus, secondary phase formation can be eliminated as a contributing factor to the extracted ^{18}O diffusion.

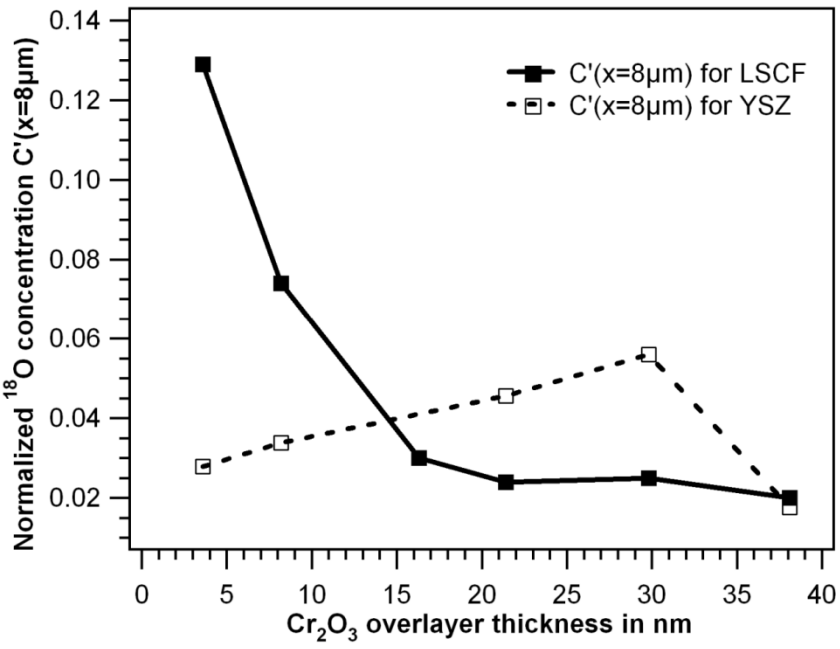

Figure 19: Near surface concentration of ^{18}O (x=8 µm,) for LSCF (filled squares) and YSZ (open squares).

Rate limitations - Differentiating between rate limitations due to oxygen adsorption at the surface or to the electronic properties of the Cr_2O_3 overlayer is rather difficult as shown for mixed-conductors by Adler et al. [49]. It is also discussed by Lane and Kilner [43] for wide band gap materials like GDC, using the same band gap arguments as Adler et al. In our case LSCF at 800°C is a mixed conductor with an electronic conductivity of about $\sigma =$ $\cdot$ [26]. Cr_2O_3, is considered a semiconductor at high temperatures (E_g= 3.3 eV at 1300°C [50]) with a conductivity of $\sigma =$ $\cdot$ at 800°C [51]. Considering these differences in the electronic properties (almost semimetal vs. band gap) and the small crystal size (on the order of film thickness) and thus the large amount of grain boundaries which are mostly perpendicular to the surface, the decrease in the surface exchange coefficient for LSCF covered with Cr_2O_3 is most likely due to the reduction in available electronic species rather than limitations in the adsorption, which is usually related to the number of active sites on the surface [49]. This is especially interesting since Cr_2O_3 is still an electronic conductor, allowing electrons from the LSCF to aid in the reduction of oxygen at the surface even after the electronic structure of the film has completely formed. As Cr_2O_3 overlayer thickness increases further these contributions become smaller and smaller leading to a slower decrease in k_{eff} for LSCF than increase for YSZ as observed in Figure 17.

In contrast, since YSZ is a poor electronic conductor with a very high band gap (E_g=4.23 eV for 9.5% Y at room temperature [52] and $\sigma \approx$ $\cdot$ for polycrystalline YSZ at 800°C [53]), this assumption predicts that for our nanocrystalline Cr_2O_3 on YSZ there would be an increase in the surface exchange coefficient with increasing Cr_2O_3 overlayer thickness. This increase would continue until the electronic structure of the Cr_2O_3 is established completely. In Figure 17, the k_{eff} value increases with increasing Cr_2O_3 thickness and reaches a constant value of approximately 2 times its clean surface value for thicknesses above 12 nm .

Interestingly, the asymptotic value for k_{eff} value for Cr_2O_3 on YSZ is even higher than that for Cr_2O_3 LSCF. This is confirmed in the measured ^{18}O concentration near the surface for the two. In Figure 19 is plotted the normalized concentration of ^{18}O vs. Cr_2O_3-film thickness for the cross section measurement nearest the surface (at x=8 μm). It clearly shows that the concentration of ^{18}O in YSZ with a Cr_2O_3 overlayer thicknesses above 12 nm is larger than for LSCF with the same Cr_2O_3-film thickness. This is strong evidence that at these thicknesses the diffusion through the Cr_2O_3/substrate interface $k_{Cr_2O_3/substrate}$ is the governing mechanism. A possible explanation for the lower k_{eff} values for LSCF might be the existence of a very thin layer of a secondary phase right at the interface of the Cr_2O_3 grains and the LSCF substrate. This very thin layer is not detectable with the experimental methods employed in our study and thus cannot be excluded. Furthermore no secondary phases are likely to form at an YSZ/ Cr_2O_3 interface leaving the k_{eff} values for YSZ unaffected. Other possible explanations could include the difference in activation energy for vacancy hopping, since LSCF has a much higher activation energy compared to YSZ (resulting in the difference in their D values in Fig. 3). However, since the surface electronic structure of the Cr_2O_3 film is well established at these overlayer thicknesses, the total oxygen uptake by, and subsequent diffusion into, the substrate would be controlled by the Cr_2O_3/substrate interface in any case.

These results provide a possible explanation of the different degradation behaviors of LSCF vs. LSM cathodes observed by others [54-56]. Jiang et al. [17] concluded that for LSCF/GDC cells, Cr_2O_3 preferentially deposits on the cathode. Based on this work, this preferential deposition would rapidly decrease the cathode's electro-catalytic activity. However, in LSM/YSZ cells, Jiang found that Cr_2O_3 preferentially deposits on the electrolyte, which based on our results leads to a slight increase of the oxygen uptake directly into the YSZ and only a gradual degradation is observed for low current densities [54]. For further understanding of the degradation processes taking place in an operating fuel cell the conditions at the air side would have to be mimicked better as gaseous chromium is deposited and, as pointed out earlier, might have additional effects on the oxygen uptake related to the deposition mechanism (e.g. electrochemical reaction competing with the oxygen reduction vs. nucleation [17]).

3.1.5. Conclusions

The analysis of the experimental results and the different conclusions that can be drawn for the Cr_2O_3/LSCF and Cr_2O_3/YSZ system show the complexity of this single SOFC degradation mechanism. The close proximity of different materials in the cell and stack environment leads to unique and sometimes unwanted interactions between them. Advantageous properties of one material, like the formation of a corrosion resistant Cr_2O_3 layers on stainless steel, can lead to detrimental secondary reactions with other cell components. To accurately predict and measure all interactions possible in this multi material environment is tedious and time consuming. Rapid commercialization of SOFC technology can only be achieved if these problems are overcome. Thus, identifying interactions between chosen material pairs and development of mitigation strategies are the only way to guarantee fast implementation of this promising technology into the everyday power generation systems. This study in the large field of degradation studies measured the Cr_2O_3 layer thickness dependence of the effective surface exchange coefficient k_{eff}. It was then possible to identify a critical thickness of ~ 12 nm where the oxygen uptake of LSCF was reduced by an order of magnitude, to a value similar to the one of YSZ. This detrimental effect, however, was not observed in YSZ itself, which showed a slight increase in oxygen uptake for this film thickness. From this part of the experiment it was possible to prove the theoretical prediction in the literature (Lane and Kilner [43]), that the observed changes are due to changes in the surface electronic structure. In the second part of the experiment, another possible factor, the formation of secondary phases, was ruled out. It was shown to not occur at temperatures and annealing times used in this experiment. This ruling out aspect of the experiment is especially important considering the many interactions possible and can be used in future studies to narrow down the degradation possibilities for these material combinations. Some conclusions can also be drawn for degradation of actual cells, as shown in the last part of the discussion section, demonstrating the high applicability to cell engineering. It also gives valuable information for the studies presented next (Chapter 4), as the sensitivity of the catalytic activity of LSCF is shown. Small contaminant concentrations on the surface can drastically reduce the effectiveness of LSCF with respect to oxygen reduction and incorporation, reducing the advantages of this material over others (e.g. $La_{0.4}Sr_{0.6}MnO_3$ - LSM). Similar effects are the focus of the next part – this time concerning the "internal" structural degradation of the cathode material LSCF under operating conditions.

Chapter 4

4. Cathode Decomposition Due to Changes in the Oxygen Vacancy Concentration

In this chapter, the structural decomposition of the LSCF cathode and subsequent SrO formation at the surface is investigated. A new way of measuring this Sr segregation via Cr tracers is presented, its dependence on the applied bias potential extracted and possible explanations for the found results are given, demonstrating the new scientific insight gained. The experimental setup, results and discussions sections are quoted from [57].

4.1. Electrochemically Driven Cation Segregation in the Mixed Conductor $La_{0.6}Sr_{0.4}Co_{0.2}Fe_{0.8}O_{3-\delta}$

4.1.1. Introduction

After determining extrinsic degradation mechanisms, induced by other cell components, the intrinsic degradation of the electrode material, which is also a contributing factor to cell degradation, is investigated. As mentioned in Chapter 2.4.2, the Sr doping of the $La_{0.6}Sr_{0.4}Co_{0.2}Fe_{0.8}O_{3-\delta}$ (LSCF) electrode gives rise to good ionic and electronic conductivity which is crucial in extending the TPB. Since this is the origin of the better cell performance of LSCF vs. poor ion conducting electrodes like LSM, maintaining good ionic conductivity is crucial. Unfortunately, material degradation under operational conditions like ion currents, varying oxygen partial pressures and high temperature is poorly understood. Therefore, structural degradation remains a barrier to broad implementation of solid oxide electrolyzer cells[58] (oxygen production), separation membranes[59] (oxygen separation) and as electrodes in solid oxide fuel cells (SOFCs)[60]. Additionally, oxygen vacancies are responsible for other properties exhibited by perovskites, e.g. magnetism[61], two-dimensional electron channels in otherwise insulating materials[61] and thus investigating this material is of broad interest to the scientific community.

The mixed ionic/electronic conductivity of the LSCF electrode in the energy related applications stems from its high oxygen vacancy tolerance at operating temperatures[34] and the polaron hopping induced by the acceptor dopant Sr. In SOFC stack tests, long-term performance degradation due to Sr segregation was observed[62] and related to compromised oxygen dissociation at the surface[32]. In the literature, some authors found evidence that the driving factor for Sr segregation might be variations in the oxygen vacancy concentration[63].

In order to develop effective mitigation strategies, the underlying mechanism has to be identified. As an example, *anodes* exposed to fuel stream contaminants such as sulfur and residual hydrocarbons showed high structural degradation as well, which was mitigated

by material property tailoring [64, 65]. To achieve the same for MIEC *cathodes* requires finding powerful techniques to identify and investigate their degradation mechanisms.
In the following sections, the Sr segregation in perovskite electrodes is investigated by means of a new technique - measuring secondary phase formation with gaseous Cr via X-ray Absorption Spectroscopy (XAS). From the previous experiment the interaction of Cr with the LSCF and YSZ components of a cell was investigated separately in a "controlled" fashion. Now, this interaction of Cr containing part in the experimental setup with the other cell components under operating conditions is used to differentiate between surface-segregated and bulk Sr. The favorable[33] acid-base reaction of Sr with hexavalent chromium (Cr^{6+}) gives our experiment this selectivity since Cr deposits in the reduced form of Cr_2O_3 (Cr^{3+}) when segregated Sr is absent.
However, care has to be taken to exclude possible enhancement or mitigation effects gaseous Cr could have on Sr segregation itself. As mentioned earlier, literature provides two competing theories for the nature of Cr deposition (see Chapter 2 and Chapter 3). As different as both cases are one thing remains the same, Cr is not seen as the origin of the Sr segregation or enhances/ mitigates it. Both cases view $SrCrO_4$ formation as a secondary solid-state reaction of existing SrO with Cr. The *ex-situ* measured $SrCrO_4$/ Cr_2O_3 ratio is therefore indicative of the relative Sr segregation and allows exploration of the impact the electrochemical environment has on this degradation mechanism. Since gaseous Cr can be introduced in many other systems as well, this experiment is broadly applicable to MIECs related research, again showing the multitude of possibilities to investigate this interesting class of materials.

4.1.2. Experimental

We first performed four-probe conductivity measurements of symmetric-half-cells[17, 58] consisting of a $Gd_{0.1}Ce_{0.9}O_{2-\delta}$ (GDC) electrolyte with $La_{0.6}Sr_{0.4}Co_{0.2}Fe_{0.8}O_{3-\delta}$ (LSCF) porous electrodes on *both* sides. The symmetrical nature of the samples allowed for the simultaneous study of how cathodic and anodic overpotentials affect Sr segregation dynamics. GDC powder was uniaxially pressed in 1/2 inch diameter disks with thicknesses of 1-3 mm. A thin LSCF paint was applied to both sides and co-sintered at 1200 ˚C for 10 hours in air. The LSCF electrode thicknesses were measured by cross section FE-SEM and ranged from 40 to 50 μm with uniform porosity. Silver mesh contacts were pressed on each side of the sample with Inconel™ disks and held together with alumina fasteners. The Inconel™ discs are perforated to allow ambient air access and they also serve as the gaseous Cr source due to Cr outgassing of this material at elevated temperature.

The sample current was measured for 48 hours with an applied constant DC voltage (potentiostatic method) with the sample and holder in a quartz tube furnace at 800˚C in air. Various GDC thicknesses were run with bias voltages from 0.1 to 0.6 V allowing us to independently assess the effects of ion current and bias potentials. One sample was disconnected from the power source one hour prior to cool down to verify that our results are independent of the presence of a bias voltage during the cooling process. After cooling at a rate of 4˚C/min to room temperature, the samples were stored in a dessicator and subsequently the Cr L_{23}-edge XAS was measured in total electron yield mode (TEY) at beamlines 4.0.2 and 6.3.1 of the Advanced Light Source of the Lawrence Berkeley National Laboratories. Reference L_{23}-edge XAS spectra for Cr^{3+} and Cr^{6+} from powders consisting of Cr_2O_3 (99% purity) for the trivalent chromium, CrO_3 (99.99% purity) and $SrCrO_4$ (99.9% purity) for the hexavalent chromium were also measured. The Sr M_{45}-

edge XAS spectra for all samples (not shown) are nearly identical and, could not be used to distinguish Sr in the $SrCrO_4$ from Sr in LSCF.

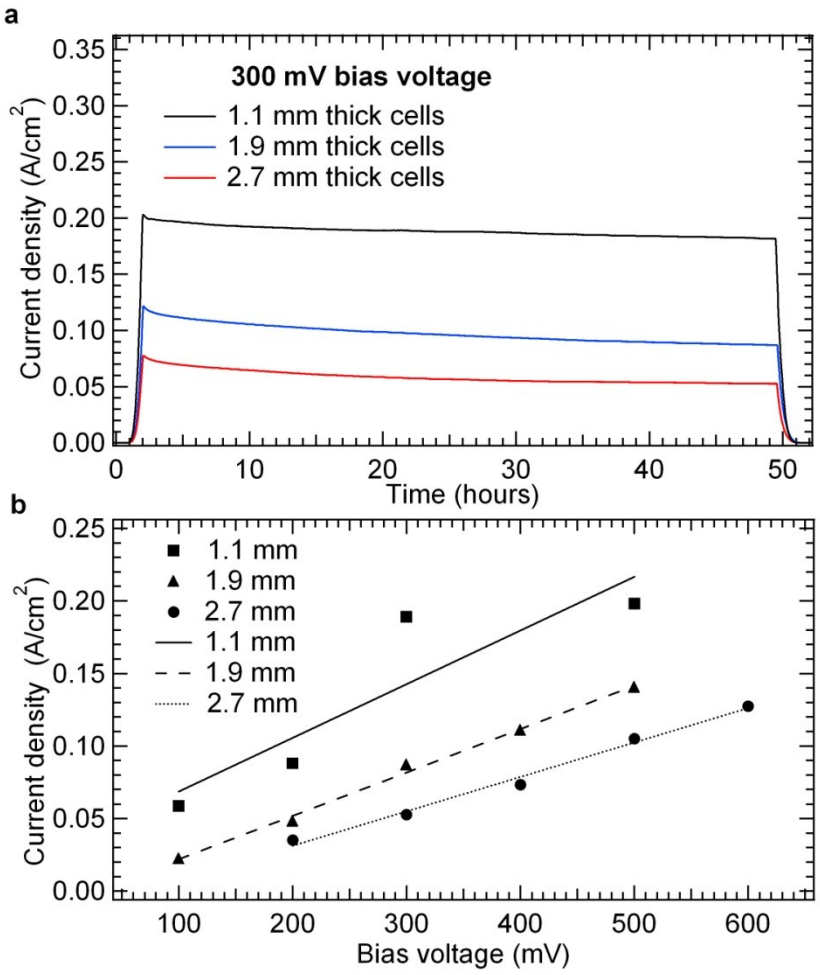

Figure 20: a) Ion current density versus time plots for three GDC thicknesses with an applied bias voltage of 300 mV. b) Ion current as a function of bias potential for all three GDC thicknesses. Each data point represents an individual sample's current density after 48 hours of operation.

4.1.3. Results

Since the electrolyte is an electrical insulator, the measured current is due to the oxygen ion flow across the GDC electrolyte, originating from oxygen molecule dissociation at the negative LSCF contact (cathode) and terminating in molecular recombination at the positive LSCF contact (anode). The ion current of each sample (with a specific bias potential and GDC thickness) was recorded over a 48 hour period and the results from representative samples are shown in Figure 20a. After the heating transient from zero current to maximum current, a sharp but brief initial degradation was observed for all samples, followed by slower long-term degradation. Figure 20b shows a plot of the current density after 48 hours as a function of bias potential for each GDC electrolyte thickness and reveals a linear behavior of the ion current with potential, indicating that the heterostructures are in a regime where the total resistance to the ion flux is dominated by the GDC electrolyte. A plot of total resistance vs. sample thickness (not shown here) also displayed a strictly linear (ohmic) behavior.

The total voltage drop across the cell can be modeled with the following equation[66]: $V = \eta_s^a - \eta_s^c - \frac{RT}{2F} ln\left(\frac{c^a_{V,int}}{c^c_{V,int}}\right) + IR_e$ which includes the surface overpotentials for the cathode $\eta_s{}^c$ and anode $\eta_s{}^a$, the concentration of oxygen vacancies at the corresponding LSCF/GDC interfaces $c^a{}_{V,int}$ and $c^c{}_{V,int}$, the gas constant R, the temperature T, the Faraday constant F, and the ohmic loss in the electrolyte IR_e. For our setup it is impossible to separately measure the overpotentials of cathode and anode, but from the strict ohmic behavior of our samples, even far beyond the potentials used in this study, we conclude that the overpotentials are small and the overpotential-current relation is linear for the bias potentials used. Thus, we mainly concentrate on the difference between anode and cathode side and the qualitative behavior with increasing overpotentials using the bias voltage as a convenient control parameter. (If the overpotentials were the main factor governing the I-V behavior we would expect a Tafel-like behavior, where the current goes up exponentially with voltage[66]).

To quantify the Sr surface segregation, we measured the Cr L_{23}-edge XAS of both sides of each heterostructure. In Figure 21a, the reference spectra for hexavalent chromium ($SrCrO_4$, black line) and trivalent chromium (Cr_2O_3, red line) and a mixture of both powders (green line) are displayed. XAS spectra for the less stable CrO_3 did not resemble any of the spectra. After energy referencing the main Cr_2O_3 peak to 575.20 eV, the spectra were normalized to the integrated L_3 peak area and subsequently normalized to the number of d-holes; 7 for Cr_2O_3 in [Ar] $3d^3$configuration and 10 for $SrCrO_4$ in [Ar] $3d^0$ configuration[67]. The mixed powder spectra can be accurately reproduced with a least-squares-fit linear sum of the two reference spectra (blue line), allowing for a quantitative determination of the relative concentrations of Cr^{6+} and Cr^{3+}. (The absolute value of either species at the surface is very difficult to obtain.)

Representative spectra of the cathode and anode side of the 1.9 mm thick GDC structure with 100 mV bias voltage and their associated fits are shown in Figure 21b. The only free parameter for fitting the Cr spectra is the ratio of the d-hole normalized Cr^{3+} and Cr^{6+} reference spectra contributions. This ratio can be used to determine the variation in the $SrCrO_4$ concentration as a function of bias voltage and is shown in Figure 21c for each side of 1.1, 1.9 and 2.7 mm thick samples. The open symbols represent the oxygen dissociation side (cathode) and the solid symbols the oxygen recombination side (anode).

The anode side unambiguously displays an increase in $SrCrO_4$ to Cr_2O_3 ratio with increasing bias potential. This trend is not observed on the cathode side where a high and nearly constant ratio is observed. This discrepancy is a clear demonstration of the

electrochemical environment affecting the composition of the Cr precipitates (our indicator of Sr segregation). Changing the contact material from silver to gold, or eliminating the bias potential before cool-down results in no change in the Cr^{3+} to Cr^{6+} ratio.

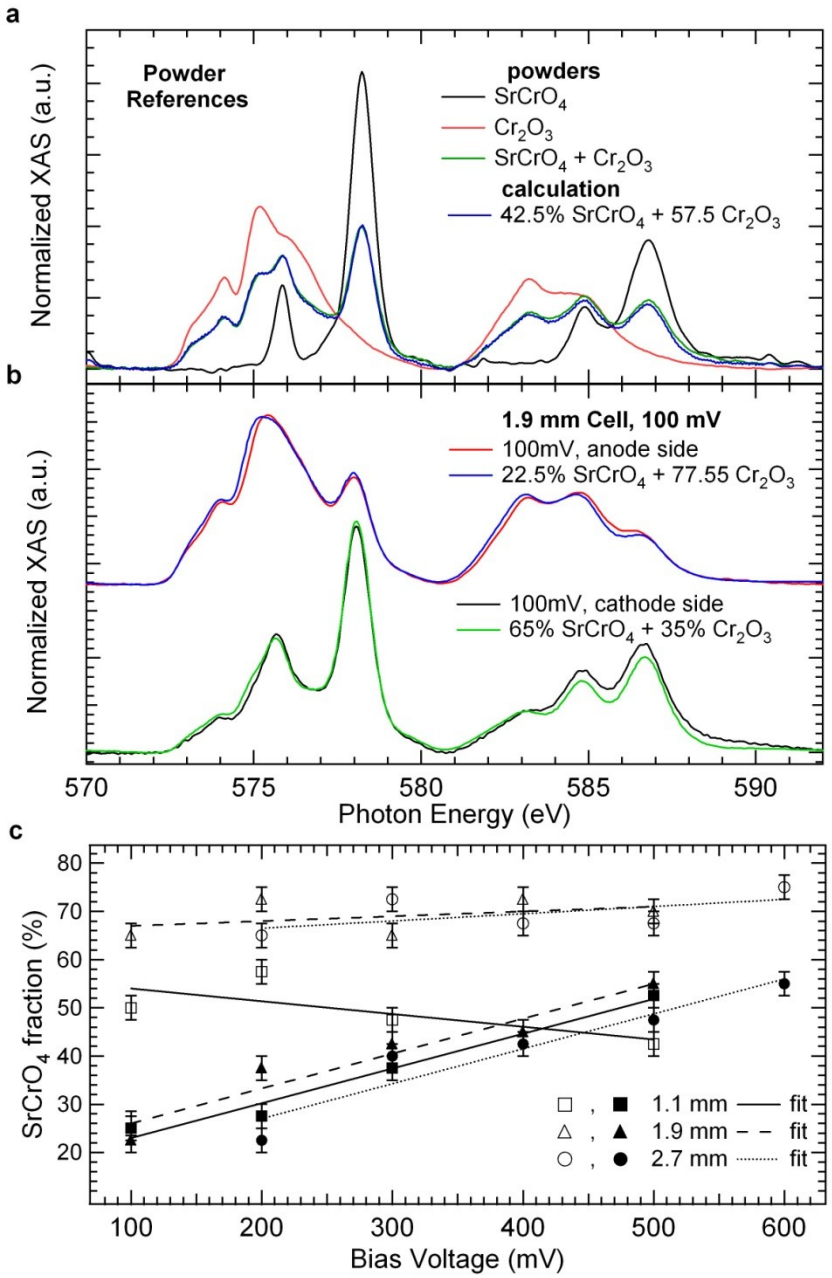

Figure 21: a) The L_{23}-edge XAS reference powder spectra for Cr^{3+} and Cr^{6+}, with a measured spectrum for a mixed powder and the best fit. b) Cr L_{23}-edge XAS spectra and fits for both sides of a representative sample at an applied potential of 100 mV. c) Cr composition as a function of bias voltage for both sides of all samples with open markers for the oxygen dissociation side (cathode), and solid markers for the oxygen recombination side (anode).

4.1.4. Discussion

The mechanism of Sr segregation and its variability with bias voltage can now be understood in the context of oxygen vacancy concentrations in the cathode and anode. Initially, without applied bias potential (I=0), the Sr dopant is charge compensated by oxygen vacancies (leading to good ionic conductivity)[34]. At the cathode, the oxygen partial pressure right above the surface of the sample decreases and the concentration of oxygen vacancies increases with applied bias potential[25, 66]. These additional oxygen vacancies can be compensated by the existing Co^{4+}, reverting to Co^{3+} (or even Co^{2+})[34]. On the other hand, if we assume Gibbs-Duhem behavior of our system, the chemical potential of the cations would increase with decreasing anion chemical potential and the oxygen vacancies could also be compensated by A-site (cation) vacancies. It was shown previously that Sr has the highest diffusivity in LSCF[62], which together with the results presented here clearly demonstrates that mainly Sr is affected by this change in chemical potential. This ultimately leads to the observed Sr segregation and makes it a significant contribution to the compensation mechanism. (Alternatively, a similar argument could be made with an electrochemical instead of just a chemical potential where we assume that the Sr ions diffuse to form a double layer, neutralizing this electrochemical potential) However, since the change in overpotential is expected to be small, the change of Sr segregation with increased bias potential or thickness of the electrolyte is expected to be small, especially since the reduction of the Co^{3+} to Co^{2+} can act as an additional compensation mechanism. Thus, a nearly constant $SrCrO_4$ to Cr_2O_3 ratio as a function of bias potential is observed as seen Figure 21c for the cathode sides of the samples (open markers).

On the anode side, the oxygen partial pressure over the surface is increased and the oxygen vacancy concentration in the LSCF is reduced, driving the oxygen association reaction[66]. For low bias potentials the decrease in vacancy concentration is mostly compensated by oxidation of Co^{3+} to Co^{4+} effectively reducing the Sr segregation and thus the $SrCrO_4$ to Cr_2O_3 ratio, as is observed in Figure 21c (solid markers). This is plausible, since the chemical potential for cations is reduced with increasing anion chemical potential. At higher anodic bias potentials, since there is no 5+ oxidation state for Co, the formation of A-site vacancies now compensates further reduction of the oxygen vacancy concentration, resulting again in Sr segregation as demonstrated by the results presented here. This leads to a variable $SrCrO_4$ to Cr_2O_3 ratio at the anode, which increases with bias potential, as observed in Figure 21c (solid markers).

As the GDC thickness is changed, the overpotentials at the cathode and anode are expected to change as well[66] (for a given total potential difference, larger GDC thickness translates to a higher voltage drop across the GDC and lower overpotentials at the electrodes). As previously discussed, as the bias potential is increased the $SrCrO_4$ to Cr_2O_3 ratio at the cathode remains mostly unaffected, but the Sr segregation at the anode is observed to increase. This leads to a crossing point when Sr segregation ($SrCrO_4$ to Cr_2O_3 ratio) is plotted as a function of bias potential for the anode and cathode sides (Figure 21c). As the sample thickness is increased, the relative contribution of the ohmic term to the voltage drop also increases. Since the cross-over point should occur at roughly the same overpotentials, larger bias potentials are required to reach this crossing point in thicker samples. This is also observed in Figure 21: the crossing point is at 410 mV for 1.1 mm GDC and (extrapolated) 760 mV and 890 mV for 1.9 and 2.7 mm GDC.

For future experiments, a comparison of Sr segregation in samples exposed to various oxygen partial pressures but without applied bias potential with the data presented here would be logical. Exposing the cathode/anode side to a mixture of e.g. N_2 and O_2 with a

P_{O2} comparable to the one expected on the cathode/anode side under bias could yield further insight into the Sr segregation mechanism.

4.1.5. Conclusion

In conclusion, the feasibility of the new technique using the XAS signature of a tracer element in studying Sr segregation in porous LSCF electrodes was clearly demonstrated. The relative concentration of Cr^{6+} in $SrCrO_4$ and Cr^{3+} in Cr_2O_3 can be used to identify the amount of Sr, segregated in symmetric model SOFCs. Hereby, the difference in the anode and cathode sides results and the dependence on bias potential and electrolyte thickness were used to deduce the driving factor for Sr segregation. As shown in the previous experiment (Chapter 3) eliminating other possible influences on the results is crucial. By keeping all other experimental parameters the same, the oxygen vacancy concentration variations (cathode vs. anode and when changing the applied bias potential) were found to be the origin of Sr segregation. This measured dependency on polarization and magnitude of the applied bias potential, governing the electrochemical environment, lead to the identification of two different compensation mechanisms that both lead to Sr segregation.
Viewed under the main goal of these types of experiments, the development of degradation mitigation strategies, this understanding of the Sr out-diffusion mechanism can help tremendously. Previously, Baumann et al.[62] showed that changing operating conditions e.g. short, reverse-bias DC pulses can lead to performance recovery after degradation occurred. As mentioned in the anode side case, material property tailoring can help to delay or even mitigate degradation on the cathode side as well. Including the knowledge of the underlying Sr segregation mechanism into the manufacturing process, it should be possible to stabilize the Sr ions within the LSCF. Since vacancy concentration changes are the cause, increasing other compensation mechanisms, for example the oxidation/reduction of Co, should mitigate Sr segregation. This could easily be achieved by increasing the Co content in the bulk material or perhaps only in the near surface region. Introducing a more effective compensation by doping a multi-valent transition metal into the B-site could also mitigate degradation. The transition metals Mo (additional 5+ oxidation state) or Mn (+6 oxidation state) are likely candidates and experiments involving them are currently in progress in our group.
The theory for these ideas is already worked out and available in the literature (e.g. Tsur et al.[68], showing the acceptor doping being fully compensated by native negative ionic defects like Sr) which is not too surprising, since it shows again how broadly applicable the results gained in this kind of studies are. The hereby gained insight was also applied in the experiments shown in the next part of this thesis. Studying the surface degradation of LSCF indirectly by means of a tracer gave inspiration to use XAS signatures of other elements in the film to, in combination with other techniques, further investigate this structural degradation phenomenon. Again, the complexity of the SOFC system with multiple materials in intimate contact and the impact of the operation conditions on the structure and performance can only be studied by using multiple techniques and tedious separation of each individual mechanism.

Chapter 5

5. Mapping of Cation Oxidation States in Dense $La_{0.6}Sr_{0.4}Co_{0.2}Fe_{0.8}O_{3-\delta}$ Cathodes

In this chapter the current and ongoing research is presented regarding the oxidation states of the B-site cations in LSCF, measured with the new fast-scan capability of beamline 6.3.1 and the mapping of these states across the sample surface. This distribution can yield valuable information about the electro-catalytically active regions on the sample and the oxygen vacancy distribution. It can also be used, in a similar fashion to the Cr tracer in the previous chapter, to determine structural information about the degradation of the LSCF film which is mainly due to Sr segregation.

5.1. Sample Preparation

In order to measure the distribution of cationic oxidation states via XAS, the samples have to be prepared carefully to obtain meaningful results. First, the thickness of the LSCF cathode has to match the penetration depth of XAS to ensure that we measure the whole cathode and not just a surface effect. Second, we want to suppress secondary phase formation at the cathode/electrolyte interface. Since the penetration depth of XAS is in the region of tens of nm, we have to make samples with cathodes/anodes of approximately that thickness, which can pose a problem due to the roughness of the electrolyte, resulting in a non-continuous film. To avoid this problem, we used 10x10x0.5 mm slabs of single crystal 8mol-YSZ (100) from MTI Corporation as electrolyte substrates. Polished on both sides to < 5 Å surface roughness (via AFM) they provided flat enough surfaces for electrodes with a thickness of 10 nm. Since we want to use LSCF as electrode material, which reacts with YSZ forming La and Sr zirconates at the interface, we have to use a GDC interlayer to prevent secondary phase formation. To obtain electrodes with a thickness of about 10 nm and the target composition of $La_{0.6}Sr_{0.4}Co_{0.2}Fe_{0.8}O_{3-\delta}$, pulsed laser deposition (PLD) in an oxygen environment was used, in cooperation with Prof. Shane Stadler, Louisiana State University. Laser targets of $La_{0.6}Sr_{0.4}Co_{0.2}Fe_{0.8}O_{3-\delta}$ and $Gd_{0.1}Ce_{0.9}O_2$ were made from commercially available powders (GDC 10M and LSCF-P, Fuel Cell Materials Inc.) having the appropriate compositions. They were uniaxially pressed with 5000 lbs into pellets and sintered for 10h at 1200˚C in air, forming the dense disks needed as targets. The PLD system has a Lambda Physik Compex 201 KrF excimer laser with a wavelength of $\lambda = 248$ nm. The fluence was set to approximately 2.5 J/cm^2 with a pulse repetition rate of 10 Hz. The base pressure of the chamber was less than 2×10^{-8} Torr before the introduction of O_2 into the growth chamber. For the film growth, the YSZ single crystal substrates were heated to 650˚C and an oxygen partial pressure of 200 mTorr was maintained. The substrate to target distance was 5 cm and the deposition rates were 0.2 and 0.3 Å/s for LSCF and GDC, respectively.

After reaching the desired film thicknesses, the samples were slowly cooled down to room temperature in a 25 Torr oxygen environment.
Since the samples had to be symmetric, contamination of the sample during the growth on the reverse side had to be avoided. To maintain proper heat conduction between sample heater and sample, the samples are usually glued to it using silver paint. Since this was not an option for these samples, at first a gold sleeve, glued to the sample heater, was used to hold the samples in place. Due to deformation at high temperature and mechanical stress from removing / flipping the samples, the gold sleeve showed deformations which might have had a negative impact on the thermal contact. Thus, the sleeve was replaced by a piece of Si wafer that was glued to the heater stage and a support frame was constructed, pressing the sample to the Si piece. This method was much more reproducible and provided extremely even, good thermal contact between the sample and the heater. This might explain some of the sample-to-sample discrepancies later (e.g. chapter 5.4.2) since differences in thermal contact might lead to slightly different substrate temperatures and thus slightly thinner or thicker films. In general, two different film structures were grown on the YSZ single crystal substrates. First, only 10 nm of LSCF were deposited on both sides of an YSZ single crystal sample and second, 20 nm GDC were deposited first, then a 10 nm LSCF film was deposited on top of it. In the following sections these sets will be labeled w/ and w/o GDC interlayer for clarity. These two different structures were chosen in order to test the influence of the GDC interlayer on the cell performance and structural degradation, possibly linking them to a specific degradation mechanism.

5.2. Experimental Setup

In order to investigate the impact of the electrochemical environment on the distribution of the cation oxidation states, a high temperature setup was build where the samples were subjected to various current and voltages in air, at temperatures comparable to the operating temperatures of SOFC stacks. Current degradation measurements were performed for up to 100 hours at 800˚C using the potentiostatic method with a bias voltage of 500 mV. To bring the sample to the target temperature, a Lindberg-Blue tube furnace (Type M) was used, containing a quartz tube with the sample holder setup as shown in Figure 22a. The furnace was controlled by a UP150 controller with a thermocouple in contact with the outside of the quartz tube, right underneath the sample holder, ensuring that the samples are indeed at target temperature. The sample holder (in contrast to the one used in Chapter 4) was machined from 6.5 mm thick, pure alumina plates (96% purity, Ortech Inc.) into disks of 25 mm diameter using water jet cutting (Hogin machine Inc.). Various holes were made the same way to hold the assembly screws, wire tubes and allow air exchange of the sample with the surrounding atmosphere, as shown in Figure 22b. Alumina tubes (99.5% purity, Ortec Inc.) were used to protect the pure gold wires (Alpha Aesar, 99.99% pure, 0.5 mm diameter) from sticking to the quartz tube or each other, by attaching them with ceramic glue (1650˚C high purity alumina adhesive, MTI Corp.) to the sample holder plates. At one side of the sample holder, only one air hole was drilled and another alumina tube attached to allow introduction of various gases/compositions to this side.

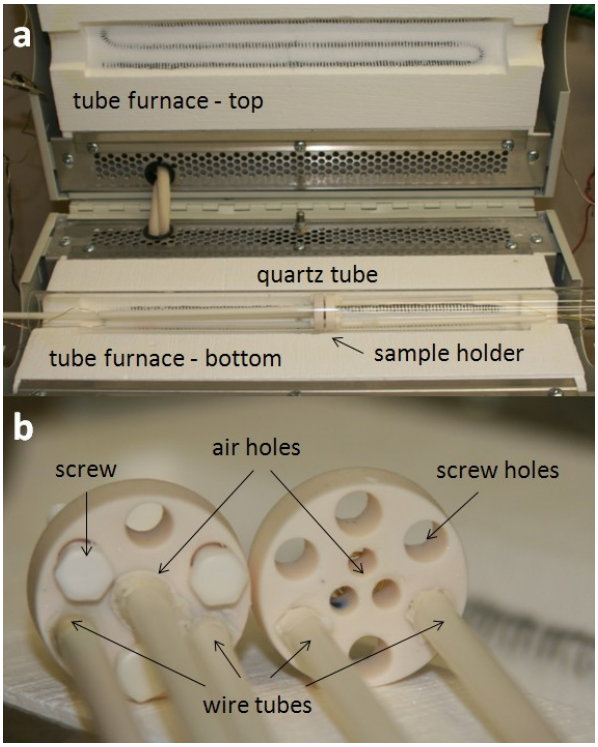

Figure 22: a) Lindberg-Blue tube furnace (in open position) with quartz tube and alumina sample holder. b) Alumina sample holder (outside) with ceramic screws, alumina wire tubes and air holes (the half on the left side has an alumina tube attached for providing different feed gases).

Since all parts of this holder were made from alumina and gold wires were used, the potential for sample poisoning with elements from the setup/holder was minimized (e.g. Cr poisoning as described earlier). To measure the current through our cells, a four-probe measurement setup was chosen to eliminate the contributions from the wires. The 0.5 mm pure gold wire was bent into a spiral and threaded through the alumina tubes, as shown in Figure 23. After placing the symmetric cells in between the gold contacts (and the holder), ceramic screws (99.5% purity, Ortec Inc.) were used to firmly press the holder and gold contacts onto the sample. This ensured a good contact at high temperature by eliminating the possibility of loosening, due to differences in the coefficient of thermal expansion (CTE).
After inserting the sample into the quartz tube and subsequently into the tube furnace, the four gold wires were connected to a BK Precision power supply (type 9121A) with remote voltage sensing capability. The power supply was connected to a PC and controlled by a self-written Lab View program, performing the potentiostatic current measurement and collecting data for runs up to 100 hours.

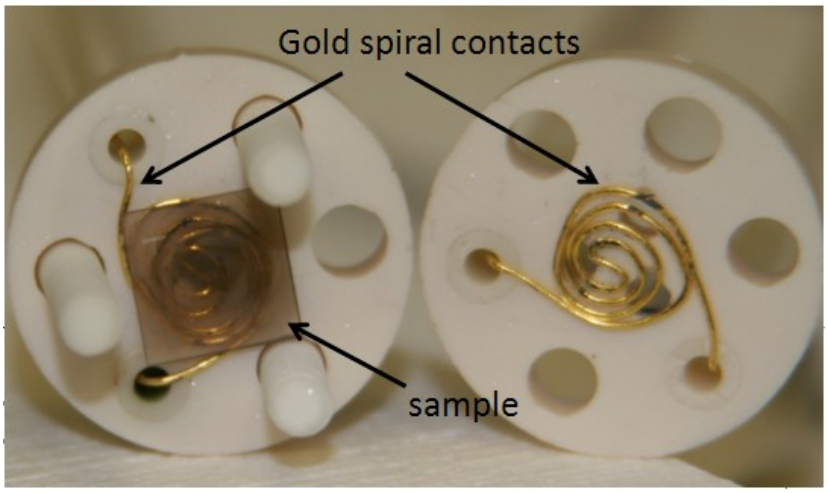

Figure 23: Open view of the ceramic sample holder with gold spiral electric contacts, holding a symmetric cell sample made by PLD. The plus sign inscribed at the upper left corner shows that the anode (electric positive) side is facing us and the backside, still in contact with the gold, is the cathode (negative) side.

After starting the four probe measurement with a constant voltage of 500 mV across the sample and tracking the resulting current, the samples were heated with a ramp rate of approx. 4˚C per minute to 800˚C, held at this temperature for 100 hours and then cooled down to room temperature with a rate of 3˚C per minute. After the cool-down and extraction from the holder, the polarity of each side was inscribed into the sample surface using a razor blade. In addition to the potentiostatic measurements, I vs. V curves were taken at 800˚C from 0 to 5 volts with different voltage scan rates. All sample properties, experimental parameters and numbers are comprised in Table 2.

		Date heat treatment	**Film growth date**	**Set**	**#**
As deposited	no GDC		050111.015 - 110111.016		
	with GDC		130111.017 - 140111.018		
Heat treated	no GDC	s110222	170111.019 - 180111.020		1
	with GDC	s110406	210111.021 - 240111.022		2
500 mV bias voltage applied for 100 h at 800˚C	no GDC	s101217	first try	a	3
	no GDC	s101228	091110.009	b	4
	no GDC	s110207	250111.023 - 270111.024	c	5
	with GDC	s101222	first try	a	6
	with GDC	s110104	131110.013	b	7
	with GDC	s110215	280111.025 - 310111.026	c	8

Table 2: Overview sample properties, treatments and numbering scheme for the PLD deposited, thin film symmetric cells used in this study. Growth a,b, and c had different thermal contacts with the sample holder during PLD growth (see text) resulting in film changes.

5.3. Sample Characterization

After sample preparation and running them in the previously described testing apparatus, the samples are characterized with respect to current degradation, I-V behavior and structural evolution in the following part. The differences between samples with and without GDC interlayer are explored, the structural evolution observed and the impact of the polarization on it analyzed.

5.3.1. Potentiostatic Current Degradation

The results of the potentiostatic current degradation experiments are displayed in Figure 24. Three samples of each type a, b and c (w/ and w/o GDC interlayer, different growths, see Table 2) were run for 100 hours at 500 mV and the current was recorded. Since the voltage was already applied at room temperature, an initial heating transient is observed until the sample temperature reaches 800˚C. This heating transient can be explained by the activation energy necessary for thermal activation of both, oxygen reduction at the cathode and oxygen conduction in the electrolyte [49, 69, 70]. Afterwards all samples show a rather rapid initial degradation during the first 10 to 15 hours, which seems to slow down and even to level off towards the end of the 100 hour runs. As expected, the samples with GDC interlayer perform much better in terms of total ion current, but show a higher degradation rate (steeper slope) as well.

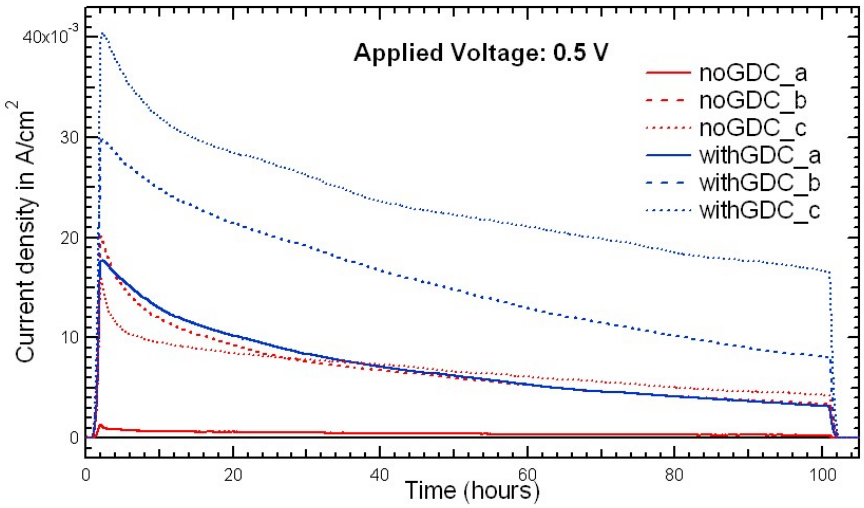

Figure 24: Current vs. Time plots for samples with and without GDC interlayer, from three different PLD growths a, b and c, with and without GDC interlayer and a constant applied bias potential of 500 mV.

However, in general we see an improvement in sample performance (current density) with the number of growths. This might be explained by the fact that the sample holder was modified after a couple of growths, leading to more homogeneous heat distribution across the sample during growth (see chapter 5.1)

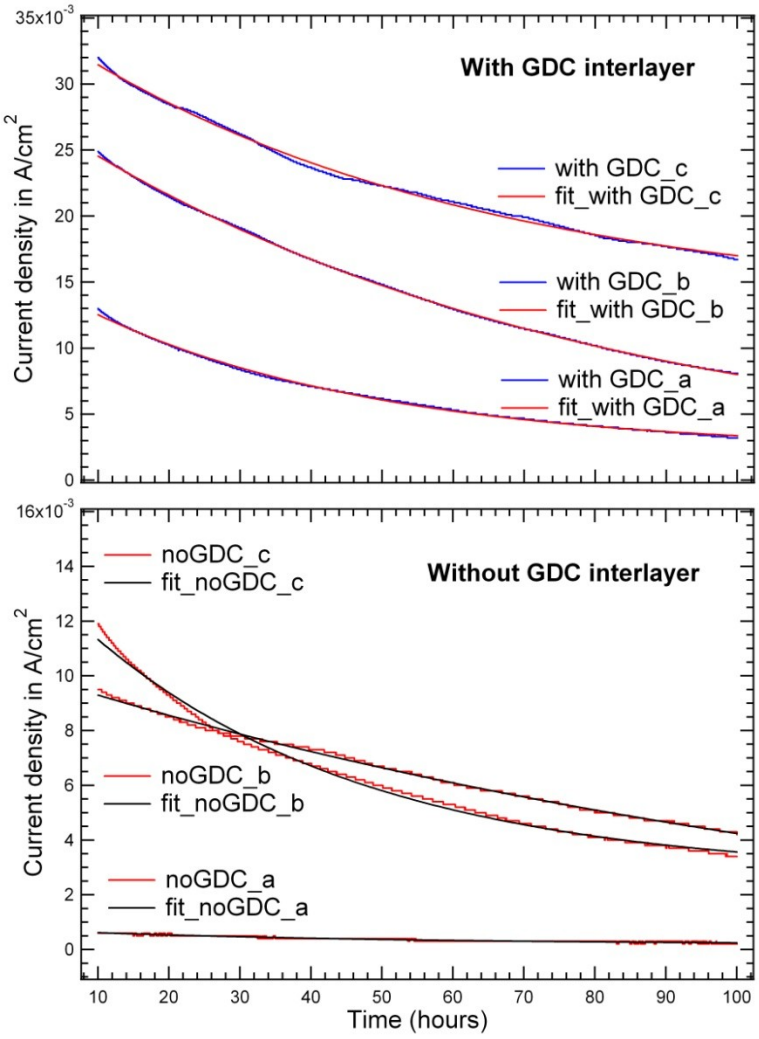

Figure 25: Current degradation for the samples shown in Figure 24. All curves were fitted with an exponential function in the region 10 hours to 100 hours to exclude the initial and final heating transient and the rapid degradation during the first hours. The fit parameters can be found in Table 3.

The long term degradation is estimated by fitting the data between 10 and 100 hours, shown in Figure 25. In general it is difficult to determine the time dependency of the current degradation since more than one factor might play a role, e.g. coarsening of the LSCF grains in the cathode, segregation of secondary phases at the surface, interface or grain boundaries, poisoning with gaseous species from other materials in the system and/or growth of defects in the film. Especially, since they in turn can have more than one origin – the kinetic or field-induced de-mixing of the cathode LSCF for example, both contributing to the segregation/secondary phase formation. In SOFC stack tests, the long term degradation (after and over thousands of hours) is normally given in % current reduction per 1000 hours of operation[55, 71]. Our experiments were conducted over shorter periods of time, making it difficult to give reliable values for such long times and our samples differ significantly from normal SOFCs, thus showing much higher degradation. This is in part due to the fact that our cathode and anode layers are dense and very thin, leaving them especially susceptible to the structural degradation mechanisms mentioned above. This is also the reason why the current and power density is relatively low for

these samples (see detailed explanation below). In order to compare the degradation of our samples, an exponential function was chosen to fit the data between the relevant points, since it best represented the data. The range 10 to 100 hours was chosen to exclude the initial and final heating/cooling transients and the rapid degradation during the first couple of hours which is most likely due to the grain formation in the PLD deposited cathode, anode and interlayers which were amorphous after deposition. An exponential function of the form:

$$I\ t\ = I_{\infty} + A \cdot e^{-\frac{t-t_0}{\tau}}$$

was used, with I the current density at time t, t_0 the shift of the curve to 10 hours (and thus not a fitting parameter) and the three fitting parameters I_{∞} (representing the asymptotic value of the cell current density), A (the current density at t=10 hours above I_{∞}) and τ which shall be called degradation parameter here. A summary of the fitting parameters used in fitting the current vs. time curves for both types of samples shown in Figure 25 is given in Table 3.

Sample / Fit parameter	with GDC a	with GDC b	with GDC c	no GDC a	no GDC b	no GDC c
I_{∞}	$2.26\text{x}10^{-3}$	$0.97\text{x}10^{-3}$	$13.1\text{x}10^{-3}$	$0.18\text{x}10^{-3}$	$2.69\text{x}10^{-3}$	$-1.26\text{x}10^{-3}$
A	$10.3\text{x}10^{-3}$	$23.6\text{x}10^{-3}$	$18.3\text{x}10^{-3}$	$0.44\text{x}10^{-3}$	$8.63\text{x}10^{-3}$	$10.6\text{x}10^{-3}$
τ	40.3	74.3	57.8	47.9	39.2	138.3

Table 3: Fit parameters I_{∞}, A and τ for the current degradation fits in Figure 25.

The initial performance of all samples is increasing with the number of deposition, as explained earlier. However, the degradation is different for each sample as well and does not seem depend on the current density, but rather on the sample characteristics. If the parameter τ is used to compare the degradation between samples, we see that the ones with GDC interlayer degrade faster (except sample "no GDC a") but have a much higher initial current density (I_{∞}+ A) and final current density I_{∞}. From those trends, it seems likely that on one hand, the GDC interlayer increases the initial performance of the cell by at least a factor of 2- 5 but on the other hand, its degradation might be the reason for the higher degradation rates. The origin of this fast degradation of the GDC interlayer is difficult to determine, since both layers are amorphous at first, but then recrystallize when the sample is heated to 800˚C. During this recrystallization process, it is possible that cations from YSZ or LSCF diffuse into or through the GDC, leading to secondary phase formation, either in the GDC layer or at the interfaces. Additionally, the higher initial current density could lead to deterioration of the interface due to enhanced cation drag (e.g. field de-mixing[72]) by the oxygen ions permeating the interface. Especially interesting is the question whether the observed enhanced degradation is due to Sr segregation comparable to the one investigated in Chapter 4. In a similar line of argument, a higher current density would lead to a higher oxygen vacancy concentration at the cathode and a lower one at the anode, respectively. This change in vacancy concentration and resulting Sr segregation would reduce the electro-catalytic activity of the LSCF and thus the oxygen reduction reaction leading to the observed current degradation.

To gain additional insight into how the degradation affects the current through the cell, the mechanism which limits the current, in addition to the ohmic drop in the electrolyte, has to be determined. One of the cells was therefore characterized with I-V curves of variable voltage ramp rates as shown in Figure 26 (top). Since our cells consist of dense rather than porous cathode films, the oxygen ions, after their reduction on the surface, have to be conducted through the LSCF cathode to pass into the GDC interlayer or directly into the YSZ electrolyte. Similarly, on the anode side the oxygen ions have to travel through the anode LSCF to recombine at the LSCF surface. Thus, our electrodes work different than porous ones since they exclude the direct reduction of oxygen at the TPBs and thus direct transfer of oxygen into the electrolyte. (As a result, the performance of our cells is much lower than that of a real cell with porous LSCF electrodes and changes in film morphology or composition can and will lead to much faster degradation, as discussed earlier.) However, in a similar matter to porous cathodes, the rate controlling mechanism for observed current can be identified from the I-V behavior of the sample using theoretical calculations by Svensson et al., which incorporates significant differences between the material system investigated here and conventional electrochemical theory[66].

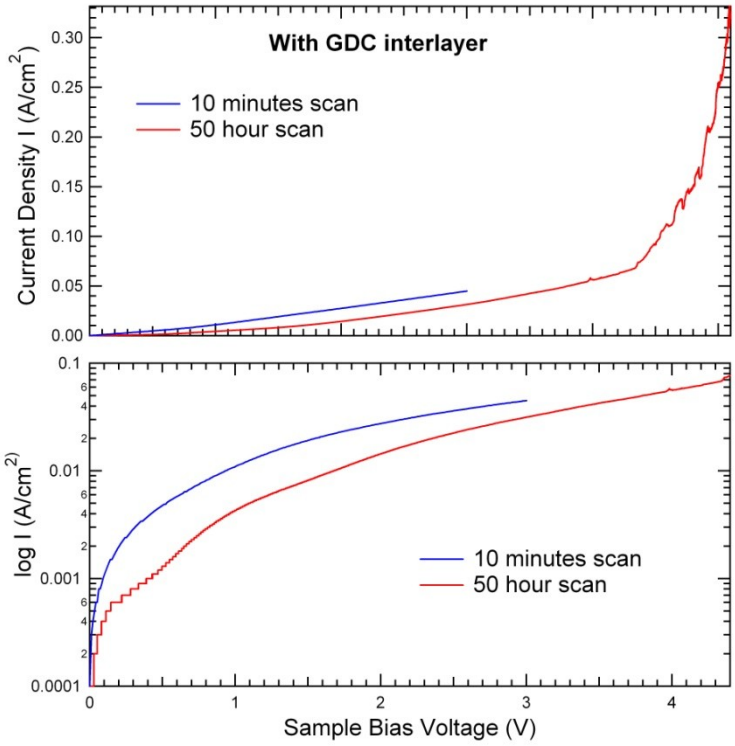

Figure 26: top) Current vs. Voltage plot for a sample with GDC interlayer and two different ramp rates, 10 minutes from 0 to 3 volts (blue) and 50 hours from 0 to 5 volts (red); bottom) Log I vs. V plot for the same measurement between 0 and 4.5 volts.

There are two rate limiting steps, adsorption of oxygen at the LSCF surface and exchange of this oxygen with the bulk. Knowledge of which one is the rate determining step might yield valuable information about the impact that the different degradation mechanism could have on the cell current. Two different rates were chosen for ramping up the applied bias potential. In the first case (blue curve in Figure 26), the bias potential was

increased from 0 to 3 volts in only 10 minutes, in the second case (red curve) it was increased from 0 to 5 volts over the course of 50 hours. As seen in Figure 26 bottom, a log I – V plot reveals that for the high ramp rate, no Tafel behavior is observed (Tafel behavior = ideal, linear log I-V behavior). In contrast, the low ramp rate exhibits almost ideal Tafel – like behavior above 1.5 to 2 volts. According to Svenson et al. this can be seen as strong evidence that, in the first case (high ramp rate), the current was limited by the adsorption of oxygen at the surface of the LSCF, whereas in the second case (low ramp rate) the current was limited by the exchange of adsorbed oxygen at the surface with the bulk. This is also supported by the observation that, in the high ramp rate case, the current density is higher than in the low ramp rate case which is also in agreement with the theoretical predictions by Svensons et al.[66]. Furthermore, in the high ramp rate case the argument of adsorption limitation is plausible, if one considers that the sample might not have been able to reach equilibrium with the gas phase during the short scan time (gas layer right above the cathode and anode side). Around 4 volts, the sample current kinks and increases dramatically, which is probably due to cell failure, as structural damage was observed after removal of the cell from the testing apparatus. In conclusion, when in equilibrium, the total cell current is most likely determined by the exchange of adsorbed oxygen with the bulk of the LSCF (in addition to the ohmic drop of the electrolyte). This is valuable information in judging the impact of structural degradation on the cell performance. Since the exchange of adsorbed surface oxygen with the bulk requires oxygen vacancies, secondary phases that lack those (like SrO) will have a significant detrimental effect. Additionally, changes in composition that mostly affect the vacancy concentration rather than electro-catalytic activity, will also result in more severe degradation.

5.3.2. Film Morphology via FE-SEM and EDX

In order to characterize the samples with respect to the change in film morphology, FE-SEM was used to track the morphological changes induced by high temperature and applied bias potential. Upon visual inspection, the “as deposited” samples showed no inhomogeneity whereas the ones used in the high temperature test setup showed slight spiral discolorations, due to the contact with the gold electrode. Overview pictures of the sample surfaces were made with low magnification SEM for orientation purposes and high magnification ones to investigate the microstructure of the film. Shown in Figure 27 is a typical SEM micrograph with high magnification (50.000 times) of a sample “as deposited” by the PLD process (top) and one with low magnification (4.000 times) after treatment in the high temperature test setup (bottom). The “as deposited” sample shows smooth, amorphous like film structure with small (~ 0.1 µm) particles distributed randomly over the surface. The sample after heat treatment shows a smooth area, expanding from the lower right corner towards the upper left. This is the area where the gold spiral was in contact with the sample, subsequently forming the spiral pattern visible with the naked eye. EDS linescans across this area showed no evidence of significant gold deposition on the sample surface within (the probably large) experimental errors in determining the Au peak intensity (see EDS discussion below). Around this contact area, the surface morphology is dominated by crystallites on a polycrystalline LSCF film (slightly whiter than the LSCF film itself).

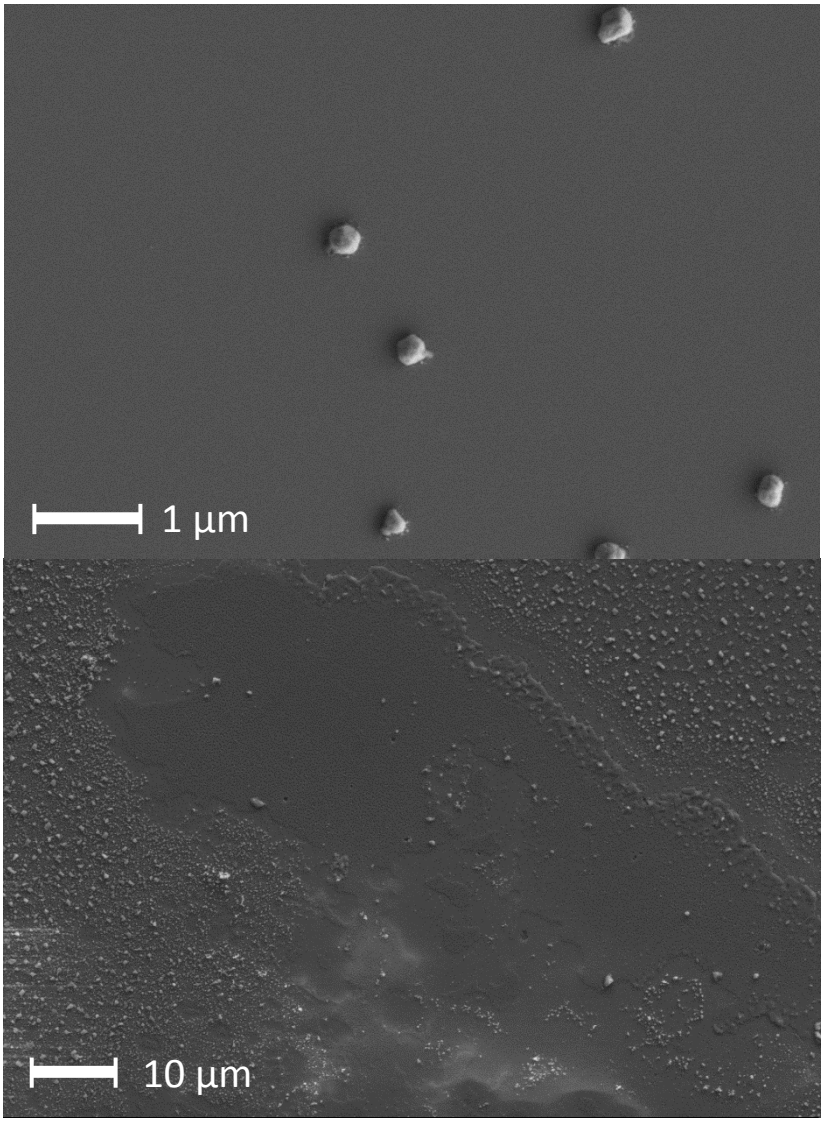

Figure 27: Top: High magnification SEM micrograph of a sample "as deposited" by PLD, showing a smooth, homogeneous film with small deposits ("white spheres", E_0= 2 keV). Bottom: Low magnification image after 100 hours at 800˚C and an applied bias potential of 500 mV. The smooth area from the lower right to upper left corner is part of the contact area of the gold spiral (E_0= 12 keV).

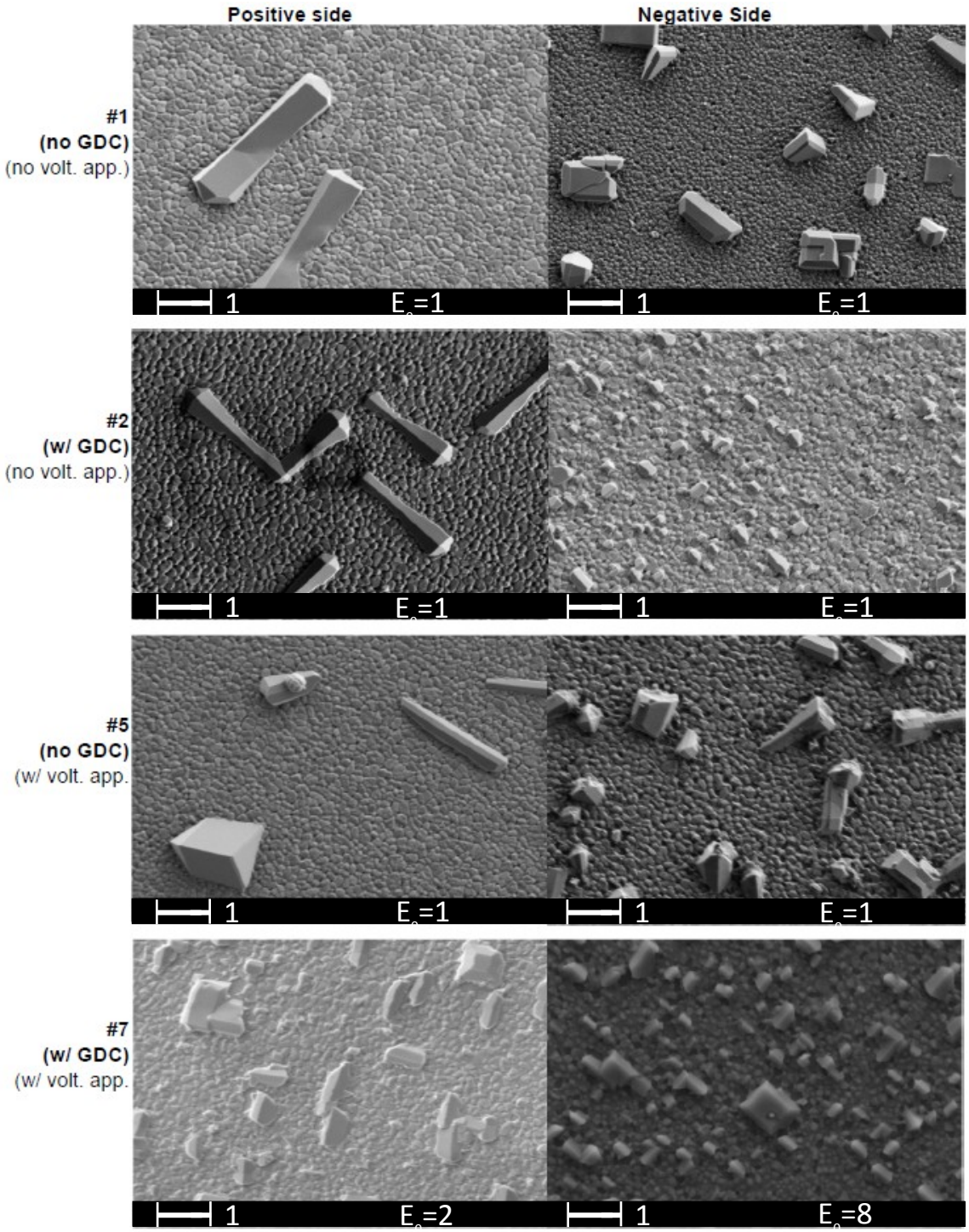

Figure 28: High magnification images of both sides of the heat treated samples (no applied bias voltage, top 4) and two samples with applied bias voltage (500 mV, lower 4), showing the microstructure of the LSCF film as function of treatment.

The high magnification pictures in Figure 28 show the microstructure of the LSCF film for representative samples for both treatments (with and without applied bias voltage, see Table 2). It shows the LSCF film to be dense and polycrystalline with an average grain size of <0.1 µm. Especially for the positive side of the just heated samples (left side,

upper 2 in Figure 28), the large crystals on top of the film seem to be thin and elongated in one direction. For the negative sides of these samples (right side, upper 2 in Figure 28), the film without GDC interlayer shows crystals of the same size but not as elongated, whereas the film with GDC interlayer shows smaller crystals but much more than the other samples. In case of an applied bias voltage, the crystals are neither small nor elongated and look to be much denser than in the just heat treated case.

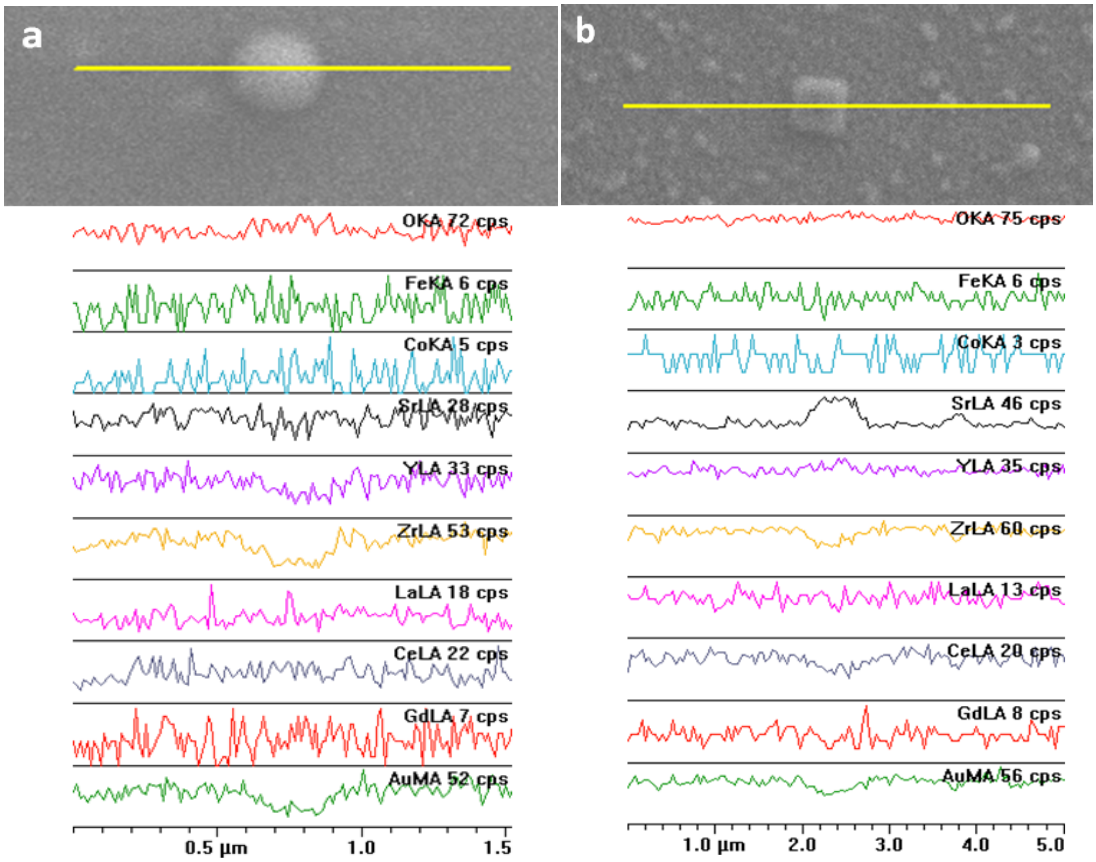

Figure 29: EDX linescans along the yellow line in the FE-SEM images at the top. a) "as deposited" sample, linescan across the particles found on the surface. b) heat treated sample (no bias voltage), linescan across the crystallites found on the surface. (The Y axes are in counts per second (cps, not shown) of the emitted X-rays, the cps value next to the element represents the highest value in the respective graph.)

To evaluate what the particles and crystals are composed of, EDX was performed and the results are shown and discussed later in this section. Since we want to investigate a possible impact of the applied bias potentials on the film morphology, grain size distribution analysis was done as well, in order to find possible links between bias potential and grain growth. The nature of these crystallites was investigated using Energy Dispersive X-ray Spectroscopy (EDS or EDX) to determine their composition and thus possibly their origin. EDX linescans of both, a particle on the "as deposited" film (left side, a) and a crystal on a heat treated sample with GDC interlayer (right side, b) are shown in Figure 29.
For the line scan in Figure 29 a) the electron energy was 12 keV and the length of the yellow line in the SEM image at the top is 2.1 µm. At a total of 128 points (0.017 µm

apart) the count rate of preset peaks (O-Kα, Fe-Kα, Co-Kα, Sr-Lα, Y-Lα, Zr-Lα, La-Lα, Ce-Lα, Gd-Lα, Au-Mα) was recorded and displayed in a diagram below the SEM image. In Figure 29 b) the same primary electron energy was used but the length of the scan is 5 µm (128 points, 0.039 µm apart). The collection time was 7.5 and 11 minutes for cases a and b, respectively.

For the "as deposited" sample, we can see a clear reduction in count rate for Y-Lα and Zr-Lα in the region of the particle, whereas the other elements show now change. To explain this change, we have to consider the probing depth of EDX. Typically, EDX probing depths at the used primary energy are 0.8 – 1.5 µm[73], mainly due to the interaction volume of the fast (high energy) electrons with the sample and the attenuation (absorption) of the created X-ray by the sample itself. Since this is much larger than the thickness of the film, we see a much larger count rate for the single crystal YSZ substrate than for the GDC or LSCF films. However, since the particles and crystals on the surface are rather thick (probably around 0.1 µm), there is a visible reduction in the substrate signal when measuring points across the particle. The Fe-Kα, Co-Kα and Gd-Lα intensities are so low that they do not yield usable information. The Au-Mα peak measured here overlaps heavily with the Zr peak, leading to the high Au counts even though the "as deposited" sample was never in contact with gold. Within the experimental error, no gold deposition was detected, even at the contact points of the gold spirals with the sample. From these results, the conclusion for the "as deposited" sample about the nature of the deposits is, that they are either droplets of LSCF material from the PLD process, or contaminations from exposing the samples to the ambient air (e.g. dust). From the somewhat crystalline and regular shape, visible in Figure 27 top, the former of the two seems more likely.

In case of the heat treated sample, Figure 29 b, the count rates for the YSZ substrate decrease when measuring across the crystal. In addition, the count rate for the GDC interlayer goes down, observable in the Ce-Lα graph. Again no change is observed for Fe-Kα, Co-Kα and Gd-Lα due to low count rates. However, a huge increase in the Sr-Lα combined with no change in the La-Lα intensity shows that the particle has to be Sr rich. The count rate (not given in the Figure) almost doubles from a 24 cps baseline to 43 cps for the peak. This is strong evidence that Sr segregates at the surface forming a secondary phase (SrO or at least very Sr rich LSCF). In view of this evidence, investigating the grain growth with and without applied bias potential might not only yield information about film morphology but also the impact of applied bias potentials on Sr segregation.

5.3.3. Grain Size Analysis

To measure and quantify the grain structure of the various samples, low magnification backscatter FE-SEM images of the samples were taken, having a higher elemental contrast due to the strong z dependence of the backscatter intensity[74], resulting in better visibility of the segregated grains. The larger area results in more grains usable for analysis and gives much better statistics. To analyze the grain structure of the samples, the online program "Simagis Live" (version 2.1 beta) was used. After uploading the SEM images, the particles on the surface were determined by the function "Particle analysis". To distinguish the particles from the background, the intensity of the pixels was used and parameters like minimum and maximum intensity of the particles were optimized to ensure that all particles were detected by the software. Subsequently, the dimensions of the picture and the length per pixel were used to compute the particle dimension in meaningful units (rather than pixels) and the distribution statistics.

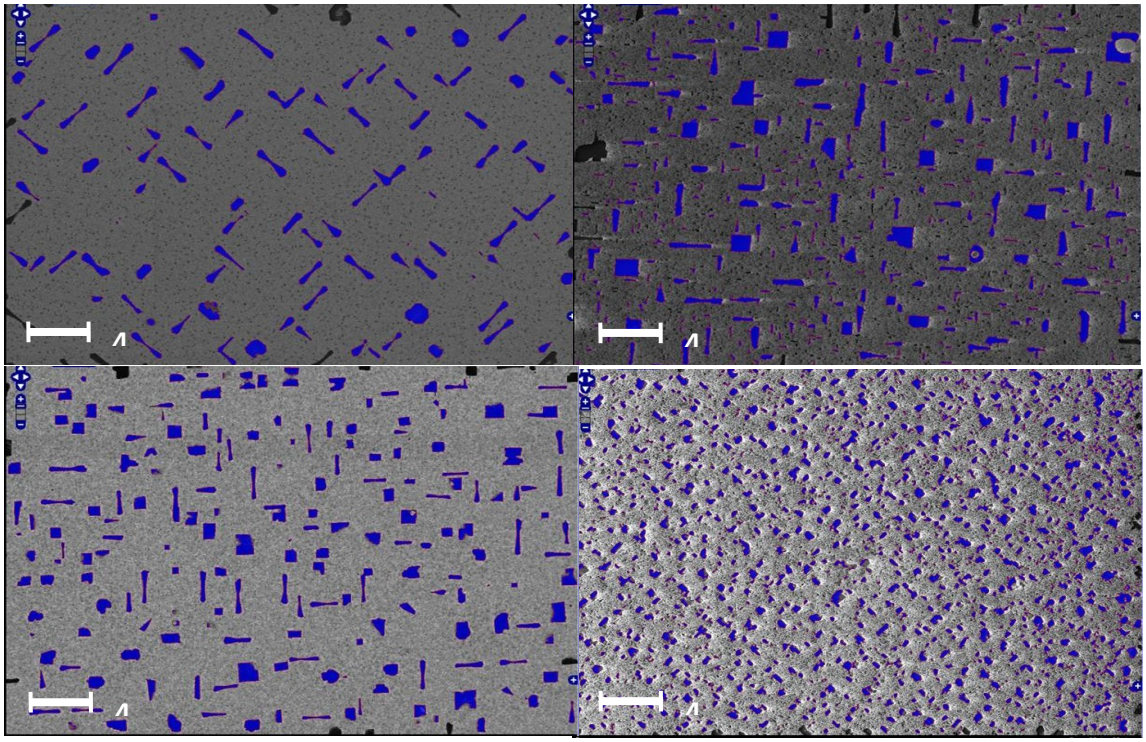

Figure 30: Backscatter SEM images used in the "Simagis Live" software. a) and b) positive and negative side of sample #2 (GDC interlayer, no bias potential, see Figure 28 and Table 2). c) and d) positive and negative side of sample #7 (GDC interlayer, 500 mV bias potential). The LSCF film is light gray (background) and the crystals appear black (or blue, if marked) E_0= 1 keV.

The images used by the software are shown in Figure 30 for both sides of samples with GDC interlayer, without applied bias potential (top) and with applied bias potential (bottom). The LSCF film itself is gray, whereas the crystals on the surface appear black in the SEM image and were marked blue by the software with the boundary being red (note that crystals touching the edge were not measured). The software parameters were chosen

to (visually) match the marked areas with the black crystals as accurately as possible. The software automatically computes area distribution values and elongation factors which are given in Table 4. The mean area provides information about the number of nucleation sites and the total area covered with crystals gives hints about the availability of growth material. High segregation means high amounts of available material which results in high nucleation and high coverage (assuming all other parameters are the same, e.g. surface diffusion coefficient, critical nuclei size. etc.)[75]. Thus, the large number of small crystals in combination with the higher coverage points towards a higher segregation rate for the sample with applied bias potential (c and d). As seen in Table 4, the mean area on the positive side is larger than that on the negative side for each sample. However, when comparing the sides between samples, with an applied potential the crystal size is smaller relative to the heat treatment only case. In the heat treated case, the crystals are more elongated as well, manifesting in a smaller elongation factor (the larger it is, the rounder the crystals). To obtain the size distribution of the crystals, the program has the option to print a list of all identified particles with their location and size. This data was used to compute the total crystal coverage of the sample as given in the last row of Table 4 and to generate a graph of the size distribution of the crystals which is shown in Figure 31.

Sample	#2 heat only positive side		#2 heat only negative side		#7 appl. bias V positive side		#7 appl. bias V negative side	
Parameters	Area μm^2	Elongation factor	Area μm^2	Elongation factor	Area μm^2	Elongation factor	Area μm^2	Elongation factor
Min	0.01	0.17	0.03	0.18	0.01	0.13	0.01	0.30
Max	1.10	0.86	1.74	0.86	1.03	0.91	0.53	0.90
Mean	0.36	0.41	0.19	0.46	0.32	0.52	0.08	0.61
Std. Dev.	0.21	0.19	0.25	0.15	0.19	0.22	0.07	0.12
Total area	37.0 μm^2		66.5 μm^2		60.7 μm^2		89.4 μm^2	

Table 4: Crystallite area, elongation factor and coverage for both sides of two representative samples, without applied bias potential (#2, heat treatment only) and with applied bias potential (#7, appl. bias V) are compared with respect to Minimum-, Maximum-, Mean-, Total area and Standard deviation.

The size distribution shows clearly that an applied bias potential boosts crystal growth, as this sample has a much higher number of crystals on both sides, while the distribution shape seems to be similar. For the negative side, the distribution looks like an exponential, whereas for the positive side it looks more like a distorted Gaussian curve. This trend is also observed in the total crystal coverage, given in the last row of Table 4. Since smaller crystals can be flatter and FEM cannot provide height information, this total coverage cannot be translated directly to amount of crystalline material. However, these results warrant the assumption that applied bias potentials increase the crystal growth at the surface of these samples. The grain size analysis thus shows that the Sr segregation observed for thin films has a similar dependence on the electrochemical environment (applied bias potential) when compared to the samples and observation in Chapter 4, using porous LSCF electrodes. This is valuable information as it ties the Sr segregation in

the thin film "model" LSCF electrodes to the observed one in real, porous electrodes which are comparable to the ones used in actual SOFCs. This fact clearly shows that thin film cells can be used to investigate the underlying mechanisms of degradation occurring in real SOFCs and yield valuable information by providing a more controlled testing environment.

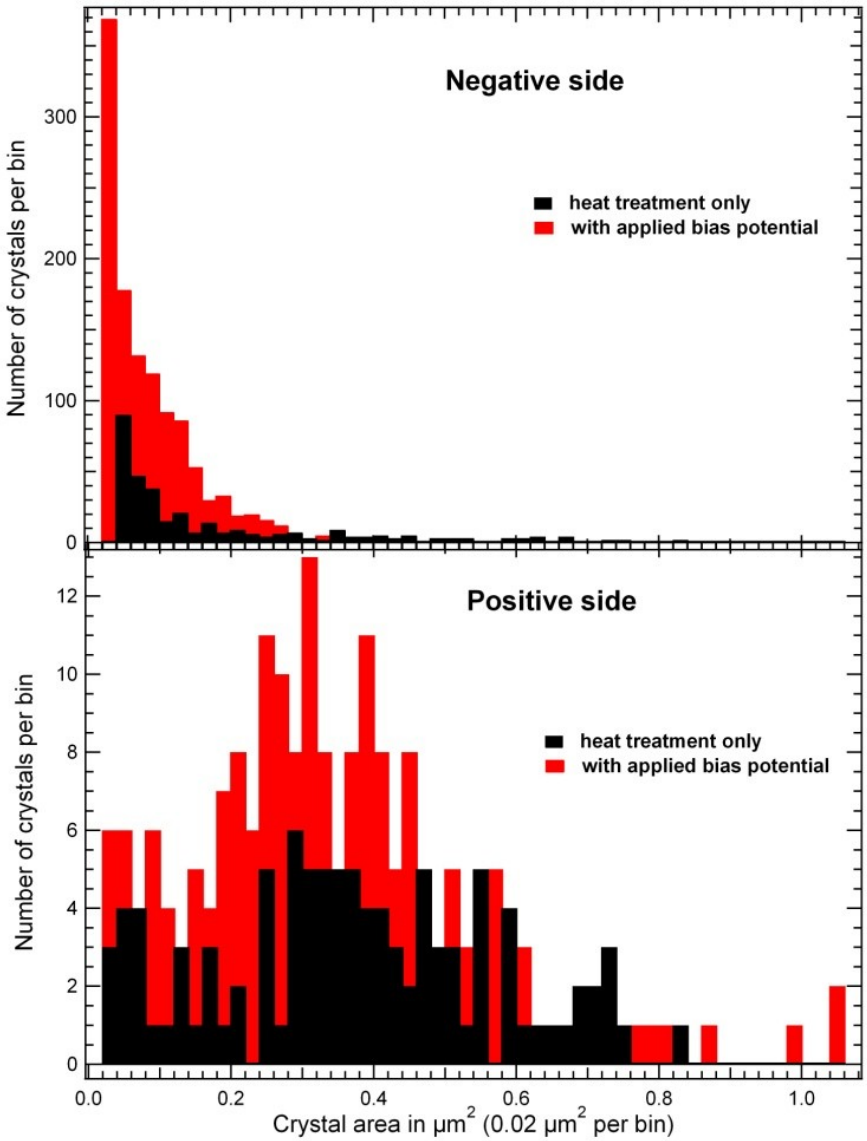

Figure 31: Grain size distribution for samples #2 (black, heat treatment only) and #7 (red, with applied bias potential) for the negative side (top) and positive side (bottom).

5.4. X-ray Absorption Mapping

After investigating the structural changes of the sample with respect to crystal growth at the surface, tying it to Sr segregation and analyzing the impact of an applied bias potential, changes in oxidation state of the elements in the LSCF film are measured using XAS. The new mapping capability is used in order to try to identify the more active regions on the sample and possibly link them to the observed Sr segregation.

5.4.1. Full Edge XAS and Comparison with XPS

As mentioned earlier, the X-ray absorption spectroscopy was conducted at ALS, using the fast-scan capability of beamline 6.3.1. The samples were attached to the sample holder by applying thin strips of silver paint to the edges, simultaneously serving as contact to the LSCF film on top of the insulating YSZ substrate. After introducing the samples into the endstation of beamline 6.3.1, XAS spectra of the complete La-M_{45}, Sr-L_{23}, Co-L_{23} and Fe-L_{23} edges were taken and are shown in Figure 32 (Fe and Co) and Figure 34 (La and Sr). All spectra were taken in total electron yield mode (TEY), which makes XAS sensitive to the first 1.5 to 14 nm of the sample[76-78] (e.g. 7.6 nm for the Fe L_{23} edge[76]) which is close to the thickness of the LSCF film. Other possible ways to measure XAS are total fluorescence yield (TFY) and transmission spectra. The first would be more useful for cathodes much thicker than the ones used here, due to the greater escape depth. For the latter, the samples are too thick and generating thinner ones is impractical. This makes TEY-XAS the perfect tool to investigate the thin film LSCF on the samples. To obtain spectra as the one shown in Figure 32 for Fe and Co, the data has to be normalized and the background has to be removed. The data treatment is described in the following section and subsequently the implications of the shown spectra are discussed. The acquired XAS data consist of photon energy, sample current (absorption intensity), beam current (I_0) and integration time per energy step.
As mentioned earlier, the fast scan method scans the grating continuously, rather than moving it in steps. Since the signal is integrated over a predefined energy interval and then assigned to the median energy, the signal can be influenced heavily by very small changes in the integration time per step. To normalize the spectrum and remove fluctuations in the electron beam in the synchrotron and absorption effects of the grating and other optical elements in the beamline, the spectra have to be normalized to the incoming beam current, measured with a gold grid at the chamber entrance (after all optical elements, right in front of the sample). However, when using very small energy steps or high scan speeds, additional noise is introduced by inconsistencies in the integration time for each step which can be quite significant, as shown for the Fe edge in Figure 33 (black curve).

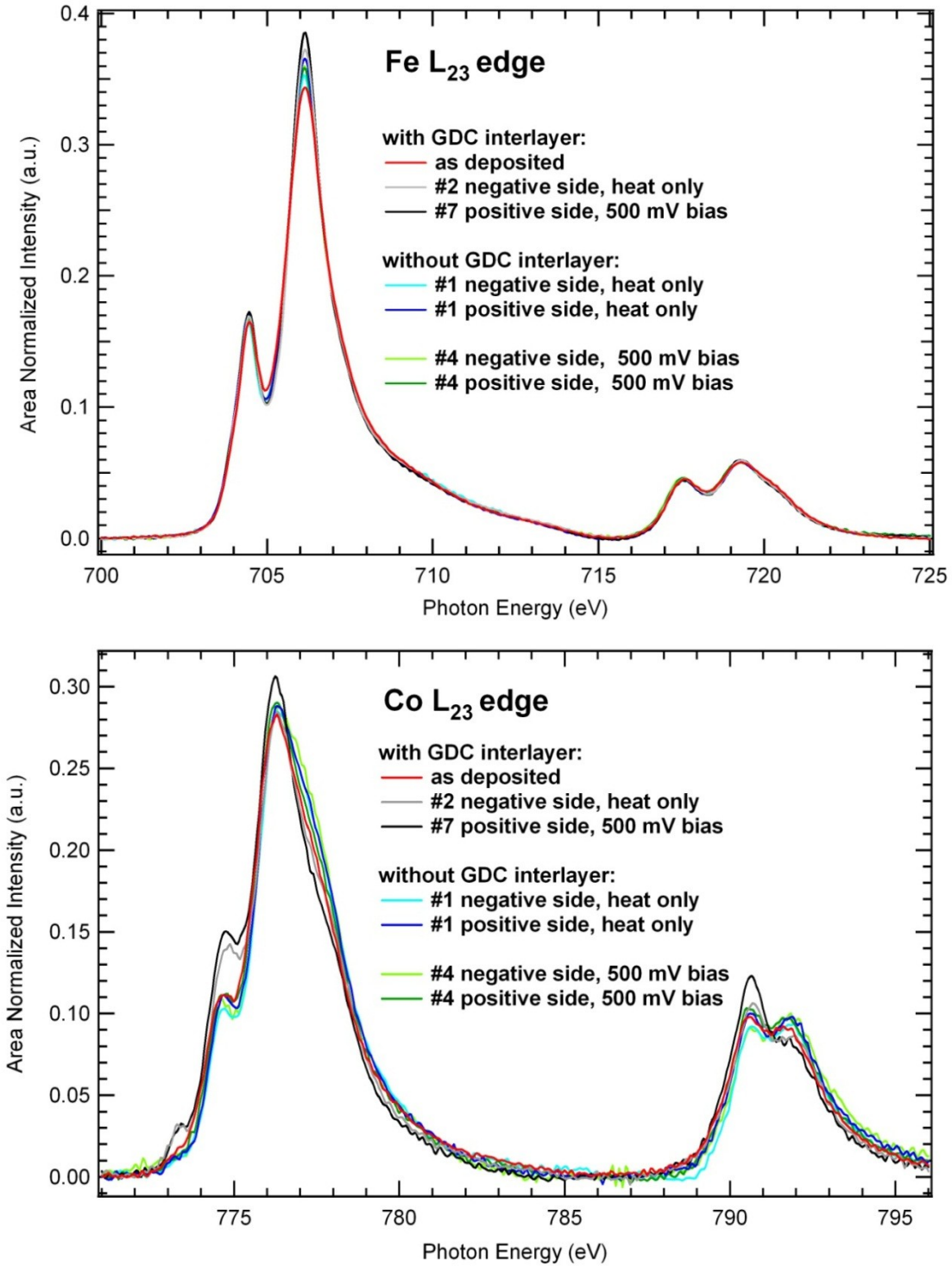

Figure 32: XAS spectra of the full Fe-L_{23} and Co-L_{23} edges for representative samples. Both are area normalized to the L_3 edge (low photon energy edge). Note the change in the relative peak heights of the Co L_3 edge peaks at 773.5 eV, 774.7 eV and 777.5 eV.

To eliminate this source of noise in the fast scan spectra, signal and beam current can be normalized using a constant reference signal. For this purpose, the output of a 1 MHz frequency generator is fed into the data acquisition system (conveniently one is already integrated in the V to f converter) and simultaneously recorded on a third channel.

Changes in the integration time per energy step are now precisely reflected by the intensity changes in this reference signal. Thus, the signal (and the beam current) can now be normalized (indirectly) by the integration time, reducing the noise greatly (Figure 33, green curve). This normalization however, is reversed when the spectrum is then also normalized to the beam current (Figure 33, blue curve) In order to normalize the signal to both, the beam current and the signal are first normalized by the integration time. Second, the beam current is smoothed using the Savatizki-Golay algorithm, preserving the area under the curve. Since the changes in the beam current have much larger scales than the changes in the integration time (tens of eV changes for beam current vs. ~0.1 eV for integration time errors) this smoothing preserves the fluctuations in the beam current due to optical elements and changes of the electron beam in the synchrotron but gets rid of the small changes introduced by the integration time fluctuations. The signal (normalized to the integration time) can now be normalized to the smoothed beam current without reversing the first normalization, shown in Figure 33 (red curve). This method yields much cleaner spectra and allows for even faster scan times and therefore all spectra were normalized in this fashion.

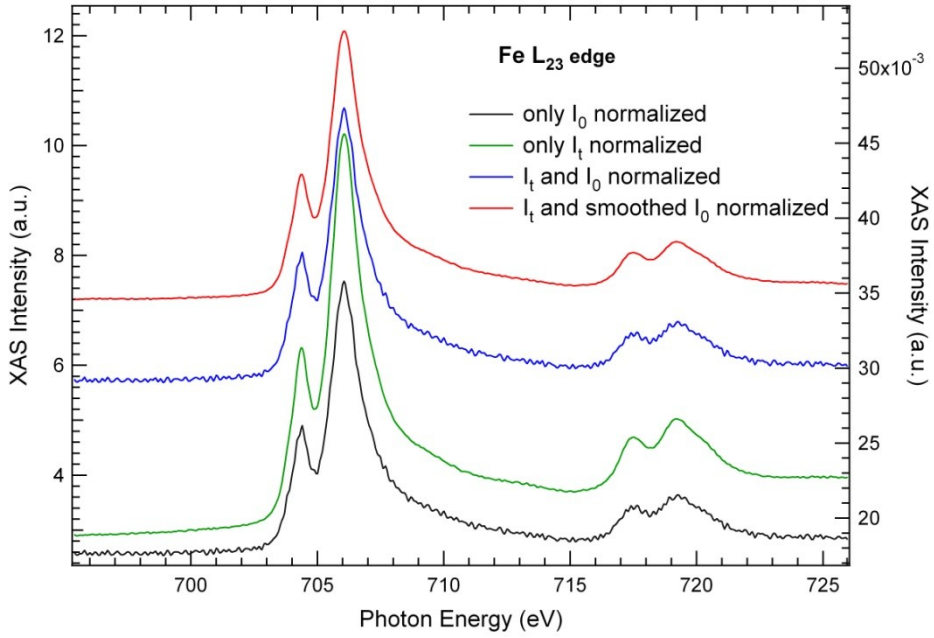

Figure 33: Different types of normalization shown on a Fe L_{23} edge fast scan. The black spectrum is normalized with the incident beam current I_0, the green one normalized with the integration time I_t (y axis on the right), the blue one is normalized with I_t and the I_t normalized I_0 and the red curve is normalized the same way but using a smoothed normalized I_0 and yields the cleanest spectrum with the appropriate background.

After normalization, the linear background has to be removed, stemming from the decrease in the total (non-resonant) absorption cross section. This is done by fitting a linear curve to the pre-edge signal and subtracting it from the spectrum. If done correctly, the post-edge part of the spectrum and (if the two edges are far enough apart) the middle part of the spectrum should then be zero since LSCF is an oxide without continuum states above the Fermi-level. (In contrast, metals have well defined post edge values, which can be found in the "Hankee" Tables and allow the determination of spin and orbital

momenta.) However, it is commonly found in oxide samples that the pre-edge slope is not the same as the post edge, resulting in the post edge being non-zero. This problem is not very well researched, but theories about the origin of these slope changes involve charging of the sample. When photon energies enable electron excitation, an additional channel for charging the sample is opened, resulting in the slope change of the background. To account for this, in some of the spectra a second linear function with a different slope was used to bring the post edge to zero. After background subtraction, the spectra were energy referenced and either area normalized or peak height normalized to the low photon energy peak for better comparison. As shown in Figure 32 the Fe and Co spectra were area normalized in order to accentuate differences in relative peak height. The Fe L_3 edge for example shows differences in peak height between samples, whereas the L_2 edge does not show these differences. In general, XAS measures the empty valence states which are in this case comprised of the t_2g and e_g states (see e.g. ref [6]). Changes in the spectral weight of the various features are thus indicative of changes in the electron population of a specific atomic orbital. An increase in intensity (area) means lower electron occupation, a lower intensity a higher electron occupation, respectively. For the Fe spectra, this means we can distinguish between the 3+ and 2+ oxidation states on one hand by measuring the total absorption cross section (which depends in the density of the final states) and compare it to the same measurement for the two oxidation states which is very hard to do. On the other hand, we can compare the relative peak height of the main and the shoulder peak (representing the t_2g and e_g levels) which is rather easy. For the additional electron in the 2+ state the intensity of the e_g level has to drop since there are less available empty states. This is confirmed in the literature, where a higher shoulder peak (lower main peak) is credited with the occurrence of Fe^{2+} ions[79]. However, care has to be taken as the peak ratio can also be affected by the site occupation of the iron atoms (octahedral vs. tetrahedral) which was shown for different phases of Fe_2O_3 [80].
The Co spectra show significant differences for the sample with GDC and without GDC. The samples without GDC (blues and green) and the "as deposited" sample (red) look almost the same, whereas the heat treated (grey) and biased sample (black) show additional peaks in the L_3 edge. The change in the relative peak heights of the peaks at 773.5 eV, 774.7 eV and 777.5 eV with respect to the 776.3 eV peak is obvious. This again can be interpreted using the above arguments. Unfortunately, the interpretation is not as easy in this case, due to the complexity of the spectrum with its many peaks. Relative peak intensity shifts between these peaks have to be used in order to extract the oxidation state. The most commonly used way is to compare the spectra to reference spectra of various Co compounds featuring the oxidation states of interest (see chapter 5.4.2).

Finally, the peak normalized La-M_{45} and Sr-L_{23} edges are shown in Figure 34. Whereas the La (top) shows no significant differences for any of the shown samples, the Sr (bottom) displays various features that differ from sample to sample. In general, the Sr signal shows much more noise which might be due to the increased probing depth at these higher energies, leading to a higher background contribution from the substrate. The most striking difference exhibits the "as deposited" sample (red). The L_3 peak is slightly broader, whereas the L_2 peak is much smaller than any of the others (a sign of charge transfer between the L_2 and L_3 edge, pointing to differences in the occupation of the d states between the "as deposited" sample and samples exposed to high temperatures). These differences might have their origin in the amorphous like structure of the "as deposited sample", leading to a different valence electron environment compared to the ideal perovskite structure, expected for crystalline LSCF. Additionally, the formation of

the Sr rich crystals at the surface could be responsible for the change in the L_2 to L_3 ratio. To get a better picture of the chemical state of the Sr, X-ray photoelectron spectroscopy was performed on the positive (anode) side of sample #4 (no GDC interlayer, heat treatment with applied bias potential).
The resulting Sr 3d spectrum is shown in Figure 35 (top), the oxygen 1s peak is shown at the bottom. The XPS spectra were acquired using monochromated Al Kα line with an energy of 1486.7 eV. The pass energy of the hemispherical analyzer was set to 23.5 eV and its work function 3.9 eV was used to determine the binding energy (x-axis). The sample was neutralized with an electron gun, calibrated using the C 1s peak. After a linear background subtraction, the Sr spectrum (top, black curve) was fitted with four peaks. These two sets of two peaks are the 3 $d_{3/2}$ and 3 $d_{5/2}$ spin-orbit split peaks (approx. 1.5 eV) corresponding to two different oxidation states of Sr.

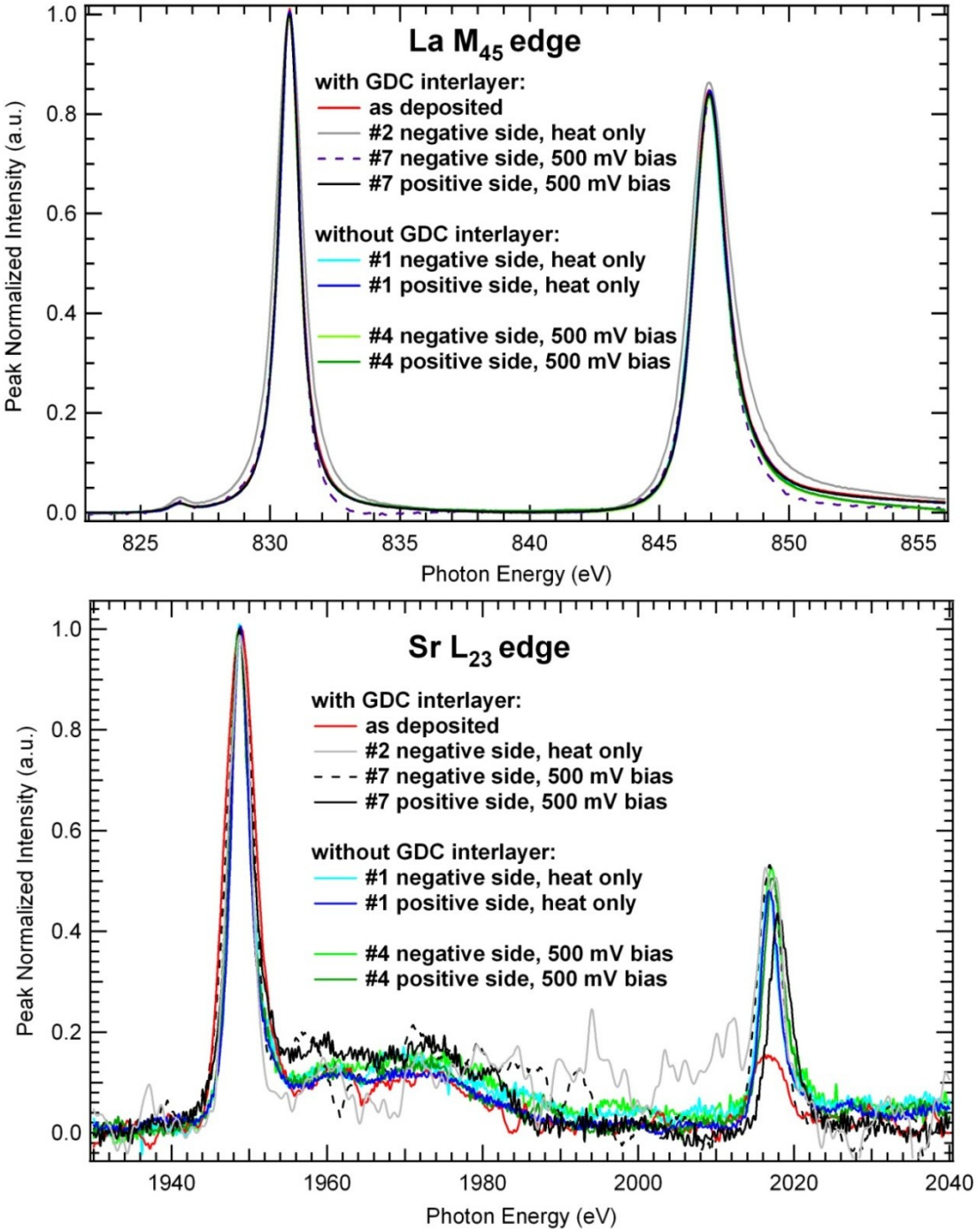

Figure 34: XAS spectra of the full La-M_{45} and Sr-L_{23} edges for representative samples. Both are peak normalized to the M_5 peak and L_3 peak, respectively. The increased noise might be due to the larger probing depth, increasing the background from the substrate. (Additionally, the red, grey and dashed black curves in the Sr graph were smoothed with 2nd order S.-G.)

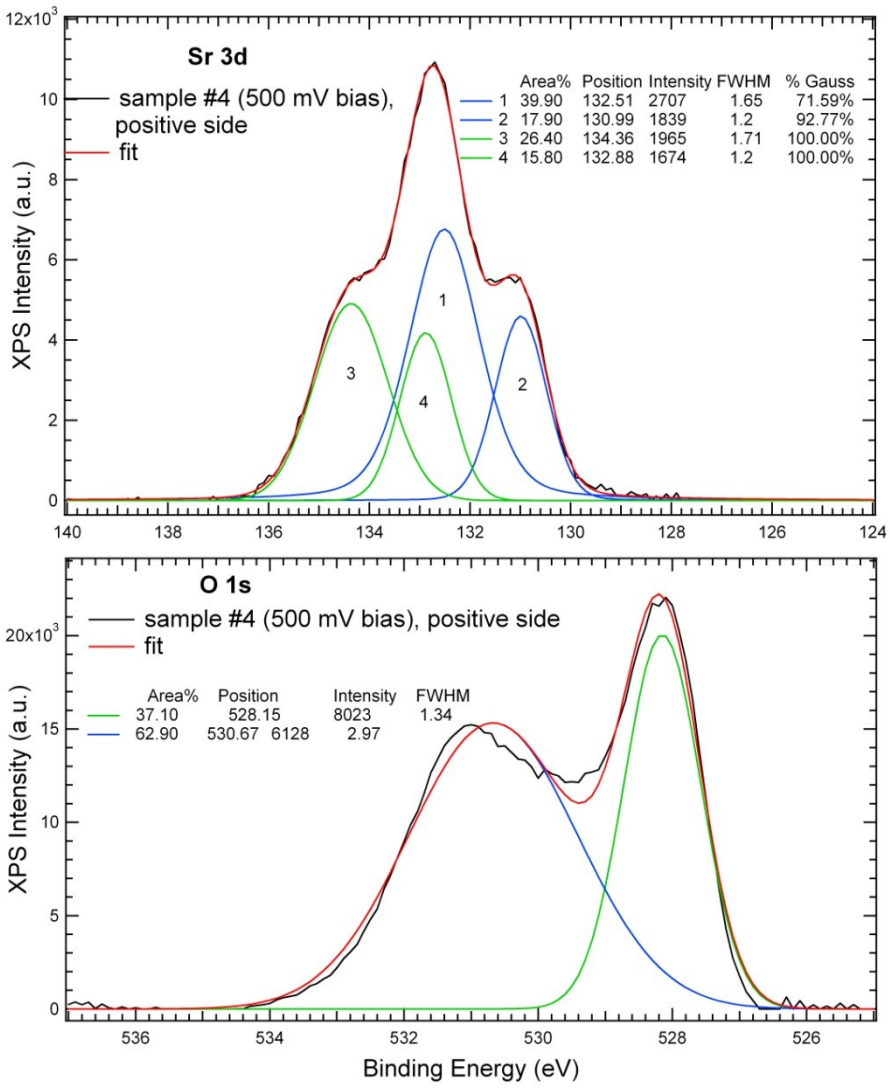

Figure 35 Top: Sr 3d XPS spectrum of sample #4 (no GDC interlayer, 500 mV applied bias), black line, with fit (red line) and the two sets of $d_{3/2}$ and $d_{5/2}$ doublets for the two different compounds SrO (3 and 4) and LSCF (1 and 2). Bottom: O 1s spectrum of the same sample, confirming the existence of the two chemically different phases.

In agreement with the literature, the two Sr phases are Sr in LSCF (low energy peaks 1 and 2) and Sr in SrO (high energy peaks 3 and 4), separated by about 1.9 eV. As shown in Appendix C1, Baumann et al. came to the conclusion that for anodic polarization (same as our sample), SrO segregates at the surface leading to the second set of (high energy) peaks with approximately the same intensities as the first (low energy) set. Since the probe depth of XPS is much smaller than XAS (on the order of <1 nm [77, 78]) the contribution of the small SrO crystals on the surface to the spectrum is much higher in XPS than XAS. The same fitting procedure was used to fit the O 1s spectrum, shown in Figure 35 (bottom). Even though the fit is worse, two clearly distinguishable O peaks confirm the existence of the surface secondary phase Sr in form of SrO crystals at the surface. Since XPS has such a low penetration depth, differences in the Co and Fe were not found and the La peaks were too low in intensity to do a similar analysis. However, XAS with its larger penetration depth and mapping capability is ideal to obtain the

distribution of the different Co oxidation states across the sample by analyzing differences in the Co peaks, as presented in the next part.

5.4.2. Cobalt Edge Mapping

In order to determine the valency state of the Co from the subtle peak changes seen in Figure 32 and map the distribution across the sample, it is easiest to compare the acquired spectra to reference spectra of known valency states. However, since XAS is not only sensitive to the oxidation state but also to crystal field, occupied crystal site, etc., reference powders of similar crystal structure are needed. After comparing the Co spectrum measured in the LSCF sample to various pure Cobalt-oxide reference spectra of different oxidation state without finding a good match, the only spectrum for adequate comparison was that of $CoFe_2O_4$ spinel (CFO). In Figure 36 (top), the spinel reference spectrum is shown (solid black) along with the LSCF spectrum (dotted black) and two spectra from the positive side of sample #7 (500 mV, with GDC, red dashed and solid).

Both sample spectra (red) could be accurately fitted with the weighted sum of the reference spectra (blue), 75% LSCF and 25% CFO in case of the spectrum acquired at z = 7 mm and y = 1 mm (solid) and 58% LSCF and 42% CFO for the spectrum at z = 3 mm and y = 1 mm. Whereas the oxidation state in pure LSCF at room temperature and stoichiometric composition is mostly 3+ with some 4+ and a small 2+ fraction[34], the oxidation state of Co in $CoFe_2O_4$ spinel is mostly 2+ and, as expected, resembles the Co^{2+} octahedral site spectrum very well [81, 82]. Thus, it is possible to extract the percentage of the Co oxidation states from each spectrum. In order to accurately do this, each spectrum should be fitted with the multiple peaks associated with the respective oxidation state and their respective percentages. Then, the peak area ratios could be used to accurately determine the oxidation state distribution. However, the multiplet structure for Co in these compounds is complicated and would have to be calculated in order to obtain all possible peaks contributing to the spectrum, e.g. using transfer multiplet calculations. This is very tedious and not the scope of this thesis, especially in view of the amount of data generated by the mapping. However, in Appendix C.2 a multi-peak fit of the two spectra is attempted, 5 possible peaks representing Co in its 2+, 3+ and 4+ state are used in order to fit the spectrum appropriately. Since those were chosen to fit both spectra reasonably and not obtained from first principle calculations, they can only serve as an estimate. It is much easier and thus faster, to use the reference spectra and their weighted sums to obtain an estimate of the oxidation state distribution by calculating peak ratios of representative peaks.

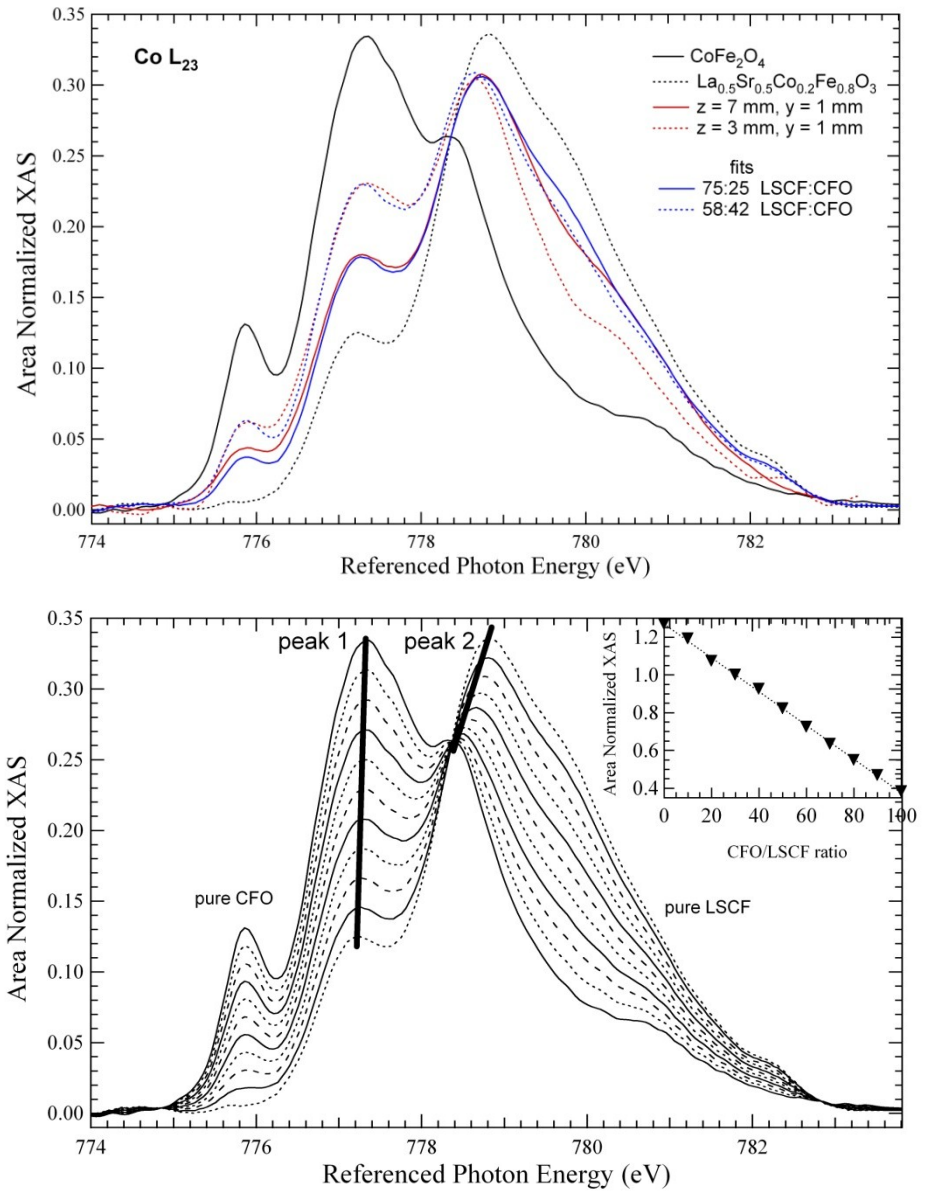

Figure 36: Top) Co L_{23} edge reference spectra of LSCF (black, dotted), $CoFe_2O_4$ (CFO, black, solid) and two spectra from two different spots on sample #7 (positive side, 500 mV, with GDC, red solid and dotted) and fits by using different percentages of the black spectra (blue lines). Bottom) Plot of the two reference spectra from top graph and their mixtures with different percentages in steps of 10% (peak 1: top solid curve = 100% $CoFe_2O_4$ and peak 2: top dotted curve = 100% LSCF). Inset) Ratio peak1/peak2 vs. percentage of reference spectra (0= pure $CoFe_2O_4$, 1= pure LSCF).

In Figure 36 (bottom), the two reference spectra and their weighted sums in 10% steps are plotted. Two peaks were chosen to represent the different oxidation states. Peak 1 at 777.2 is mainly attributed to the 2+ oxidation state (so is the peak at 775.8 eV but due to its small value in the LSCF reference spectra using it for comparison might lead to higher errors in the concentration determination). Peak 2 shows a slight shift with increasing LSCF percentages, which is probably due to the fact that it is a combination of two peaks from the 3+ and 4+ oxidation state (see Appendix C.2) which are both present in LSCF

but not in CFO (only some 3+). This limits this type of analysis to the extraction of the 2+ vs. 3+/4+ composition (having more 3+ than 4+) using the peak1/peak2 ratio but will be fast and suffice for the purpose of this thesis. When plotting the peak ratio for the weighted sum spectra, linear behavior of the ratio with respect to the composition of the sample is evident (Figure 36, bottom inset). Now, the spectra obtained by the mapping procedure can be analyzed with respect to this peak ratio and the plot shown in the inset can be used to determine the percentage of LSCF and CFO, respectively.

In order for the mapping procedure to yield a spatially resolved picture of the Co oxidation states using the referencing method described above, obtaining the Co L_3 edge with sufficient resolution is essential. The difficulty lies in the tradeoff between incident photon flux and resolution, apparent in Figure 7. The 1200 lines/mm grating has a much lower flux but the resolution necessary to resolve the spectral features needed for the oxidation state analysis and loss in flux was partly compensated by choosing an exit slit width of 40 μm. To get a reasonable signal to noise ratio, the films on the samples had to be contacted with silver paint (since the YSZ substrate is an electrical insulator) and a rim was painted on the outer edges in order to obtain homogeneous contact over the sample surface. This reduced the sample surface usable for mapping slightly but still left an area of approximately 9 mm by 9 mm. The scan speed, step size and energy region had to be adjusted to yield the desired spectra in a reasonable timeframe. For the Co L_3 edge, 10 eV (774-784) were sufficient to obtain the full edge with some background to do the background subtraction and data was acquired every 0.05 eV (close to the energy resolution of the beamline at these energies) and the scan-speed was set to 0.1 eV per second. The mapping was done to accommodate the difference in beam dimension in the z direction (vertical, out of the synchrotron plane, perpendicular to the X-ray beam) and in y direction (horizontal, in synchrotron plane, perpendicular to the X-ray beam). Since the beam is much more focused in the out of plane direction the beam size here is much smaller (<0.5mm) whereas the in plane direction gives a wider beam of ~ 1 mm. The grid on the sample was made to get as many spectra as possible on the sample surface without overlap and within reasonable time limits. To accommodate the shape of the beam, a grid on the sample surface was chosen with 1 mm steps in the y and 0.5 mm steps in z direction. A total of 10 steps in the y and 21 steps in the z direction ensured that the whole surface was mapped. To obtain absolute z and y values (borders of the sample) in the chamber, the photon energy was set to the Co edge and incremental z and y scans were performed. After determining the absolute position of the sample, a scanfile was written, repeating the fastscan with the above described parameters on every point of the grid. The total scan time of one sample with this grid and scan parameters added up to just over 6 hours. The data-file containing all 210 spectra with 201 data points each were approximately 12.5 Mb plain text documents and for data analysis a special macro had to be written (using IGOR Pro as analysis software) an can be found in Appendix C.3.
First the macro loads the complete data-file and separates the individual scans. Then, the first scan is displayed and a region has to be defined for the linear background subtraction and will be preset for the subsequent spectra (can still be changed). Afterwards, the spectrum is peak normalized to the second peak and the value of the first peak is displayed making the determination of the peak ratio very fast and easy. It can now be entered in a matrix representing the scan grid and displayed. To obtain smoother images an interpolation is done using the interpolate picture package in Igor Pro. Here, each "pixel" value and the neighboring ones are used to determine the value in between and those are displayed as well. This increases the amount of pixels by a factor of four and makes the picture look much smoother. In Figure 37 the Co maps of three samples are

shown: “as deposited” in the top left (no treatment, after PLD deposition of the LSCF and GDC layers), a heat treated only sample in the top right (#2, no applied bias potential, side that was on the negative side of sample holder) and both sides of a sample with applied bias potential at the bottom (#7, 500 mV). The color legend is on the top and shows the different Co valency states with predominately Co^{4+} and Co^{3+} areas in dark red and predominately Co^{2+} areas in yellow. Since the value displayed here is the peak ratio, full scale is 1.2 for yellow (mostly CFO like) and 0.4 for dark red (zero values are black). For the “as deposited” sample (Figure 37 top left), an evenly dark red color across the whole sample surface indicates that most of the cobalt ions are in an oxidation state close to normal LSCF, which is mostly Co^{3+}. This is good confirmation that the pulsed laser deposition at high temperature in oxygen environment produces an even LSCF film of the desired stoichiometry. This film clearly changes upon heat treatment as evident from the heat treatment only sample mapping (top right). The mapping shows a dark red ring with the rest being lighter red in color, indicating a lower oxidation state of the cobalt. For the sample with applied bias potential (bottom) a similar dark ring for the negative side can be seen but with the rest of the sample having even more yellowish color, implicating even higher Co^{2+} content. On the positive side, we see a dark red Y shape and mostly brighter red everywhere else, indicating less transformation of Co^{3+} into Co^{2+} compared to the negative side. The significance of these shapes and explanation of their origin will be explained later in the conclusions part of this chapter (5.5). For now, a closer inspection of the Co L_3 edge variations across the sample is done and composed in Figure 38.

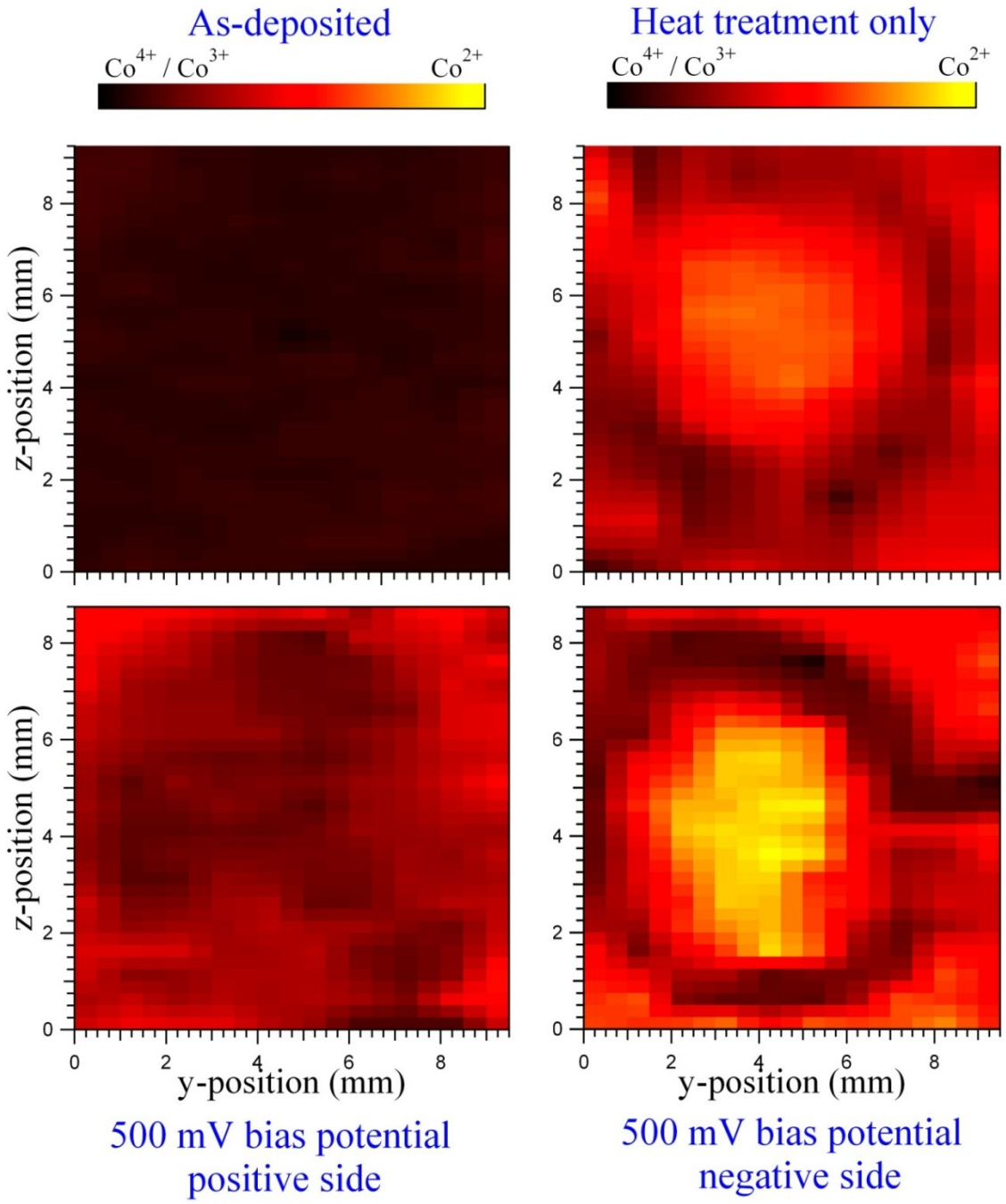

Figure 37: Co valence map of three different samples. Top left: "as deposited" sample without any treatment. Top right: Sample #2, only heat treatment, no applied bias potential (side that was on the normally negative side of the sample holder) Bottom: Sample #7, 500 mV applied bias during heat treatment, positive side on the left and negative side on the right.

The spectra with the minimum and maximum peak 1 to peak 2 ratios are plotted, as well as a spectrum with the average value across the sample (black solid, dashed and dotted lines in Figure 38). The spectra were then fitted using the LSCF and CFO reference spectra. The fitted spectra are in very good agreement with the data and show the validity

of the extracted peak values in the mapping. Again, the "as-deposited" sample (top left) shows almost no variation and is very close to the expected LSCF spectrum. The heat treatment only sample (top right) and the positive side of the 500 mV biased sample (bottom left) have very similar average spectra (peak ratios), with the biased sample featuring slightly lower Co oxidation sates. Finally, the negative side of the biased sample shows very high variations across the sample (minimum vs. maximum) and features the highest Co^{2+} valence concentration.

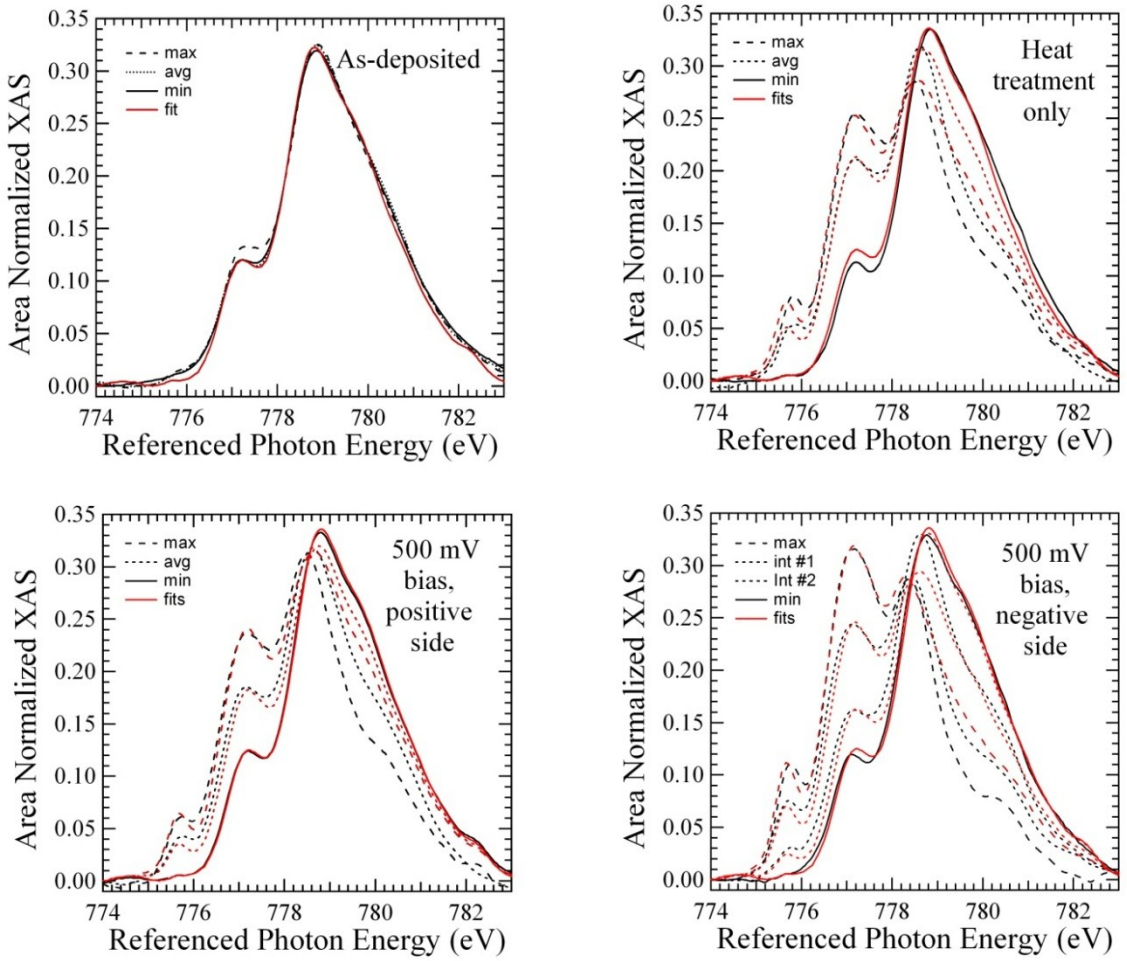

Figure 38: Representative Co L_3 fast-scans from the mappings shown in Figure 37. The minimum and maximum peak ratio spectra are shown, as well as an average spectrum (black) and fits by using the LSCF and CFO reference spectra (red). Top left: "as deposited" sample without any treatment. Top right: Sample #2, only heat treatment no applied bias potential Bottom: Sample #7, 500 mV applied bias during heat treatment, positive side on the left and negative side on the right.

Since the spectra acquired in the mapping are not only adequate for determining the peak ratio but also for fitting them with the two reference spectra, the percentage of the two Co oxidation states can be determined. Thus, the transformation of the peak ratio axis (color legend in 28) into a percentage axis, using the inset in Figure 36 (bottom), is possible. The highest value (yellow) would then be almost 100% Co^{2+} and the lowest value (dark red) will be approximately 60% Co^{3+} and 40% Co^{4+} according to Tai et al. [34]. This again

shows the validity of the color scale in Figure 37 using Co^{3+}/Co^{4+} for dark red and Co^{2+} for yellow.

5.4.3. Iron Edge Mapping

Last but not least, the Fe edge was mapped to check for possible variation in the Fe across the sample. Since the Fe L_3 edge does not exhibit intensity changes in peaks only associated with one oxidation state but rather changes in the intensity of the same peaks (Figure 32 top), extracting values for the possible oxidation state concentrations is difficult. However, peak intensity variations can be mapped and at least qualitatively compared to the results obtained for the Co edge mapping. In Figure 39 (top right), representative Fe L_3 XAS spectra are shown for the positive side of sample #7 (500 mV applied bias during heat treatment) and the evaluation of the mapping data with respect to various spectral features. The XAS spectra were peak height normalized to the main Fe L_3 peak at 706.4 eV and subsequently the intensity of the shoulder peak and trough extracted (see Figure 39). According to the literature, variations in the shoulder peak and trough are indicative of concentration changes between the Fe^{3+} and Fe^{2+} oxidation states, with a higher shoulder peak featuring more Fe^{2+} ions[79]. However, care has to be taken as the peak ratio can also be affected by the site occupation of the iron atoms (octahedral vs. tetrahedral) which was shown for different phases of Fe_2O_3 [80]. Since the LSCF film on the sample is polycrystalline after a short time at 800˚C in air, the site occupancy is not expected to change and direct comparison of the peak heights is validated. In Figure 39 (top left), the intensity of the shoulder peak is displayed. The color scale is the same as used in Figure 37 but now in arbitrary units of the peak normalized XAS intensity, with a minimum and maximum value of 40 and 51, respectively. At the bottom left, the map of the trough intensity is displayed, using the same color scale again, however with a maximum value (yellow) of 0.33 and a minimum value (dark red) of 0.23. Much more variation in intensity across the sample is visible in the map of the trough intensity. It looks very similar to the Co map of the same sample (Figure 37, bottom left) but with inverse colors, showing a bright red Y instead of a dark one. To determine the influence of the shoulder peak intensity variations, a map of the difference of peak intensity and trough intensity was computed and is displayed at the bottom right of Figure 39. The color scale maximum is 0.21 and the minimum is 0.13 and the map looks very close to the Co one. According to the literature, this suggests that more Fe is in its 2+ oxidation state where the color is yellow (bright red) since the shoulder peak is more pronounced there. On the other hand, it is more in a 3+ state where the color is dark red, as expected from stoichiometric LSCF. This is similar to the observation made for the Co mapping, having the more LSCF like state in a Y shape on this side of the sample and a lower oxidation state occurring in between. This evidence of a link between the Co and Fe oxidation state is useful for drawing conclusions. However, the difficulty in extracting the much smaller Fe peak and trough values, susceptible to larger errors due to improper background subtraction, and the lack of good references for the different oxidation states makes the Fe mapping much less reliable than the Co mapping at this point in time. Nonetheless, the quantitative observations from the Fe mapping can be used as additional evidence for determining possible causes for the patterns seen in the Co mapping.

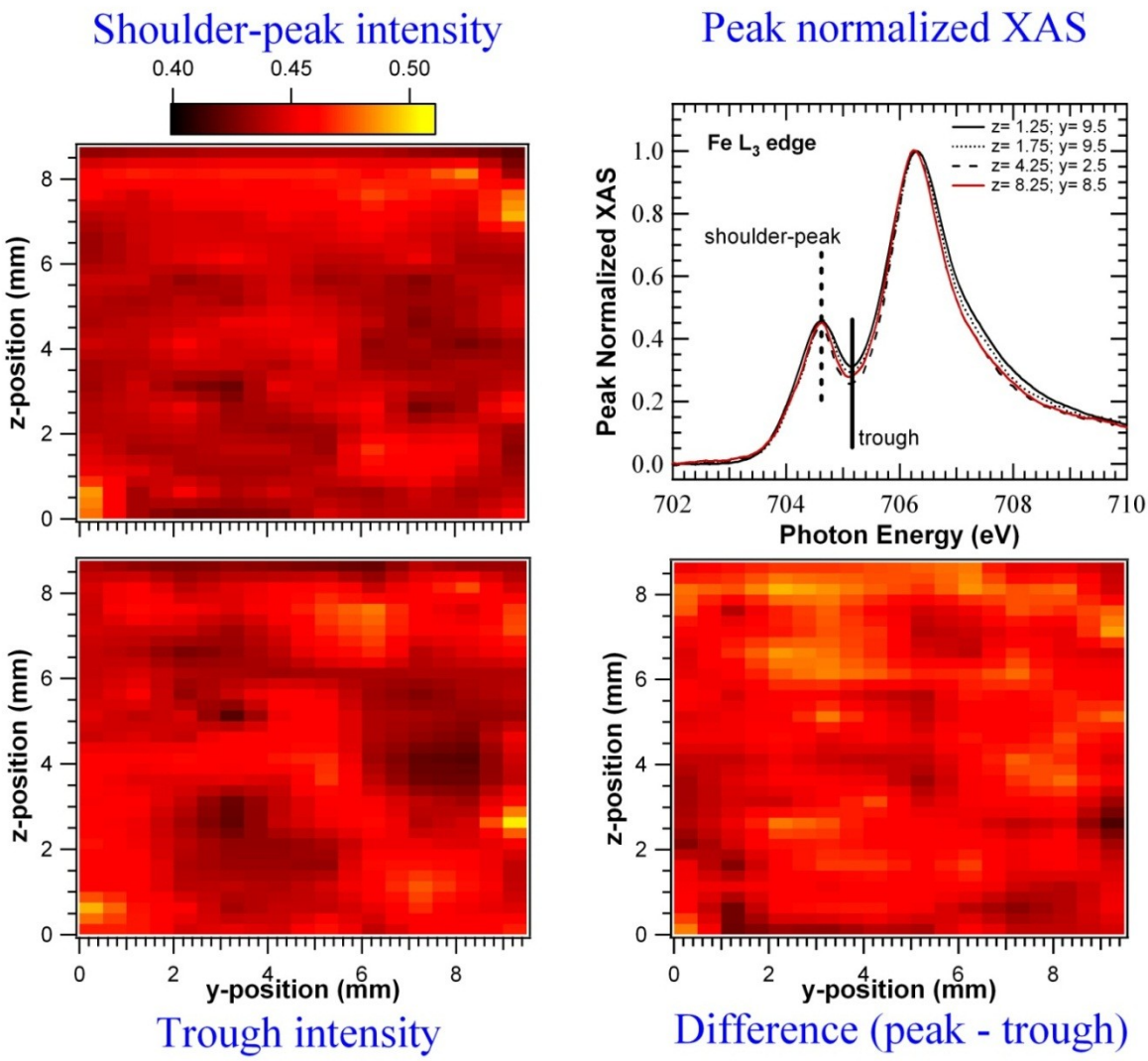

Figure 39: (Top right) Representative Fe L_3 spectra of the positive side of sample #7 (500 mV bias potential during heat treatment). The spectra are normalized to the main L_3 peak and the position of the shoulder peak and trough is marked that were used for the mapping. (Top left) Map of the shoulder-peak intensity. (Bottom left) Map of the trough intensity (same color scale but maximum value (yellow) is 0.33 and minimum value (dark red) is 0.23 (arbitrary units of peak normalized XAS). (Bottom right) Map of the difference "shoulder-peak intensity" minus "trough intensity" (same color scale; maximum value (yellow) is 0.21 and minimum value (dark red) is 0.13).

5.4. Conclusions

In conclusion, it was found that the high oxygen environment, high temperature PLD grown LSCF films (with GDC buffer layer) on single crystalline YSZ initially had the desired LSCF stoichiometry in the as-deposited samples. Upon heating the samples to a temperature of 800˚C in air, the very smooth film with a few small droplets on top transformed into a polycrystalline one (Figure 27 and 19). Large crystals were observed

on top of the film and identified to be Sr rich using EDX (Figure 29) and most likely consisting of SrO by comparing XPS data with data found in the literature for the same material. Crystal size analysis revealed an increase in crystal area and number when a bias potential was applied during heat treatment. This increase in Sr rich crystals, caused by applied bias potentials and oxygen ion flow, was previously observed by other groups and for other sample geometries [32, 33, 62, 63] and was used to explain performance degradation either due to occupation of surface incorporation sites (e.g. $SrCrO_4$ formation[15]) or lack of Sr in the near surface region[32, 33]. Indeed, the samples showed large degradation over time in the potentiostatic current measurements (Figure 25) and from the characteristic behavior it was concluded that for our samples the oxygen ion current is limited by the incorporation of adsorbed oxygen into the LSCF cathode material.

A new fast XAS scan method, implemented at beamline 6.3.1 at ALS, made it possible to "map" a sample with dimensions in the cm range, by acquiring the XAS spectra of hundreds of points across the sample surface. Since Sr does not change valency, direct Sr mapping using XAS is difficult, especially due to the lack of resolution needed to resolve the small changes induced by the change in crystal structure from LSCF to SrO. Thus, La, Co and Fe edges were measured but only Fe and Co were found to have significant spectral changes to extract information about the oxidation states (La remains in its 3+ state). After comparison with reference spectra, it was possible to extract the Co oxidation states expected in LSCF and measure their shift towards Co^{2+}. A similar method was used for the Fe edge but due to a lack of good reference spectra only qualitative results were obtained. Three different samples were mapped: an "as-deposited" sample, one heated to 800˚C for 100 hours in air and one with an additional bias potential of 500 mV applied. The latter two samples showed significant changes in the Co oxidation state distribution across the sample, featuring high amounts of Co^{2+}, especially in the sample with an applied bias potential. The distribution of these altered states can now be understood when comparing the mapping to actual pictures of the sample after the heat treatment. In Figure 40, the Co mapping of the positive side of sample #7 (with GDC interlayer, 500 mV applied bias during heat treatment) is shown in the bottom left, the Fe mapping shown in the top right, and a sized picture is shown twice in the bottom right and top left (the mappings are copies of the one shown in Figure 37 and 30). As guides to the eye, white lines are drawn from prominent features in the picture to their counterparts in the Co mapping. Excellent matching of the mapping features with the features visible in the picture of the sample shows the power of this technique to spatially resolve the oxidation state of the transition metal ions in the sample. Using the dimensions from the XAS mapping and the known size of the sample, a perfect match of sample area measured and picture of the sample was achieved. The better distinction of the Co features has its origin in the larger spectral feature difference for the two Co oxidation states in comparison to the rather small changes in the Fe spectrum.

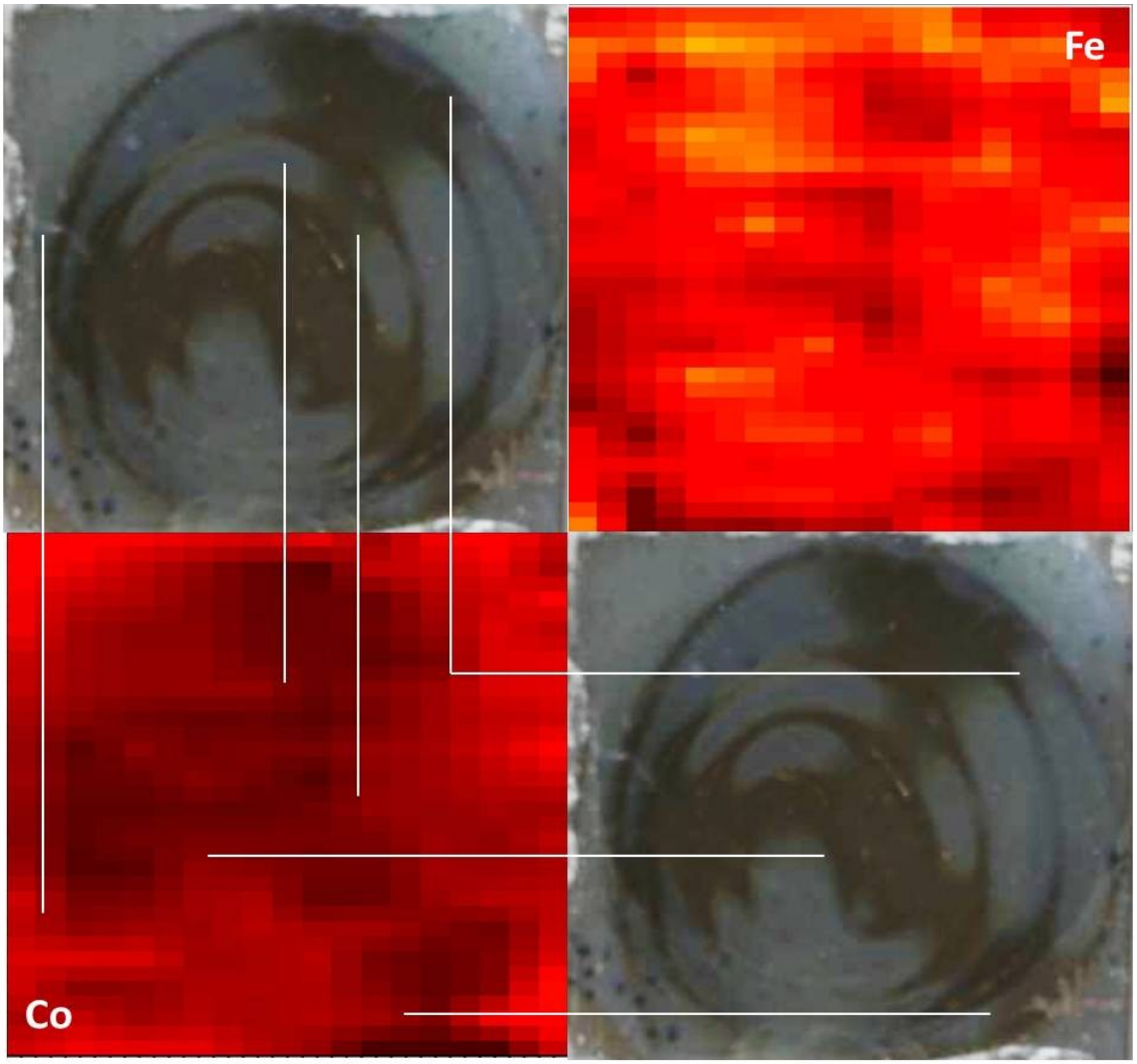

Figure 40: Comparison of the Co (bottom left) and Fe (top right) mapping with an actual picture (top left, bottom right) of the sample surface of the positive side of sample #7 (with GDC interlayer, 500 mV applied bias during heat treatment; mappings are copies of Figure 37 and 30). White lines as guide to the eye point out prominent structures in the picture and their counterpart in the map.

In order to find the origin of these structures, the sample position in the ceramic holder has to be considered. As mentioned in the "Experimental Setup" (Chapter 5.2), a gold spiral was used to provide the electrical contact with the sample (see Figure 22). This explains the spiral pattern on the surface seen in the picture in Figure 40 but not the difference in reflectivity, making some areas on the sample appear "white" in the picture when the flash was used and the camera positioned vertically above the sample, or no flash was used and the camera positioned at a grazing angle. This is good evidence that the film was not structurally altered itself, rather that the color change originates in the change in reflectivity of the surface. This alteration of the surface is very likely due to the SrO crystals forming upon heat treatment, which can also be observed in Figure 27 (bottom). The gold contact area in the FE-SEM picture shows no signs of crystallites, making it smooth and thus less reflective. Also, the spiral pattern visible in Figure 40 suggests that this is the same for the whole spiral contact area. However, on top of the

spiral pattern a dark Y shape is visible that is also clearly visible in the Co and Fe map (in contrast to the spiral pattern, which seems to be absent but is probably below the resolution limit). The reason for the dark Y shape can be easily demonstrated when overlaying the sample with a picture of the sample holder (it cannot be taken directly, since the sample surface in contact with the side of interest has to face the camera to get the white contrast from the flash). In Figure 41, an overlay of the same picture used in Figure 39 with the positive side of the sample holder is shown. The origin of the white color can now be directly linked to the three air holes in the sample holder. Apparently, the gold spiral hinders the access of ambient air to parts of the sample, making them appear dark in the picture. Together with the previous evidence, this suggests that the SrO crystal formation is reduced in areas of the sample with low / less air exchange. This is further solidified by the observations made for the negative side of the samples, featuring one large air supply hole and showing only one dark ring structure in the mapping (Figure 37) which can be attributed to the outmost ring of the spiral.

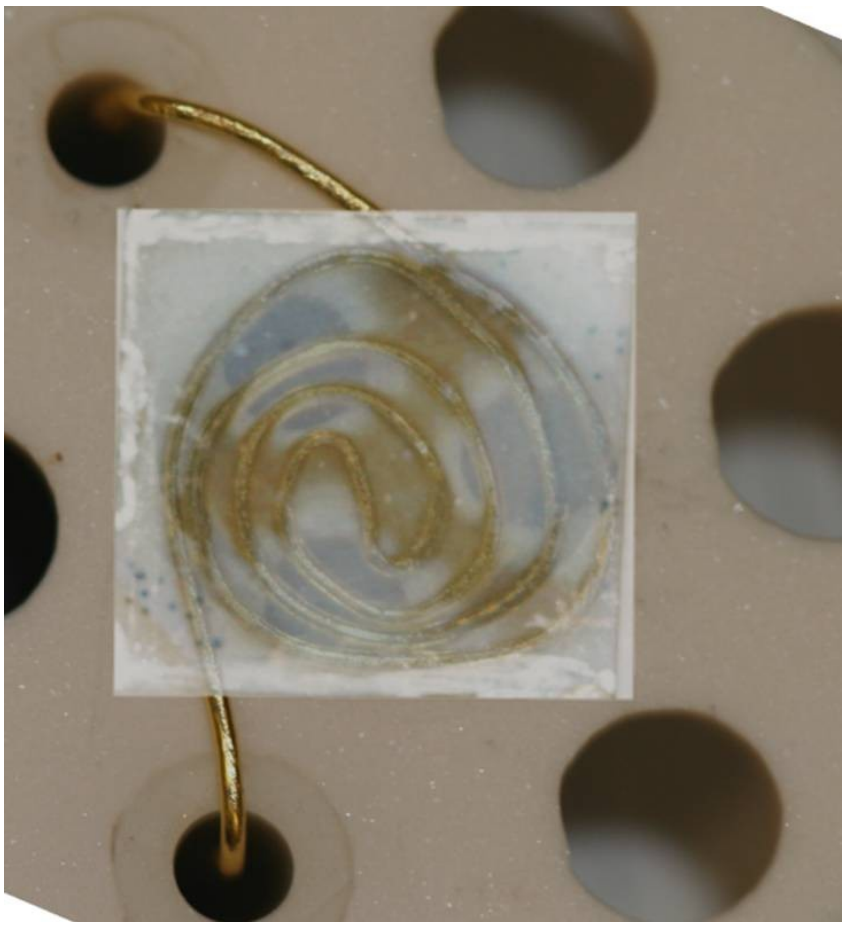

Figure 41: Overlay of a picture of sample #7 (positive side, same used in Figure 39) with the positive side of the sample holder. The picture of the sample has an enhanced contrast and brightness of 40% and 60% respectively and was made 20% translucent.

Since the XAS spectra only yielded peak ratios, a quantitative composition analysis of the film composition is impossible. This makes a complete assessment of the mechanisms leading to the differences in the oxidation state distribution across the sample and their dependence on the air accessibility difficult. However, a possible explanation for the observed patterns in the oxidation state mappings will be given here. As discussed earlier,

when heating LSCF in air the oxygen vacancy concentration increases which has to be compensated by valency changes of the transition metal ions to retain charge neutrality[34]. On the other hand, Sr segregation might also contribute to the vacancy neutralization, resulting in the observed SrO crystal formation at the surface. When applying a bias potential, this increase in oxygen vacancies is greatly enhanced on the cathode side of the sample, while it is reduced on the anode side of the sample. Since the Co can change its valency from 4+ to 3+ or even 2+ to compensate the positive oxygen vacancies, this explains why the negative side of the sample with and without bias potential (Figure 37 right column) shows the same structure but the sample with bias potential has a higher Co^{2+} concentration (more yellow). It is problematic however, that the sample without bias voltage shows a pattern at all. This can only be explained by the fact that the sample stoichiometry irreversibly changed after 100 hours at 800˚C. The only noticeable change however, was the Sr segregation and subsequent formation of SrO crystals at the surface. The increase of SrO crystals with applied bias potential, evident from the grain size analysis, is evidence for the correctness of this supposition. Since the Co and Fe valency changes occurring at high temperatures should be reversible, the formation of SrO can be seen as a mechanism for freezing in the low oxidation states of the transition metals.

If the Sr segregation would simply result in Sr vacancies and no change in the crystal structure or composition, one would expect the average transition metal valency to go up when cooling the sample down to compensate the lower oxygen vacancy concentration (more negative O ions in the lattice). However, the opposite case seems to be true and the average valency of Co and Fe goes down, with Co changing the most. Additionally, on the positive anode side the decrease in oxygen vacancies should reduce the amount of Co^{2+} and Fe^{2+} formed and thus also reduce Sr segregation. In Chapter 4 however, evidence was presented that this reduction of oxygen vacancies on the anode side might still lead to Sr segregation and SrO formation at the surface. That the total amount of Co^{2+} is reduced compared to the cathode side is evident when comparing Figure 38 bottom row mappings. The cathode side has much more Co^{2+} than the anode side, resulting in a much more yellow map. That the anode shows Co^{2+} even though the oxygen vacancy concentration is probably low means the Sr segregation is directly linked to the appearance of low valency transition metal ions.

As mentioned before, the most likely explanation for this link is that the LSCF film undergoes structural changes, featuring a secondary phase with higher concentrations of Co^{2+} and Fe^{2+}. It is possible that it forms e.g. the spinel structure $CoFe_2O_4$ that was used as reference due to the very good fit of its spectral features. It is also reasonable to assume that it contains some La^{3+} in the B site, making the total composition of the secondary phase similar to that of the host lattice LSCF. On the other hand, the Sr rich crystal growth observed could mean that the SrO is not “pure” but contains 2+ Co and Fe ions. This would also explain the match of the “white” areas seen in the pictures of the sample and the distribution of Co^{2+} and Fe^{2+} in the mappings. Which mechanism is more likely, might also depend on the polarization of the sample. Whereas on the cathode side higher oxygen deficiency leads to Sr segregation, making the secondary phase formation of a lower O containing spinel more likely, the overabundance of oxygen on the anode side would make the doped SrO crystals scenario more likely. To investigate which of the two actually occurs on what side (or possibly both) a structural analysis of the film after different heat treatment times would be needed in order to track possible phase changes and emerging secondary phases. The obvious choice would be X-ray diffraction (XRD) which can provide phase information and unit cell dimensions, also giving clues to possible lattice distortions. However, since the film is on the order of 10 nm which means it consists only of approximately 5-10 atomic layers, getting good quality XRD spectra is

challenging. Currently, this type of experiment was not available at MSU. Additionally, the crystals on the surface might not give a spectral contribution at all but rather leads to high noise levels. In conclusion, good quality, grazing angle XRD would greatly improve the understanding of the morphological changes in the films investigated and the proposed mechanisms.

Lastly, the obvious dependence on the air accessibility adds another layer of complication. Since the film is flat, no partial pressure differences across the surface are expected. The gold spiral used to contact the sample created “pockets” on the surface (in addition to the actual points of contact), where the gas layer above the sample might not have been in equilibrium with the surrounding air. This effect might have been increased by the fact that there was no air flow over the sample, thus only diffusion and no turbulent mixing to reach equilibrium. On the cathode side this results in a lower oxygen partial pressure above the sample surface and even higher oxygen vacancy concentrations in the cathode side. On the anode side, it would result in higher oxygen concentrations and even less oxygen vacancies in pockets with reduced air accessibility. Since these areas are therefore hindered in their capability of exchanging oxygen with the surrounding air, the overpotentials would increase. This increase in overpotential would lead to a reduced oxygen reduction / oxidation in those areas, comparable to a higher resistance. Thus, most of the oxygen ion flow would be conducted through the other areas of the sample, leading to less Sr segregation and lacking the “white” reflections seen in the picture for the well ventilated areas. Fister et al.[63] already showed an oxygen partial pressure dependence of Sr segregation and thus provide more evidence supporting this scenario.

Chapter 6

6. Summary and Outlook

In summary, the investigation of degradation phenomena on the cathode side of solid oxide fuel cells (SOFCs) is complex and many factors and interactions have to be considered in order to extract the underlying mechanisms. To accurately determine the impact of a single factor, such as bias potential, stoichiometry or gas flow on the degradation of this complex system, each individual mechanism in each material has to be studied separately. Subsequently, the impact of each factor on the system as a whole has to be determined. In modern solid oxide fuel cells, $La_{0.6}Sr_{0.4}Co_{0.2}Fe_{0.8}O_{3-\delta}$ (LSCF) is one of the most promising cathode material candidates. In cell tests featuring SOFCs with LSCF cathodes, the origin of degradation was found to be outside sources, e.g. Cr from inerconnects[14-16, 42], but also structural degradation[32, 33, 62, 63]. In this thesis, an in-depth investigation of the cathode material LSCF with respect to both ways of degradation was performed and the impact on cell performance determined.

First, the impact of gaseous Cr (CrO_3 and $CrO_2(OH)_2$) and its deposition as dense Cr_2O_3 surface layer on the YSZ electrolyte and LSCF cathode material was investigated. Using ^{18}O as a tracer for secondary ion mass spectroscopy (SIMS) analysis of diffusion profiles, the surface exchange coefficient as a function of Cr_2O_3 surface layer thickness was extracted. Fundamental differences in the oxygen uptake of YSZ ($Y_{0.15}Zr_{0.85}O_2$) and LSCF were identified by comparing the different impacts the Cr_2O_3 surface layer had on those two materials. On one hand, the mixed ionic/electronic conducting (MIEC) material LSCF has a very high surface exchange coefficient to begin with, mostly due to its electronic conductivity, supplying electrons for oxygen reduction. On the other hand, YSZ is mostly seen as an electrical insulator, leading to low surface exchange, but with a very high ionic conductivity. In this thesis it was shown that the cathode material LSCF was tremendously affected by the Cr_2O_3 surface layer and the surface exchange and reduction of oxygen is greatly hindered. In contrast, the YSZ actually showed improved performance, possibly due to the higher electrical conductivity of the Cr_2O_3, therefore acting as a catalyst on the surface. A critical thickness of ~ 12nm Cr_2O_3 was identified for LSCF, above which the positive effect of the mixed conductivity was nullified by the Cr_2O_3 surface layer. This finding is crucial for judging the impact of Cr on the performance of industrial SOFCs and gives valuable guidelines for the Cr tolerance of this material. This work also showed the complexity of SOFC studies, which usually involve two or more ceramic materials, often in intimate contact and how differently they can be affected by a single element introduced into the system. Thus, to correctly predict the interaction of an element with many different cell components can be quite challenging and increases the complexity of the degradation studies greatly.

Second, the structural degradation of the cathode material LSCF was investigated and the experience gained from the previous study was used to explore a new way to measure this degradation. Sr segregation and subsequent formation of SrO on the cathode was identified by previous authors (Ref [62]) but the dependence on electrical polarization and over-potential could not be measured. Using gaseous Cr as a tracer to identify the segregated Sr from Sr in bulk LSCF yielded highly valuable, quantitative data that was used to display the dependence of Sr segregation on applied bias potentials. From this data, two different mechanisms were proposed to explain the Sr segregation observed

previously by other groups on the cathode but also on the anode side of a symmetric SOFC sample. The Sr segregation dependence on the bias potential showed two completely different mechanisms for the two polarizations that were only discernable when looking at their dependence on bias potential. X-ray absorption spectroscopy (XAS) was used as a strong tool to investigate the oxidation states of the tracer element and to obtain the quantitative data needed to identify the bias potential dependency. Besides developing this new tool for investigating degradation, the experimental data again provides guidelines for the structural tolerance of oxygen vacancies in LSCF and the dependence on polarization, which can be crucial in applications like solid oxide electrolyzer cells (SOEC) or symmetric SOFCs.

Third, a new fast-XAS method was used in order to obtain the oxidation states of the transition metals in LSCF with good spatial resolution across samples with centimeter dimensions. High temperature, oxygen environment pulsed laser deposition (PLD) was used to deposit thin films of LSCF acting as cathode and anode on single-crystalline YSZ. Comparing the sample treatments and I-V characteristics with film morphology, segregation of Sr-rich crystals on top of the flat, polycrystalline LSCF film was observed. Energy dispersive X-ray spectroscopy (EDX) of those crystals and X-ray photoelectron spectroscopy (XPS) of the sample confirmed the existence of a second Sr phase which most likely consists of SrO. The amount of segregated crystals and the area covered by them was found to increase upon application of a bias potential during heat treatment at 800°C for 100 hours. Finally, the oxidation state mapping of Co and Fe across the sample showed a reduction in the valence / oxidation state. The areas, where a high percentage of reduction occurred, were visible in the mappings and could be cross-referenced to areas with good air circulation in the sample holder. Photographic pictures taken of the sample showed those areas to be more reflective than others, most likely due to an increase in number of crystallites on the surface, increasing diffuse reflection. This additional information was used to refine the proposed mechanisms that are believed to govern the Sr segregation under different polarizations. Structural changes of the surface are plausible causes for the different oxidation states observed in the mappings and could be used to mitigate structural degradation in the future. Mitigation strategies were proposed based on these findings and can help to reduce degradation by material property tailoring, e.g. co-doping.

Future experiments, e.g. investigating the crystal structure of thin LSCF films via XRD or measuring the total amount of Sr segregated to the surface are the next logical steps based on this work. They would greatly compliment the research presented here, contribute to today's knowledge and further the understanding of this material class. It would also facilitate the investigation of this class of materials, by providing standardized tools that can be used for all of them. In many ways, SOFCs are superior to the existing electrical generators in terms of size, noise and maintenance. However, SOFCs have shortcomings of their own that need to be overcome before commercialization. From degradation due to poisoning with Cr originating from the stainless steel interconnect over secondary phase formation and decomposition to Sr segregation at the surface, the oxygen reduction reaction, crucial for SOFC operation, can be blocked or reduced in many ways. However, identifying degradation mechanisms and finding mitigation strategies will greatly enhance efficiency and lifetime and therefore the usefulness of SOFCs in everyday life applications. This contribution towards more efficient and flexible energy usage is an important step towards a greener and more sustainable utilization of the remaining fossil fuels and can greatly ease the transition towards fully renewable energy sources.

Acknowledgements

This work would not have been possible without the outstanding mentorship of Prof. Juergen A. Schaefer and Prof. Yves U. Idzerda. Thank you for your tremendous support during all stages of this project, your inspiration and, most of all, nurturing my love for physics.

I would also like to thank my co-workers Paul, Alex, Harsh, Adam and Vanessa for the great time we had, the inspiring physics conversations and for making me feel at home.

My special thanks and deep gratitude go to my mother Angelika, father Horst, sister Stefanie, grandmas Margit and Ursula and especially to my fiancée Henriette for their moral (and financial) support. Thank you for preparing me for this adventure, your encouragement and for always believing in me. You made me the person that I am and I am proud to have such a great family.

The Secondary Ion Mass Spectroscopy was performed using the Environmental Molecular Sciences Laboratory (EMSL), a national scientific user facility sponsored by the Department of Energy's Office of Biological and Environmental Research and located at Pacific Northwest National Laboratory.

The X-ray absorption spectroscopy was in part done at the National Synchrotron Light Source (Brookhaven National Labs) beamline U4B and at the Advanced Light Source (Lawrence Berkeley national Labs) beamlines 4.0.2. and 6.3.1 which are all supported by the Department of Energy.

I want to especially acknowledge the help of Elke Arenholz at ALS in general and with the new fast scan and mapping measurements performed at beamline 6.3.1. Without her help and outstanding user support at ALS this thesis would not have been possible.

For the work presented in Chapter 3, I would like to thank the co-authors Zihua Zuh for providing the SIMS depth profile measurements and Ezana Negusse for providing the XAS measurements. I also would like to thank all authors for the scientific and linguistic support during the creation of the article.

For the research presented in Chapter 4, I would like to thank the co-authors for the scientific and linguistic support during the creation of the article, especially Alexandre Lussier for designing the test setup and help during operation.

Finally, I gratefully acknowledge the financial support by the Department of Energy, The National Energy Technology Laboratory under Award Number DE-08NT0004115 and part of it by the National Science Foundation under grant number CBET-0709358.

References

1 http://www.fuelcelltoday.com/media/pdf/education-kit/The-Technology.pdf.
2 U. S. E. I. Administration, *International Energy Outlook 2010*, 2010).
3 A. L. Robinson, *X-Ray Data Booklet, Section 2.2 History of Synchrotron Radiation*, 2009).
4 D. Attwood, *Soft X-rays and Extreme Ultraviolet Radiation* (Cambridge University Press, 2000).
5 W. C. Röntgen, Ann. Physik Chemie **N.F. 64**, 1 (1898).
6 H. C. S. J. Stöhr ed., *Magnetism From Fundamentals to Nanoscale Dynamics* (Springer.
7 R. Shankar, *Principles of Quantum Mechanics* (Plenum Press, 1980).
8 P. Nachimuthu, Synchrotron Radiation Instrumentation: Eighth International Conference **CP705**, 4 (2004).
9 http://www.energy.siemens.com/co/en/power-generation/fuel-cells/.
10 C. L. Tsai, *CERAMIC PROCESSING AND ELECTROCHEMICAL ANALYSIS OF PROTON CONDUCTIVE SOLID OXIDE FUEL CELL*, 2010).
11 K. Q. Huang, P. Y. Hou, and J. B. Goodenough, Solid State Ionics **129**, 237 (2000).
12 N. H. Menzler, F. Tietz, M. Bram, I. C. Vinke, and L. G. J. de Haart, Advances in Solid Oxide Fuel Cells IV: Ceram. Eng. Sci. Proc. **29** (2008).
13 http://www.thyssenkrupp.com/en/presse/art_detail.html&eid=tk_pnid930.
14 K. Hilpert, D. Das, M. Miller, D. H. Peck, and R. Weiß, Journal of The Electrochemical Society **143** (1996).
15 S. Taniguchi, M. Kadowaki, H. Kawamura, T. Yasuo, Y. Akiyama, Y. Miyake, and T. Saitoh, Journal of Power Sources **55**, 73 (1995).
16 S. P. S. Badwal, R. Deller, K. Foger, Y. Ramprakash, and J. P. Zhang, Solid State Ionics **99**, 297 (1997).
17 S. P. Jiang and Y. Zhen, Solid State Ionics **179**, 5 (2008).
18 E. Konysheva, H. Penkalla, E. Wessel, J. Mertens, U. Seeling, L. Singheiser, and K. Hilpert, Journal of the Electrochemical Society **153**, A765 (2006).
19 J. W. Fergus, International Journal of Hydrogen Energy **32**, 3664 (2007).
20 M. Finsterbusch, A. Lussier, E. Negusse, Z. H. Zhu, R. J. Smith, J. A. Schaefer, and Y. U. Idzerda, Solid State Ionics **181**, 640 (2010).
21 H. Chen, et al., Surface & Coatings Technology **202**, 4820 (2008).
22 S. B. Adler, Chemical Reviews **104**, 4791 (2004).
23 A. Lussier, S. Sofie, J. Dvorak, and Y. U. Idzerda, International Journal of Hydrogen Energy **33**, 3945 (2008).
24 Y. D. Zhen and S. P. Jiang, Journal of the Electrochemical Society **153**, A2245 (2006).
25 S. B. Adler, J. A. Lane, and B. C. H. Steele, Journal of the Electrochemical Society **143**, 3554 (1996).
26 K. Swierczek and M. Gozu, Journal of Power Sources **173**, 695 (2007).
27 A. Esquirol, N. P. Brandon, J. A. Kilner, and M. Mogensen, Journal of the Electrochemical Society **151**, A1847 (2004).
28 S. B. Adler, Solid State Ionics **111**, 125 (1998).

[29] J. M. Ralph, C. Rossignol, and R. Kumar, Journal of the Electrochemical Society **150**, A1518 (2003).
[30] A. Chen, G. Bourne, K. Siebein, R. DeHoff, E. D. Wachsman, and K. Jones, Journal of The American Ceramic Society **91**, 5 (2008).
[31] N. Jordan, W. Assenmacher, S. Uhlenbruck, V. A. C. Haanappel, H. P. Buchkremer, D. Stover, and W. Mader, Solid State Ionics **179**, 919 (2008).
[32] S. P. Simner, M. D. Anderson, M. H. Engelhard, and S. J.W., Electrochem. and Solid-State Letters **9**, A478 (2006).
[33] D. Oh, E. N. Armstrong, D. Jung, C. C. Kan, and E. D. Wachsman, ECS Transactions **25 (2)**, 2871 (2009).
[34] L. W. Tai, M. M. Nasrallah, H. U. Anderson, D. M. Sparlin, and S. R. Sehlin, Solid State Ionics **76**, 273 (1995).
[35] J. M. Wimmer and I. Bransky, edited by N. M. Tallan (Pergamon Press, New York, 1971).
[36] F. A. Kroger and H. J. Vink, Solid State Physics-Advances in Research and Applications **3**, 307 (1956).
[37] C. J. Zhang, et al., Nature Materials **9**, 944 (2010).
[38] S. P. Jiang, Materials Science and Engineering a-Structural Materials Properties Microstructure and Processing **418**, 199 (2006).
[39] L. C. De Jonghe, C. P. Jacobson, and S. J. Visco, Annual Review of Materials Research **33**, 169 (2003).
[40] J. W. Fergus, Materials Science and Engineering a-Structural Materials Properties Microstructure and Processing **397**, 271 (2005).
[41] A. Lussier, et al., Thin Solid Films **516**, 4 (2008).
[42] S. P. Jiang, S. Zhang, and Y. D. Zhen, Journal of The Electrochemical Society **153**, 7 (2006).
[43] J. A. Lane and J. A. Kilner, Solid State Ionics **136**, 927 (2000).
[44] R. A. De Souza and R. J. Chater, Solid State Ionics **176**, 1915 (2005).
[45] P. S. Manning, J. D. Sirman, and J. A. Kilner, Solid State Ionics **93**, 125 (1996).
[46] J. Crank, *The Mathematics of Diffusion* (Oxford University Press, 1975).
[47] M. Leonhardt, R. A. De Souza, J. Claus, and J. Maier, Journal of the Electrochemical Society **149**, J19 (2002).
[48] R. A. De Souza, Physical Chemistry Chemical Physics **8**, 890 (2006).
[49] S. B. Adler, X. Y. Chen, and J. R. Wilson, Journal of Catalysis **245**, 91 (2007).
[50] A. Atkinson, M. R. Levy, S. Roche, and R. A. Rudkin, Solid State Ionics **177**, 1767 (2006).
[51] J. A. Crawford and R. W. Vest, Journal of Applied Physics **35**, 5 (1964).
[52] V. R. Paiverneker, A. N. Petelin, F. J. Crowne, and D. C. Nagle, Physical Review B **40**, 8555 (1989).
[53] I. Kosacki, T. Suzuki, V. Petrovsky, and H. U. Anderson, Solid State Ionics **136**, 1225 (2000).
[54] T. Komatsu, R. Chiba, H. Arai, and K. Sato, Journal of Power Sources **176**, 132 (2008).
[55] F. Tietz, V. A. C. Haanappel, A. Mai, J. Mertens, and D. Stover, Journal of Power Sources **156**, 20 (2006).
[56] Y. Matsuzaki and I. Yasuda, Journal of the Electrochemical Society **148**, A126 (2001).
[57] M. Finsterbusch, A. Lussier, J. A. Schaefer, and Y. U. Idzerda, Solid State Ionics **submitted (under review)** (2011).

[58] V. I. Sharma and B. Yildiz, Journal of the Electrochemical Society **157**, B441 (2010).
[59] M. Burriel, C. Niedrig, W. Menesklou, S. F. Wagner, J. Santiso, and E. Ivers-Tiffee, Solid State Ionics **181**, 602 (2010).
[60] Z. P. Shao, S. M. Haile, J. Ahn, P. D. Ronney, Z. L. Zhan, and S. A. Barnett, Nature **435**, 795 (2005).
[61] J. N. Eckstein, Nature Materials **6**, 473 (2007).
[62] F. S. Baumann, J. Fleig, M. Konuma, U. Starke, H. U. Habermeier, and J. Maier, Journal of the Electrochemical Society **152**, A2074 (2005).
[63] T. T. Fister, D. D. Fong, J. A. Eastman, P. M. Baldo, M. J. Highland, P. H. Fuoss, K. R. Balasubramaniam, J. C. Meador, and P. A. Salvador, Applied Physics Letters **93** (2008).
[64] L. Yang, S. Z. Wang, K. Blinn, M. F. Liu, Z. Liu, Z. Cheng, and M. L. Liu, Science **326**, 126 (2009).
[65] J. C. Ruiz-Morales, J. Canales-Vazquez, C. Savaniu, D. Marrero-Lopez, W. Z. Zhou, and J. T. S. Irvine, Nature **439**, 568 (2006).
[66] A. M. Svensson, S. Sunde, and K. Nisancioglu, Journal of the Electrochemical Society **145**, 1390 (1998).
[67] E. Riedel, *Anorganische Chemie* (de Gruyter, Berlin, New York, 2002).
[68] Y. Tsur and I. Riess, Solid State Ionics **119**, 37 (1999).
[69] E. Ruiz-Trejo, J. D. Sirman, Y. M. Baikov, and J. A. Kilner, Solid State Ionics **115**, 565 (1998).
[70] P. S. Manning, J. D. Sirman, R. A. DeSouza, and J. A. Kilner, Solid State Ionics **100**, 1 (1997).
[71] A. Hagen, Y. L. Liu, R. Barfod, and P. V. Hendriksen, Journal of the Electrochemical Society **155**, B1047 (2008).
[72] K. Li, B. Wang, B. Zydorczak, and Z. T. Wu, Journal of Membrane Science **344**, 101 (2009).
[73] D. Mandrino, M. Godec, M. Torkar, and M. Jenko, Surface and Interface Analysis **40**, 285 (2008).
[74] L. Reimer, *Scanning Electron Microscopy* (Springer, 1998).
[75] B. Lewis and J. C. Anderson, *Nucleation and Growth of Thin Films* (Academic Press, 1978).
[76] B. H. Frazer, B. Gilbert, B. R. Sonderegger, and G. De Stasio, Surface Science **537**, 161 (2003).
[77] A. Jablonski and C. J. Powell, Journal of Electron Spectroscopy and Related Phenomena **100**, 137 (1999).
[78] A. Jablonski and C. J. Powell, Surface Science **551**, 106 (2004).
[79] K. Kuepper, M. Raekers, C. Taubitz, H. Hesse, M. Neumann, A. T. Young, C. Piamonteze, F. Bondino, and K. C. Prince, Journal of Applied Physics **104** (2008).
[80] J. S. Kang, et al., Journal of Physics-Condensed Matter **20** (2008).
[81] S. Hidai, et al., Physical Chemistry Chemical Physics **11**, 8226 (2009).
[82] H. Jung, S. J. Lee, M. Song, S. Lee, H. J. Lee, D. H. Kim, J. S. Kang, C. L. Zhang, and S. W. Cheong, New Journal of Physics **11** (2009).

Appendix A

Abbreviations

ALS	–	advanced light source
ARPES	–	angle resolved photoelectron spectroscopy
CTE	–	coefficient of thermal expansion
CFO	–	$CoFe_2O_4$
CGO	–	cerium gadolinium oxide (see GDC)
DMFC	–	direct methanol fuel cell
EDS, EDX	–	energy dispersive X-ray spectroscopy
EPU	–	elliptical polarizing undulator
FE-SEM	–	field emission secondary electron microscopy
GDC	–	Gd doped ceria, $Gd_xCe_{1-x}O_2$ (used in this thesis: $Gd_{0.1}Ce_{0.9}O_2$)
LSCF,LSCFO	–	$La_{1-y}Sr_yCo_xFe_{1-x}O_{3-\delta}$ used in this thesis: $La_{0.6}Sr_{0.4}Co_{0.2}Fe_{0.8}O_{3-\delta}$
LSM, LSMO	–	$La_{1-x}Sr_xMnO_3$
NSLS	–	national synchrotron light source
PEMFC	–	polymer electrolyte membrane fuel cell, proton exchange membrane fuel cell
PLD	–	pulsed laser deposition
RBS	–	Rutherford backscattering spectroscopy
RF	–	radio frequency
SIMS	–	secondary ion mass spectroscopy
SOFC	–	solid oxide fuel cell
SOEC	–	sold oxide electrolyzer cell
TEY	–	total electron yield
TFY	–	total fluorescence yield

YSZ	–	yttria stabilized zirconia, $Y_xZr_{1-x}O_2$ (used in this thesis: $Y_{0.15}Zr_{0.85}O_2$)
XAS	–	X-ray absorption spectroscopy
XMCD	–	X-ray magnetic circular dichroism
XPS	–	X-ray photoelectron spectroscopy
XRD	–	X-ray powder diffraction

Appendix B

Additional Material

C.1: Figure 7 from reference F.S. Baumann et al. „Strong Performance Improvement of $La_{0.6}Sr_{0.4}Co_{0.2}Fe_{0.8}O_{3-\delta}$ SOFC Cathodes by Electrochemical Activation“ [62] showing their XPS analysis of cathodic and anodic polarized LSCF, demonstrating the resulting changes in the Sr 3d spectrum from SrO segregation at the surface. The anodic polarization case (B) is comparable to the XPS spectrum shown in this work.

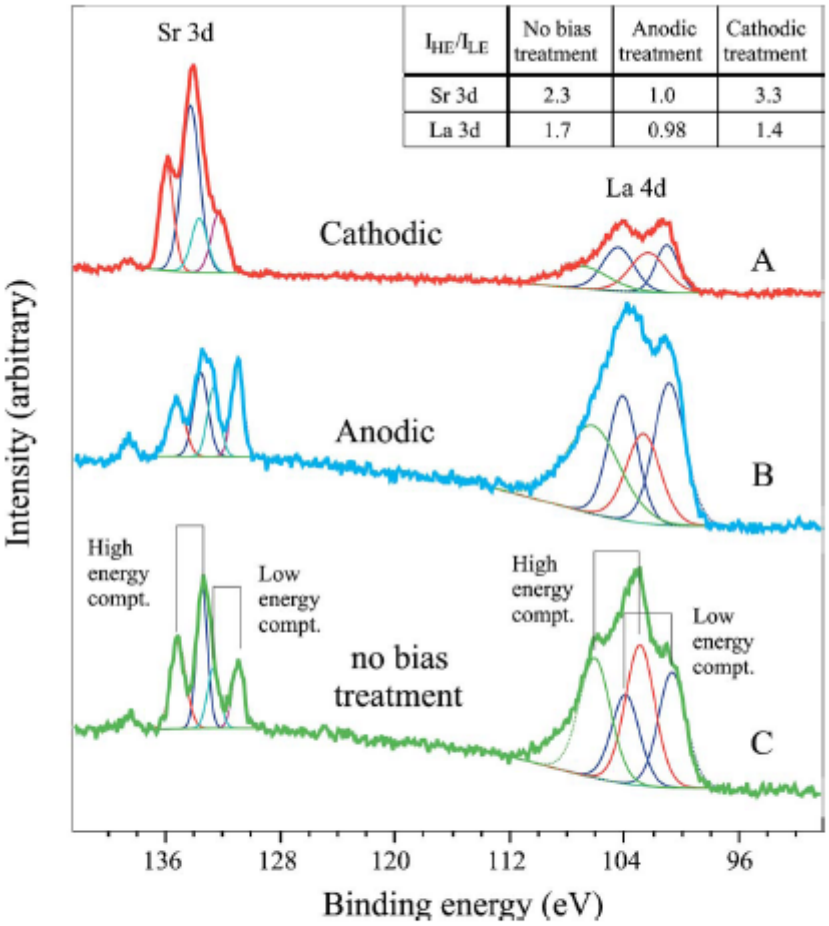

I_{HE}/I_{LE}	No bias treatment	Anodic treatment	Cathodic treatment
Sr 3d	2.3	1.0	3.3
La 3d	1.7	0.98	1.4

Figure 6. XPS spectra of the Sr 3d and La 4d core levels of three nominally identical $La_{0.6}Sr_{0.4}Co_{0.8}Fe_{0.2}O_{3-\delta}$ microelectrodes with different electrochemical pretreatment: (A) a cathodically, (B) an anodically, and (C) an unpolarized electrode. Two chemically different spin-orbit split doublets are fitted to the experimental data (see text for details).

C.2 Multipeak fit of the reference spectra in Figure 36. The residual is given in $1x10^{-3}$ at the top of the graph. 3 peaks were kept at constant energy in both spectra, representing possible 2+, 3+ and 4+ states. The difference in the ratio of peak 1 and 2 in Figure 36 vs. using the fitted peaks in this figure is neglectable (<1%).

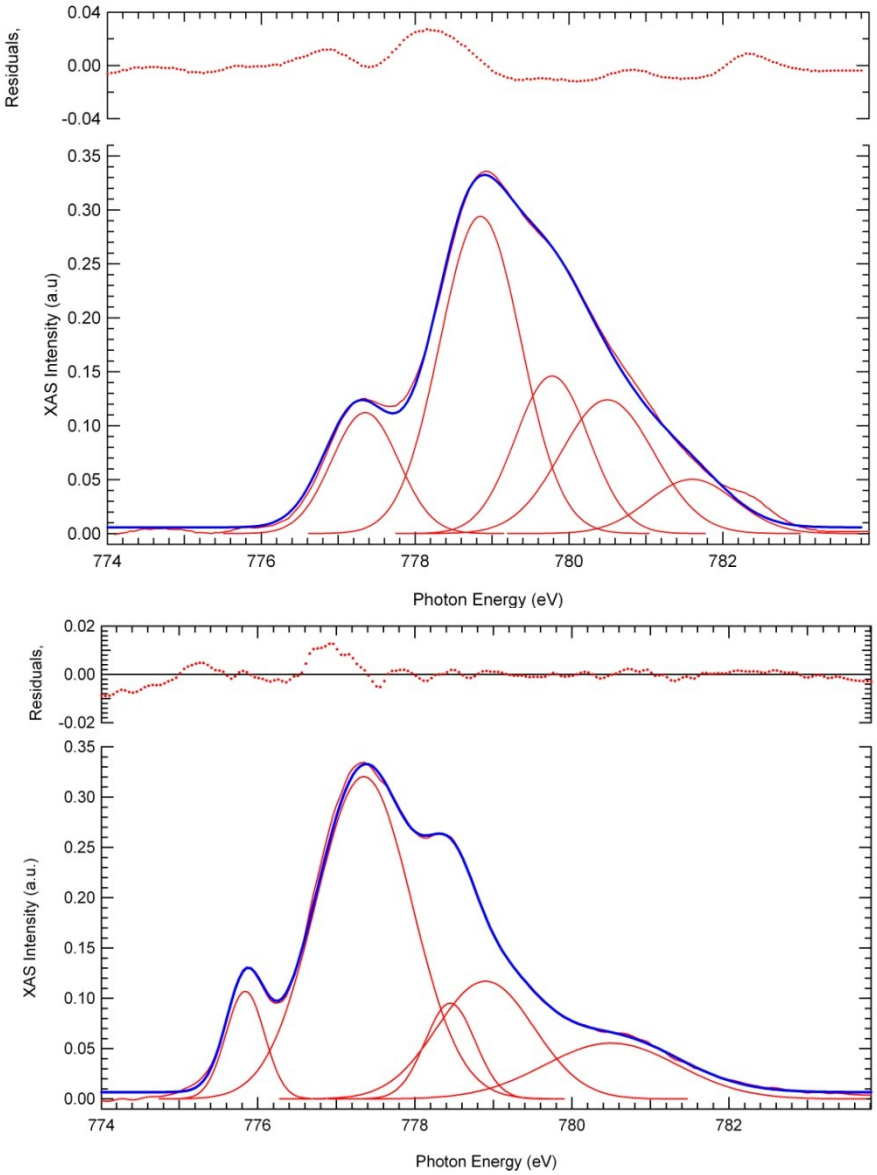
Residuals,
0.04
0.00
-0.04
XAS Intensity (a.u)
0.35
0.30
0.25
0.20
0.15
0.10
0.05
0.00
774
776
778
780
782
Photon Energy (eV)
Residuals,
0.02
0.00
-0.02
XAS Intensity (a.u.)
0.35
0.30
0.25
0.20
0.15
0.10
0.05
0.00
774
776
778
780
782
Photon Energy (eV)

Appendix C

List of publications

"Oxygen vacancy induced cation segregation in mixed ionic/ electronic conductors"
Finsterbusch, M.; Lussier, A.; Schaefer, J.A.; Idzerda, Y.U.; submitted to "Solid State Ionics" August 3rd 2011

"Epitaxial growth and thermoelectric properties of TiNiSn and $Zr_{0.5}Hf_{0.5}NiSn$ thin films"
Jaeger, T; Mix, C.; Schwall, M.; Kozina, X.; Barth, J.; Balke,B.; Finsterbusch, M.; Yves U. Idzerda, Y.U.; Felser, C.; Jakob, G.; *accepted* "Thin Solid Films", July 1st 2011

"Effect of Cr_2O_3 on the ^{18}O tracer incorporation in SOFC materials"
Finsterbusch, M.; Lussier, A.; Negusse, E.; Zhu, Z.; Smith, R.J.; Schaefer, J.A.; Idzerda, Y.U.; Solid State Ionics, v 181, n 13-14, p 640-645, May 21st 2010

"Thermal stability and oxidation resistance of TiCrAlYO coatings on SS430 for solid oxide fuel cell interconnect applications"
Chen, H.; Lucas, J.A.; Priyantha, W.; Kopczyk, M.; Smith, R.J.; Lund, K.; Key, C.; Finsterbusch, M.; Gannon, P.E.; Deibert, M.; Gorokhovsky, V.I.; Shutthanandan, V.; Nachimuthu, P. **;** *Surface & Coatings Technology*, v 202, n 19, p 4820-4, June 25th 2008

"Interface mixing of Al/Fe and Fe/Al bilayer systems and the role of Ti as a stabilizing interlayer using Rutherford backscattering spectrometry and X-ray reflectometry"
Priyantha, W.; Chen, H.; Kopczyk, M.; Smith, R.J.; Kayani, A.; Comouth, A.; Finsterbusch, M.; Nachimuthu, P.; McCready, D.; *Journal of Applied Physics*, v 103, n 1, p 014508-1-5, January 1st 2008

Erklärung

Ich versichere, dass ich die vorliegende Arbeit ohne unzulässige Hilfe Dritter und ohne Benutzung anderer als der angegebenen Hilfsmittel angefertigt habe. Die aus anderen Quellen direkt oder indirekt übernommenen Daten und Konzepte sind unter Angabe der Quelle gekennzeichnet. Weitere Personen waren an der inhaltlich-materiellen Erstellung der vorliegenden Arbeit nicht beteiligt. Insbesondere habe ich hierfür nicht die entgeltliche
Hilfe von Vermittlungs- bzw. Beratungsdiensten (Promotionsberater oder anderer Personen)
in Anspruch genommen. Niemand hat von mir unmittelbar oder mittelbar geldwerte Leistungen für Arbeiten erhalten, die im Zusammenhang mit dem Inhalte der vorgelegten Dissertation stehen. Die Arbeit wurde bisher weder im In- noch im Ausland in gleicher oder ähnlicher Form einer Prüfungsbehörde vorgelegt. Ich bin darauf hingewiesen worden,
dass die Unrichtigkeit der vorstehenden Erklärung als Täuschungsversuch angesehen wird
und den erfolglosen Abbruch des Promotionsverfahrens zu Folge hat.

Ilmenau, den 9. Oktober 2011

Martin Finsterbusch